



universität  
wien

# DIPLOMARBEIT

Titel der Diplomarbeit

Preparation of a  $^{55}\text{Fe}$ -AMS standard and the precise measurement  
of the neutron capture cross-section of  $^{54}\text{Fe}(n,\gamma)$

angestrebter akademischer Grad

Magister der Naturwissenschaften (Mag. rer. nat.)

Verfasser:	Kathrin Buczak
Matrikel-Nummer:	9171568
Studienrichtung:	411 Physik
Betreuer:	Ao. Univ.-Prof. DI Dr. Robin Golser

Wien, am 19.10.2009



## Abstract

The interest in neutron capture on  $^{54}\text{Fe}$  is linked to a variety of topics: to studies of nucleosynthesis in stellar environments, to radioactive waste generation in fusion reactors and to the half-life of the long-lived  $^{59}\text{Ni}$ . In this regard samples have been irradiated with neutrons of energies in the range from thermal to MeV at several facilities, offering different irradiation conditions. The radionuclide  $^{55}\text{Fe}$  ( $t_{1/2} = 2.7$  yr) produced in these activations, was measured at VERA (Vienna Environmental Research Accelerator) via accelerator mass spectrometry (AMS). Due to the absence of an isobaric interference, this technique allows highly sensitive detection of  $^{55}\text{Fe}$ . Such ultra-low isotope ratio measurements, however, require an accurate  $^{55}\text{Fe}$ -AMS standard as reference material to deduce absolute  $^{55}\text{Fe}/\text{Fe}$  ratios:

(1) At VERA, iron samples, highly enriched in  $^{54}\text{Fe}$ , were bombarded with 5.5 MeV protons to produce  $^{55}\text{Co}$  ( $t_{1/2}=17.53$  h), which decays to  $^{55}\text{Fe}$ . The total number of daughter-nuclides  $^{55}\text{Fe}$  was determined from the measured  $^{55}\text{Co}$ -activity.

(2) Another independent standard was produced by a dilution series of a certified  $^{55}\text{Fe}$ -standard-solution.

For the measurement of the thermal neutron capture cross section  $\sigma(^{54}\text{Fe}(n,\gamma)^{55}\text{Fe})$ , irradiations have been performed at the TRIGA Mark-II reactor of the Atominstitut in Vienna, and with cold neutrons at the Budapest Research Reactor. The thermal cross-section value was determined to  $(2.328 \pm 0.060)$  barn.

This result has consequences on the value of the half-life of long-lived radioisotope  $^{59}\text{Ni}$ , which was measured by Nishiizumi et al. to  $(76\,000 \pm 5\,000)$  y and by Rühm et al. to  $(108\,000 \pm 13\,000)$  y. The main contribution to the uncertainty of the latter value came from the cross-section value for  $^{54}\text{Fe}(n,\gamma)$ , which could be reduced to  $< 3\%$  in this work. With the new result for the neutron capture cross-section value on  $^{54}\text{Fe}$  and improved knowledge of additional contributions, the above mentioned  $^{59}\text{Ni}$ -half-life value of 108 000 y will change to  $(92\,700 \pm 5\,000)$  y. The total uncertainty is reduced to 5.4 %.



## Zusammenfassung

Das Interesse am Wirkungsquerschnitt für die Kernreaktion  $^{54}\text{Fe}(n,\gamma)$  ist verknüpft mit einer Vielfalt an Themen:

mit der Nukleosynthese in Sternen, mit der Erzeugung von radioaktivem Abfall in Fusionsreaktoren und mit der Halbwertszeit von  $^{59}\text{Ni}$ . Zu diesem Zwecke wurden Eisenproben an verschiedenen Anlagen mit Neutronen bestrahlt, deren Energie von thermischen Neutronen bis hin zu MeV-Neutronen reichten. Das Radionuklid  $^{55}\text{Fe}$  ( $t_{1/2} = 2.7$  yr), das im Zuge dieser Aktivierungen produziert wurde, wurde mit AMS (accelerator mass spectrometry) bei VERA (Vienna Environmental Research Accelerator) gemessen. Das einzige stabile Isobar  $^{55}\text{Mn}$  bildet keine negativen Ionen und damit sind sehr sensitive  $^{55}\text{Fe}$ -AMS Messungen möglich. Die Messung genauer Isotopenverhältnisse setzt einen gut bekannten  $^{55}\text{Fe}$ -AMS Standard als Referenzmaterial voraus, um absolute Isotopenverhältnisse  $^{55}\text{Fe}/\text{Fe}$  zu bestimmen:

(1) Bei VERA wurden Eisenproben, die stark in  $^{54}\text{Fe}$  angereichert waren, mit 5.5 MeV Protonen bombardiert, um  $^{55}\text{Co}$  ( $t_{1/2}=17.53$  h) zu produzieren, welches anschließend zu  $^{55}\text{Fe}$  zerfällt. Die totale Anzahl an Tochternukliden  $^{55}\text{Fe}$  wurde über die gemessene  $^{55}\text{Co}$ -Aktivität bestimmt.

(2) Ein weiterer, unabhängiger Standard wurde durch eine Verdünnungsreihe einer zertifizierten  $^{55}\text{Fe}$ -Standardlösung hergestellt.

Für die Messung des thermischen Neutronen-Einfangwirkungsquerschnittes  $\sigma(^{54}\text{Fe}(n,\gamma)^{55}\text{Fe})$ , wurden Proben am TRIGA Mark-II Reaktor des Wiener Atominstutits mit thermischen Neutronen und am Budapest Research Reactor mit kalten Neutronen bestrahlt. Der Wirkungsquerschnitt wurde zu  $(2.328 \pm 0.060)$  barn bestimmt.

Dieses Ergebnis wirkt sich direkt auf die Halbwertszeitbestimmung des langlebigen Radionuklids  $^{59}\text{Ni}$  aus, welche durch Nishiizumi et al. zu  $(76\,000 \pm 5\,000)$  Jahren und durch Rühm et al. zu  $(108\,000 \pm 13\,000)$  Jahren bestimmt wurde. Die Unsicherheit des letzteren Ergebnisses setzte sich hauptsächlich aus der Unsicherheit des Wirkungsquerschnittes für  $^{54}\text{Fe}(n,\gamma)$  zusammen, welcher in dieser Arbeit zu  $< 3\%$  reduziert werden konnte. Mit dem präzise bestimmten Wirkungsquerschnitt für  $^{54}\text{Fe}(n,\gamma)$  und neueren bekannten Daten ändert sich der Wert für die  $^{59}\text{Ni}$ -Halbwertszeit von 108 000 Jahren zu  $(92\,700 \pm 5\,000)$  Jahren. Die gesamte Unsicherheit reduziert sich auf  $\approx 5.4\%$ .

---

# Contents

<b>1</b>	<b>Introduction</b>	<b>1</b>
1.1	Motivation . . . . .	1
1.2	Outline . . . . .	2
<b>2</b>	<b>Theoretical background</b>	<b>5</b>
2.1	The basics - particles . . . . .	5
2.1.1	The (radioactive) atom . . . . .	6
2.1.2	Physics of photons . . . . .	7
2.1.3	Interactions of particles in matter . . . . .	13
2.2	Nuclear Reactions . . . . .	15
2.2.1	The cross section . . . . .	16
<b>3</b>	<b>Experimental background</b>	<b>21</b>
3.1	Iron and its isotopes . . . . .	21
3.2	Nuclear reactions on $^{54}\text{Fe}$ . . . . .	22
3.2.1	Neutron capture $^{54}\text{Fe}(n,\gamma)^{55}\text{Fe}$ . . . . .	23
3.2.2	Proton capture $^{54}\text{Fe}(p,\gamma)^{55}\text{Co}$ . . . . .	26
3.3	The facility VERA . . . . .	29
3.3.1	The principle of accelerator mass spectrometry (AMS) . . . . .	29
3.3.2	The main components . . . . .	31
3.3.3	Isotope ratios - Ion detection systems . . . . .	34
<b>4</b>	<b>Mathematical background</b>	<b>39</b>
4.1	Activation - Production of radionuclides . . . . .	39
4.2	Determination of produced $^{55}\text{Fe}$ . . . . .	41
4.2.1	The number of produced radioactive atoms . . . . .	41
4.2.2	The activity of an irradiated sample . . . . .	41
4.2.3	Correction factors for the true count rate per second . . . . .	42
4.2.4	The calculated number of $^{55}\text{Fe}$ -atoms . . . . .	43
4.2.5	The calculated isotope ratio $^{55}\text{Fe}/\text{Fe}$ . . . . .	43
4.3	Correction factors for the germanium diode . . . . .	44
4.3.1	Coincidence summing correction . . . . .	44
4.3.2	Self - attenuation . . . . .	44
<b>I</b>	<b>Part I: The production of a <math>^{55}\text{Fe}</math>-AMS standard</b>	<b>45</b>

<b>5</b>	<b>The standard production via <math>^{54}\text{Fe}(p,\gamma)^{55}\text{Co}</math></b>	<b>47</b>
5.1	Principle . . . . .	47
5.2	Preconsiderations . . . . .	47
5.3	Experimental procedure . . . . .	48
5.3.1	Samples . . . . .	48
5.3.2	Proton Irradiations at VERA . . . . .	50
5.3.3	Activity measurement of $p^+$ -irradiated samples . . . . .	53
5.4	Results and discussion for $^{54}\text{Fe}(p,\gamma)^{55}\text{Co}$ -activations . . . . .	55
5.4.1	Comparison of isotopic ratios $^{55}\text{Fe}/\text{Fe}$ , deduced from the activity measurements . . . . .	55
5.4.2	Discussion about the isotopic ratios $^{55}\text{Fe}/^{54}\text{Fe}$ . . . . .	57
5.4.3	Final Results of $^{55}\text{Fe}/^{54}\text{Fe}$ . . . . .	58
5.4.4	Measurement of the half-life of $^{55}\text{Co}$ . . . . .	59
<b>6</b>	<b>The standard production via an activity solution</b>	<b>63</b>
6.1	$^{55}\text{Fe}$ - activity standard solution . . . . .	63
6.2	Experimental procedure . . . . .	63
6.2.1	Dissolving the Fe-foils . . . . .	64
6.2.2	Dilution series . . . . .	64
6.3	Results and discussion . . . . .	66
<b>II</b>	<b>Part II: The neutron capture cross section of <math>^{54}\text{Fe}(n,\gamma)</math></b>	<b>67</b>
<b>7</b>	<b>Neutron irradiations for the <math>^{54}\text{Fe}(n,\gamma)</math>-reaction</b>	<b>69</b>
7.1	Principle . . . . .	69
7.2	Neutron irradiation at the TRIGA Mark-II reactor . . . . .	70
7.2.1	The TRIGA Mark-II reactor . . . . .	70
7.2.2	Experimental Procedure . . . . .	70
7.2.3	Results and discussion of the neutron fluence . . . . .	71
7.3	Neutron irradiation at the BRR . . . . .	73
7.3.1	The Budapest Research Reactor (BRR) . . . . .	73
7.3.2	Experimental set-up . . . . .	74
7.3.3	Experimental procedure . . . . .	74
7.3.4	Results and discussion of the neutron fluence . . . . .	76
7.4	Overview of neutron irradiated samples . . . . .	77
<b>8</b>	<b>AMS Measurements of <math>^{55}\text{Fe}</math> @ VERA</b>	<b>79</b>
8.1	Overview of the sample material . . . . .	80
8.2	Tuning procedure of $^{55}\text{Fe}$ . . . . .	82
8.3	The evaluation of acquired data . . . . .	85
8.3.1	Measured isotopic ratio . . . . .	85
8.3.2	Blank Correction . . . . .	86
8.3.3	Determination of the scaling factor $f_{std}$ . . . . .	86

---

8.3.4	Determination of the final $^{55}\text{Fe}/\text{Fe}$ -ratios of the samples . . . . .	87
8.4	Results and discussion . . . . .	88
8.4.1	Scaling factors and blank-correction factors for the beam-times . . . . .	88
8.4.2	$^{55}\text{Fe}/^{56}\text{Fe}$ versus $^{55}\text{Fe}/^{54}\text{Fe}$ . . . . .	89
8.4.3	A0, A1, A2 standards . . . . .	90
8.4.4	pg_standards . . . . .	93
8.4.5	AI06 and AI08 samples . . . . .	94
8.4.6	BP samples . . . . .	96
<b>9</b>	<b>Determination of the neutron capture cross section of <math>^{54}\text{Fe}(n,\gamma)</math></b>	<b>97</b>
9.1	Results of the cross section of $^{54}\text{Fe}(n,\gamma)$ . . . . .	97
9.1.1	Samples irradiated with thermal neutrons . . . . .	97
9.1.2	Samples irradiated with cold neutrons . . . . .	99
9.2	Discussion . . . . .	100
<b>10</b>	<b>The half-life of <math>^{59}\text{Ni}</math></b>	<b>101</b>
10.1	Introduction . . . . .	101
10.2	Scaling the half-life of $^{59}\text{Ni}$ . . . . .	102
10.3	Results . . . . .	103
10.4	Discussion . . . . .	103
<b>A</b>	<b>Appendix A</b>	<b>107</b>
A.1	Efficiency of the HPGe-diode . . . . .	107
A.1.1	Coincidence summing correction . . . . .	109
A.1.2	Results and Discussion . . . . .	112
A.1.3	Conclusions . . . . .	115
<b>B</b>	<b>Appendix B</b>	<b>117</b>
B.1	Statistics . . . . .	117
B.1.1	The arithmetic mean . . . . .	117
B.1.2	The weighted mean . . . . .	117
B.1.3	Uncertainties of the weighted mean . . . . .	118
B.1.4	Gaussian law of error propagation . . . . .	118
	<b>Bibliography</b>	<b>119</b>
	<b>Acknowledgments</b>	<b>135</b>
	<b>Curriculum vitae</b>	<b>137</b>

*Contents*

---

# 1 Introduction

## 1.1 Motivation

The main goals of this thesis are: The production of an accurate  $^{55}\text{Fe}$  reference material to provide a precise determination of the neutron capture cross section  $\sigma_{^{54}\text{Fe}(n,\gamma)}$  for thermal energies.

Dependent on the energy of the neutron, the neutron capture reaction is important for various applications:

- Neutrons in the MeV range  
are produced in fusion reactors by the fusion reactions in the DT - plasma (e.g. by  $^3\text{H}(^2\text{H},n)^4\text{He}$ ) and generate radioactive waste. It is important to know the probability to produce long-lived radioisotopes, e.g. via various neutron capture reactions.
- Neutrons in the keV range  
are present in stellar processes like the s - process, which occurs during helium burning in the phase of red giants. In this s - process, stable isotopes capture neutrons and reach radioactive isotopes, which then decay in the direction of the valley of stability. Along this valley, stable isotopes are produced from the seed element iron till bismuth. The density of the neutrons is rather low (one million neutrons per  $\text{cm}^3$ ) and leads to a rather slow neutron capture rate compared to typical half-lives of radioactive beta-minus decay. Studies of such nucleosynthesis in stellar environments are important to understand the chemical evolution of the galaxy. Typical temperatures in such star phases are  $10^8$  K, which equals Maxwellian distributed  $\approx 26$  keV neutrons ( $= k_B T$ ). The probability of capturing such neutrons is given by the cross section and lies in the range of about mbarn to barn.
- Neutrons of 0.025 eV  
are called thermal neutrons. At such a low energy, the thermal neutron capture cross section gives an important anchor for the excitation function, which is the energy dependent cross section function. Moreover this value directly enters into a determination of the half-life of  $^{59}\text{Ni}$  [Rühm *et al.*, 1994], which was performed relatively to the one of  $^{55}\text{Fe}$ . The uncertainty of that measurement was mainly dominated by the cross section value  $\sigma_{^{54}\text{Fe}(n,\gamma)}$ , which could be reduced to a level of about 3 % in this thesis.

The half-life of  $^{59}\text{Ni}$  is under discussion since a measurement of [Rühm *et al.*, 1994], whose result was discrepant to the recommended value of [Nishiizumi *et al.*, 1981]. Due to its long half-life of hundred thousand years, this cosmogenic radionuclide  $^{59}\text{Ni}$  can be used for the determination of the history of meteorites and for the investigation of the time-dependence of the solar  $\alpha$ -flux.

### 1.2 Outline

One of the main goals of this thesis is the precise determination of the thermal neutron capture cross section  $\sigma_{^{54}\text{Fe}(n,\gamma)^{55}\text{Fe}}$ .

To measure this neutron capture cross section,  $^{55}\text{Fe}$  was produced in several iron samples by irradiating them with thermal neutrons at the TRIGA-reactor Vienna and with cold neutrons at the Budapest Research Reactor BRR. The emerging isotopic ratios  $^{55}\text{Fe}/\text{Fe}$  were in the  $10^{-15} - 10^{-10}$  range and were measured via accelerator mass spectrometry (AMS) at the Vienna Environmental Research Accelerator (VERA). The  $^{55}\text{Fe}$  - AMS measurements are not interfered by the stable isobar of iron,  $^{55}\text{Mn}$ , because it does not form negative ions [Korschinek *et al.*, 1990].

The experimental focus of this thesis can be divided into two parts:

- The preparation of an  $^{55}\text{Fe}/\text{Fe}$ -AMS reference material, achieved by two independent methods, to provide absolute isotopic ratios :
  - (a) Iron samples, highly enriched in  $^{54}\text{Fe}$ , were bombarded with protons to produce via proton capture ( $p,\gamma$ )  $^{55}\text{Co}$ , which decays with a half-life of 17.53 h to  $^{55}\text{Fe}$  ( $t_{1/2}=2.74$  y). The total number of daughter-nuclides  $^{55}\text{Fe}$  was determined from the measured  $^{55}\text{Co}$ -activity.
  - (b) A certified  $^{55}\text{Fe}$ -standard-solution was diluted with iron of natural composition.
- The irradiation of iron samples with thermal neutrons and cold neutrons, and the adjacent measurement of the produced isotopic  $^{55}\text{Fe}/\text{Fe}$ -ratio via accelerator mass spectrometry. Furthermore, the reproducibility and accuracy of those  $^{55}\text{Fe}$ -AMS measurements was studied.

The neutron capture cross section is then determined by equation 1.1:

$$\sigma_{^{54}\text{Fe}(n,\gamma)} = \frac{N_{^{55}\text{Fe}}}{N_{^{54}\text{Fe}}} \cdot \frac{1}{\Phi}, \quad (1.1)$$

where  $\Phi$  is the neutron fluence (number of incident neutrons per area),  $N_{55\text{Fe}}$  is the number of produced  $^{55}\text{Fe}$ -atoms and  $N_{56\text{Fe}}$  is the number of  $^{56}\text{Fe}$ -target-atoms. The neutron fluence is determined via an activity measurement of a fluence monitor, which was irradiated simultaneously with the iron sample. The isotopic ratio  $N_{55\text{Fe}}/N_{56\text{Fe}}$  is measured via accelerator mass spectrometry.

In order to understand the physics behind all those experiments, chapter 2, **Theoretical background**, of this thesis will focus on some parts of nuclear physics:

The interaction of photons with matter is necessary for the activity measurements, the interaction of neutrons with matter is needed for the studied nuclear reaction, the neutron capture. The interaction of protons with matter is relevant, because an  $^{55}\text{Fe}/\text{Fe}$ -AMS standard will be produced by proton capture. So one chapter will treat interactions of particles with matter. The energy dependence of the cross section, known as excitation function, will be discussed in the final chapter of the theoretical introduction. The basics of all these processes are the particles themselves and will be introduced at the very beginning of chapter 2.

The next chapter 3, **Experimental background**, treats the available experimental data of the isotopes of iron and of neutron and proton capture cross sections for  $^{54}\text{Fe}$ . The Vienna Environmental Research Accelerator (VERA) and the AMS technique will also be discussed at that place.

All calculations, which are needed for the determination of the cross section, are described in chapter 4, **Mathematical background**.

After these three chapters of basic information about the theoretical, experimental and mathematical background, the work of the thesis will be described in two parts:

The first part treats two methods for the preparation of the  $^{55}\text{Fe}$ -AMS standard. The second part treats the neutron irradiations, the  $^{55}\text{Fe}$ -AMS measurements, the determination of the neutron capture cross section and finally the recalculation of the half-life of  $^{59}\text{Ni}$ .



## 2 Theoretical background

As mentioned already in the outline of the previous chapter, each experiment implies theoretical considerations. As one aim I will try to give a more general overview of the physics behind the occurring processes and then go into detail. In this regard, a brief overview about nuclear physics is given in order to understand the basic physical ideas behind the experiments of the thesis itself.

### 2.1 The basics - particles

One main topic of this diploma thesis concerns interactions of various particles. However, before the treatment of the interaction of photons with matter and of neutron and proton induced nuclear reactions, the particles itself and their properties will be discussed. As a reference for this chapter the book "Unterhaltsame Kernphysik" from Muchin [Muchin, 1974] and the book "Gamma- & X-Ray Spectrometry with semiconductor detectors" from [Debertin & Helmer, 1988] were used.

So, let's start at the very beginning:

Looking at all elemental particles one can classify them by a handful of properties: the mass, the spin, the isospin, the parity, the electrical charge, the baryon number, the lepton number, the strangeness, the magnetic momentum, the decay scheme and the life-time. To nearly each particle an anti-particle already was found. An anti-particle equals its particle in the mass, the spin and the life-time, but has the opposite sign in the electrical charge, the baryon number, the lepton number, the strangeness and the magnetic momentum. The decay scheme of the antiparticle is charge - conjugated. No matter which interactions (strong, electromagnetic and weak) between the particles take place, some of the properties are always conserved: the energy, the momentum, the angular momentum, the electrical charge, the baryon number and the lepton number.

A rough view over the particles leads to the following classification: There are photons, leptons (electron, myon, taon, their 3 neutrinos and the antileptons) and hadrons. Hadrons consist as the only one of further elemental particles called quarks. If the hadrons are build of two quarks (quark & antiquark) they are called mesons and if they are build of three quarks or three antiquarks they are called baryons. The neutron and proton belong to the baryons and have a spin and a isospin of  $1/2 \hbar$ .

Special interest lies here in the interaction of protons and neutrons with other nuclei on the one hand and the interaction of photons with matter on the other hand.

### 2.1.1 The (radioactive) atom

Three particles, the proton, the neutron and the electron form an atom. In the nucleus, the neutrons and protons are held together by the (short distant) strong force. Outside the nucleus, which has a diameter of about  $(10^{-15} - 10^{-14})$  m, the strong force decreases to zero. The negatively charged electrons are bound to the nucleus by the electromagnetic force at a distance of about  $10^{-10}$  m. The range of the electromagnetic force decreases with  $1/r^2$  (Coulomb's law) and below  $10^{-14}$  m the strength of the strong force starts to play a role. From outside, the atom is not charged because the number of protons ( $=Z$ ) equals the number of electrons.

During the conversion of nuclei,

- $\gamma$ - quanta ( $\gamma$ -radiation)

can be produced by the electromagnetic force and

- electrons, antineutrinos ( $\beta^-$ -decay corresponds to  $n \longrightarrow p + e^- + \bar{\nu}_e$ )
- positrons and neutrinos ( $\beta^+$ -decay corresponds to  $p \longrightarrow n + e^+ + \nu_e$ )

can be generated by the weak force. In the case of

- electron capture ( $EC$  corresponds to  $p + e^-_{atom} \longrightarrow n + \nu_e$ )

the nucleus captures an electron of the own shell, a neutron converts to a proton and emits a neutrino. This emitted neutrino gets the whole energy as kinetic energy and has therefore a monoenergetic energy spectrum. The neutrinos from the  $\beta^{+/-}$ -decays have a continuous energy-spectrum because they have to share the total energy with a second particle. The following important decay-modes are mentioned for completeness:

- the alpha-decay (the parent nucleus emits a  ${}^4_2He$  nucleus, which is possible by quantum tunneling),
- the isomeric decay (an excited "metastable" state has a relatively long half-life) and
- internal conversion (the excited nucleus transfers his deexcitation energy to an orbital electron, which leaves the nucleus).

### 2.1.2 Physics of photons

Photons have no mass, no electrical charge, spin  $1\hbar$  and move in empty space with the speed of light  $c$ . They are described as the force carriers of the electrodynamic force. Properties of a photon are the energy  $E$  and the momentum  $p$ . Related by  $E = pc$ , they only depend on the frequency  $\nu$  (equivalent to the wavelength  $\lambda$  through  $\nu = c/\lambda$ ), see 2.1:

$$E = h \cdot \nu = h \cdot c/\lambda \quad (2.1)$$

Compared to visible light, which is in the range of hundred nanometers, X-rays are in the range of about  $10^{-8} - 10^{-11}$  m and  $\gamma$ -rays in the range of  $< 10^{-11}$  m. These ranges are in the order of the size of atoms [diameter  $10^{-10}$  m] and nuclei [diameter  $10^{-14}$  m].

#### $\gamma$ -rays

X-rays lie between some eV and hundred keV, whereas  $\gamma$ -rays are going from some tens of keV upwards. But in general, the distinction between X- and Gamma-rays lies in their origin. While X-rays are emitted "in transitions of the atomic electron different states in an atom" [Debertin & Helmer, 1988], gamma-rays "are produced by transitions from excited states in a nucleus" [Debertin & Helmer, 1988].

Looking at the "birth" of a  $\gamma$ -ray, one has to know what happens during a gamma-ray transition. Which properties have to be conserved? Which properties are there?

Properties of nuclear states can be listed as follows:

- level energies  $E$
- half-lives  $t_{1/2}$
- spin  $\vec{J}$  with  $|\vec{J}| = (\sqrt{J(J+1)}) \cdot \hbar$
- parity  $\Pi$

A transition from an initial state  $i$  to a final state  $f$  of a nucleus leads to following properties which can be related to the emitted  $\gamma$ -rays:

- $\gamma$ - energies  $E_\gamma$
- emission probability  $p_\gamma$
- angular momentum  $\vec{L}$
- multi polarity  $\Pi_\gamma$

In the gamma-ray emission process the energy  $E$ , the momentum  $\vec{p}$ , the angular momentum  $\vec{L}$  and the parity have to be conserved (see 2.5, 2.2, 2.3 and 2.4):

$$|\vec{p}_\gamma| = |\vec{p}_{nucleus}| \quad (2.2)$$

$$\vec{J}_i = \vec{J}_f + \vec{L}_\gamma \quad (2.3)$$

$$\Pi_i = \Pi_f - \Pi_\gamma \quad (2.4)$$

Due to the fact that the mass of the photon is zero, the recoil energy becomes negligible. The difference between the initial and final energy state of the nucleus ( $E_i$  and  $E_f$ ) results in the energy of the gamma-ray.

$$E_\gamma = E_i - E_f - E_{recoil} \quad \text{with} \quad E_{recoil} \rightarrow 0 \quad (2.5)$$

The ratio between the energy and the momentum of a massless(!) particle equals the speed of light in vacuum (see 2.6):

$$E = p \cdot c \quad (2.6)$$

### Interaction of photons with matter

Once emitted, a  $\gamma$ -quant will pass through matter and interact with it. Depending on the energy of the photon and the atomic number of the matter, the photoelectric absorption (also called photo effect), the Comptoneffect and the pair production will replace each other as the dominant interaction process.

- An photon of low energy will mainly experience the photo effect: The whole energy of the photon is absorbed by an atomic electron (for the absorption of the photon by a free electron it would not be possible to conserve the energy and the momentum!), which will leave the atom with the photons energy minus the binding energy (neglecting the recoil energy). The free electron will pass through matter and lose energy with every collision it undertakes with the matter. But on the other hand the electron left a vacancy in the atom's shell which will be refilled by an electron from an outer shell, releasing his binding energy in form of X-rays (or Auger-electrons), which also will be absorbed by matter. The interaction cross section is strongly  $Z$  dependent (see figure 2.1).
- The Compton scattering of a photon (dominant, e.g. for 150 keV - a few MeV photons in germanium with  $Z = 32$ , see also figure 2.2) takes place at a "free" electron. After the interaction, the photon has a lower energy, therefore a bigger wavelength and the electron obtains energy. The difference between the energy of the incident and scattered photon is described by formula 2.7 and defines the energy of the electron. The maximal energy transfer occurs at a

scattering angle of  $180^\circ$  (see formula 2.8) and is also known as the Compton edge in Gamma spectra (see figure 2.3).

$$E_{e^-} = E_\gamma - E_{\gamma'} = E_\gamma - \frac{E_\gamma}{1 + \frac{E_\gamma}{m_e c^2} \cdot (1 - \cos\Theta)} \quad (2.7)$$

$$E_e^-(180^\circ) = \frac{E_\gamma}{1 + \frac{m_e c^2}{2E_\gamma}} \quad (2.8)$$

- The third process requires a minimum energy of  $\geq 2m_e c^2$  within an electric field of an atom to produce an electron and a positron. The greater the kinetic energy of the photon the bigger the kinetic energy of the two particles. After the positron loses its kinetic energy it annihilates with a (loosely bound) electron into two  $\gamma$ -quanta (2 · 511 keV). (The total energy of both  $\gamma$ -quanta is a bit less than  $2m_e c^2$  because of the small energy transfer to the atom of the electron. Moreover the electron movement in the orbit of the atom at the moment of the annihilation leads to the Dopplereffect, which causes a natural variation of the  $\gamma$  - energy of about  $\pm 2$  keV.)

### Photon attenuation

The number of photons  $N$ , which do not suffer energy and direction losses after crossing a layer of matter, is given by equation 2.9. The amount of photons penetrating a layer of matter decreases exponentially with the thickness and the mass of the target.

$$N = N_0 e^{-\mu t} = N_0 e^{-\frac{\mu}{\rho} \cdot t \rho} \quad (2.9)$$

$N_0$  is the number of incident photons,  $N$  is the number of photons of the same energy after penetrating a layer of matter of thickness  $t$  [cm] with density  $\rho$  [g cm<sup>-3</sup>].  $\frac{\mu}{\rho}$  is the attenuation mass coefficient (see figure 2.1) given in  $\text{cm}^2 \text{g}^{-1}$  and  $t\rho$  is the mass per unit area [g cm<sup>-2</sup>].

The correction factor to account for the loss of  $\gamma$ -rays in a sample is given in equation 2.10, taken from [Debertin & Helmer, 1988].

$$C = \frac{\mu t}{1 - e^{-\mu t}} \quad (2.10)$$

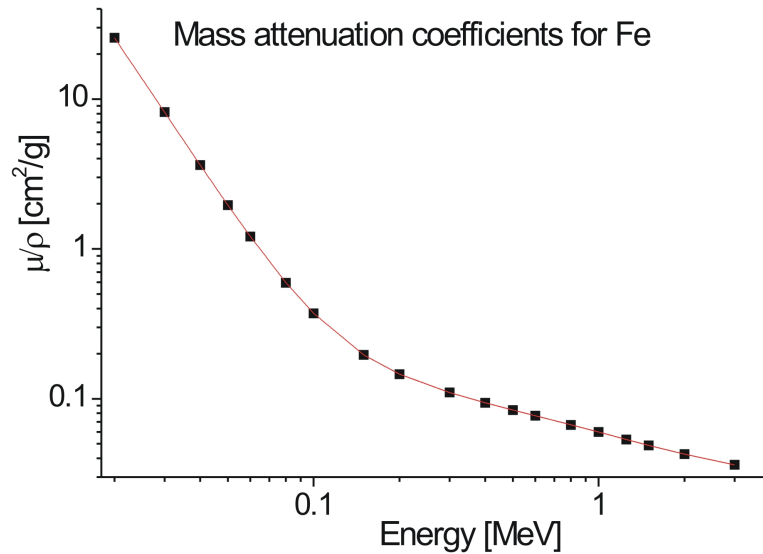


**Figure 2.1:** Mass attenuation coefficient in iron dependent on the photons energy (double logarithmical scale), taken from [Hubbel & Seltzer, 1996]. Compare the total attenuation for Ge in figure 2.2

### Detection of $\gamma$ -rays

The most common detectors used for the detection of photons are:

- Gas detector  
(low density material, moderately small thickness, low efficiency)
- NaI(Tl) scintillator  
(high  $Z$  material, high  $\rho$  density, large thickness)
- High purity Ge semiconductor detector  
( $Z_{Ge} > Z_{Si(Li)}, \rho_{Ge} > \rho_{Si(Li)} \rightarrow$  Ge is better for photons of higher energy)
- Ge(Li) semiconductor detector
- Si(Li) semiconductor detector

No matter which detector is used, one can describe the processes of detection as follows:

#### 1) $E_\gamma \rightarrow E_{e^-}$

As the  $\gamma$ -ray traverses matter it will interact with the atoms via the just mentioned "photoelectric absorption", "compton scattering", "pair production" and its energy

(as far as the detector material can stop the  $\gamma$ -ray inside the detector material) will be converted into the kinetic energy of  $e^-$  ( $e^+$ ).

Figure 2.2 shows the linear attenuation coefficient in Ge for the photoelectric effect, Compton scattering and pair production. The values are taken from XCOM: Photon Cross Sections Database [M.J. Berger & Zucker, 1990].

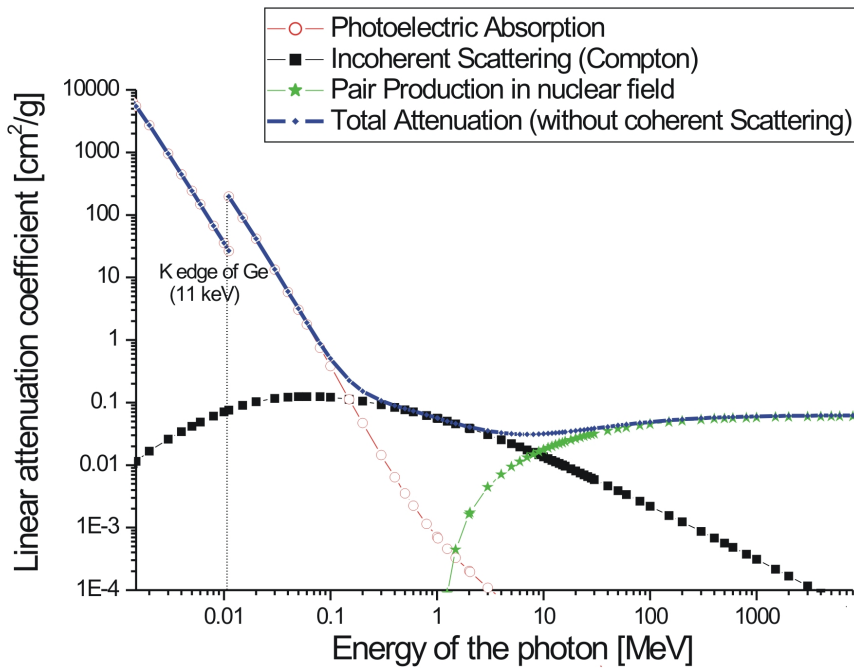


**Figure 2.2:** Linear attenuation coefficients in Ge (Photon Cross Sections for photoelectric effect, Compton Scattering and pair production given in  $cm^2/g$ ). Data taken from [M.J. Berger & Zucker, 1990].

## 2) $E_{e^-} \rightarrow$ charge carriers or light

Then the high energetic primary electrons will either ionize the detector material and therefore produce charge carriers (electron-ion pairs; electron-hole pairs) or they will excite molecular states and therefore produce indirectly light (emitted in the deexcitation). The production of the electron-ion / electron-hole pairs is a statistical process. Using a gas counter one needs around 30 eV to produce an electron-ion pair versus around 3 eV to produce an electron-hole pair in a semiconductor detector. The production of a photon in a NaI scintillator requires around 100 eV. (Those numbers are taken from [Debertin & Helmer, 1988]) A high energetic photon will produce more charge carriers than a low energy photon.

### 3) Collection and measurement of the charge carriers or the light

Finally, the formed charge carriers (both electrons and holes in the case of semiconductor detectors) are collected by applying an electric field (bias supply voltage) across the detector. (The conversion of the electrical signal into a digital one is done with a typical signal processing, which includes a preamplifier, an amplifier, an ADC (Analog to Digital Converter) and a Multi-Channel Analyzer).

Figure 2.3 shows a typical energy dispersive  $\gamma$ -ray spectrum of a monoenergetic emitter, measured by a lead shielded high purity germanium detector. Compton scattering is the main interaction mode for  $\gamma$ -rays between 150 keV and 10 MeV (see figure 2.2). The typical shape of a spectrum, shown in figure 2.3 can be explained as follows:

- **The full energy peak**  
is the result if the whole energy of the incident  $\gamma$ -ray is converted to electron-hole pairs, and nothing escapes from the sensitive volume of the detector. (In the case of a X-ray escape peak only the Ge-X-ray escapes from the detector material. Trapping effects and charge-collection losses can be neglected [Debertin & Helmer, 1988].
- **Compton scattering continuum to the Compton edge**  
corresponds to absorbed electrons with energy values lying between zero and  $\frac{E_\gamma}{1 + \frac{m_e c^2}{2E_\gamma}}$  (see equation 2.7 and 2.8) when the  $\gamma$ -rays leaves the detector. The compton edge refers to the Compton electrons of maximal energy.
- **Continuum between the Compton edge and the full energy peak**  
corresponds to the scattered photons with energies lying between  $\frac{E_\gamma}{1 + \frac{m_e c^2}{2E_\gamma}}$  and  $E_\gamma$  (see equation 2.7 and 2.8).
- **Pile - Up Signals**  
occur if the electronics cannot resolve two different signals originating from  $\gamma$ -rays (in time) and therefore treat them as one  $\gamma$ -ray with a corresponding higher energy.
- **Pair Production**  
plays a role above 1.5 MeV. In general, corresponding to the full energy peak one finds the single escape peak at  $E - m_e c^2$  and the double escape peak at  $E - 2m_e c^2$  if both, the electron and the positron, escape from the detector.

The probability, that a  $\gamma$ -ray of the energy  $E_\gamma$  produces a full energy peak with the net peak area  $N$  (registered detector counts inside the full energy peak minus the background) is known as the full energy peak efficiency of a detector. A typical efficiency curve, which is the efficiency versus the energy of the photon, is shown in figure A.1 for a high purity germanium detector.

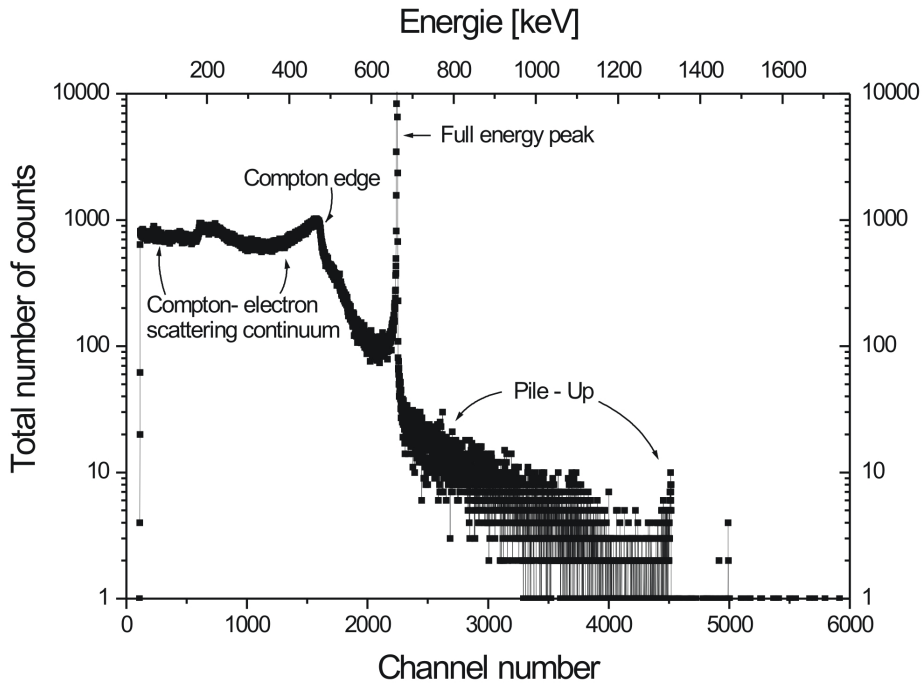


**Figure 2.3:** Typical spectrum of a monoenergetic *gamma*-ray source ( $^{137}\text{Cs}$ ), acquired by a high purity germanium detector (shielded with lead).

### 2.1.3 Interactions of particles in matter

In this section, possible interactions of particles in matter are discussed. Compared to a photon, which is only affected by the electromagnetic force, particles with mass can be affected by the strong force (if composed of quarks, e.g. neutron, proton), the electromagnetic force (if charged, e.g. proton, electron (neutron is also affected but only because of its magnetic momentum)) and the weak force. The proton and neutron will serve as examples for charged and uncharged particles .

#### Protons

Depending on the distance between the charged projectile and a target, those forces can lead to the following most important interactions:

- distance  $> 10^{-10}\text{m}$ : Coulomb's law  $\propto \frac{1}{r^2}$ :  
 → **Inelastic electromagnetic interaction between the proton and the atomic electrons** leads to the ionization of the atom and is described by the formula of Bethe and Bloch (see equation 3.7). The proton reaches the maximum of energy loss at the end of its path (described by the Bragg curve).

- distance  $\geq 10^{-14}$ m: strong force  $\longrightarrow 0$ , coulomb's law  $\propto \frac{1}{r^2}$ :  
→ **Elastic electromagnetic (Coulomb-) scattering due to the positive charge of the nucleus** (proton loses much more energy per distance than in the previous process).
- distance  $\approx 10^{-15}$ m: strong force:  
→ **Nuclear reaction** possible (besides the elastic or inelastic scattering) (will be discussed in more detail in section 2.2).

Inelastic scattering always leads to the excitation of the atom and therefore to a loss of the projectiles incident kinetic energy. If a proton approaches an electron, there exists a small probability for a weak interaction  $e^- + p^+ \longrightarrow \nu_e + n$  (called inverse  $\beta$ -decay). Two additional processes caused by the electromagnetic force have to be mentioned: Bremsstrahlung (emitted photons if charged particles change their velocity or their direction, intensity increases quadratically with lower mass) and Cherenkov radiation (if a charged particle's speed exceeds the speed of light in the medium).

### Neutrons

The strong and weak force will have a much bigger influence on the neutron compared to the electromagnetic force (which only affects the neutron because of its magnetic momentum). The main interactions are:

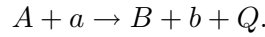
- **Elastic scattering at nuclei**
- **Inelastic scattering at nuclei**
- **Nuclear reactions**, e.g. neutron capture (see chapter 2.2 and figure 3.3)

The relative probability of these interaction modes changes with the energy of the neutron. A high energy neutron will scatter with a high probability and when slowing down, the probability for being captured, increases. Besides, the energy of the neutrons can be classified as follows:

- cold neutrons ( $E_{cold,n} < meV$ )
- thermal neutrons = neutrons at room temperature  $\approx 20^\circ$  ( $E_{th,n} \approx 0.025$  eV =  $\frac{1}{40}$  eV)
- epithermal neutrons ( $0.025$  eV  $\leq E_{epith,n} \leq 1$  keV)
- fast neutrons ( $E_{fast,n} \approx$  keV, MeV)

## 2.2 Nuclear Reactions

A common notation for a nuclear reaction is:



The projectile  $\mathbf{a}$  is bombarded onto target nucleus  $\mathbf{A}$  and produces an (excited) nucleus  $\mathbf{B}$  by emitting a particle  $\mathbf{b}$ . The incident particle  $\mathbf{a}$  and the target nucleus  $\mathbf{A}$  form the initial state  $i$  and the outgoing particle  $\mathbf{b}$  and the (excited) nucleus  $\mathbf{B}$  form the final state  $f$ . Throughout the thesis, the following notation will be used for nuclear reactions:  $\mathbf{A}(\mathbf{a},\mathbf{b})\mathbf{B}$  (e.g.  ${}^{54}\text{Fe}(n, \gamma){}^{55}\text{Fe}$ ).

The difference between the rest-masses of the incoming reaction channel ( $m_a c^2$  and  $m_A c^2$ ) and the outgoing reaction channel ( $m_b c^2$  and  $m_B c^2$ ) is described by the Q-value. If it is greater than zero, energy is released (exothermic reaction). If it has a negative value, one has to provide energy to make the reaction possible (endothermic reaction) and  $|Q|$  equals then the minimum center-of-mass energy needed for the nuclear reaction. In the laboratory system for endothermic reactions, however, where the target nucleus rests, the minimal kinetic energy  $E_{a,min}$  of the incident particle is greater than the Q-value, because a part of the kinetic energy is used to conserve the momentum of the center of mass. That minimal kinetic energy is called threshold energy and is given in equation 2.11. For a more detailed description see [Segré, 1977].

$$E_{a,min} = E_{threshold} = |Q| \left(1 + \frac{m_a}{m_A}\right) \quad (2.11)$$

Dependent on the interaction time of a nuclear reaction, different models are used for description. If a nuclear reaction occurs within the transit time of the projectile through the nucleus, it is called a **direct reaction** [ $\approx 10^{-22}$ s]. Some typical examples of direct reactions are:

- kick off, e.g. (n,p)
- stripping, e.g. (d,p)
- pick up, e.g. (p,d).

**Compound nuclear reactions** take place, if there is enough time to distribute the whole energy of the incident projectile among all the nucleons of the target nucleus [ $\approx 10^{-16}$ s]. This type of nuclear reaction takes place as long as the mean free path of the incident particle  $\mathbf{a}$  is smaller than the radius of the nucleus  $\mathbf{A}$ , which corresponds to kinetic energies of the projectile below 50 MeV.

A mixture of both types of nuclear reactions occurs in **preequilibrium reactions**, which take place at an energy scale of about (10 - 200) MeV. The projectile reacts only with some nucleons of the target and does not stay in the nucleus until the thermal equilibrium of the nucleons is reached. For projectiles with higher energy,

**spallation reactions** [above 200 MeV] and **fragmentation** [above 500 MeV] are possible.

In this work, only capture processes will be of importance, especially the neutron and the proton capture:  $(n,\gamma)$  and  $(p,\gamma)$ . If the incident projectile has the energy, which is needed to reach a excited state of the compound nucleus, resonances occur and cause a large rise of the cross section for a small energy region. In the energy region, which is used for neutron capture (thermal neutrons) and proton capture (several MeV) in this work, resonances don't occur and thus, were not important.

### 2.2.1 The cross section

The main quantity, which describes a nuclear reaction, is the nuclear cross section  $\sigma$ . It describes the probability to produce the nucleus **B** as reaction product of the nuclear reaction  $A(a,b)B$ . The number of nuclear reactions equals the number of produced nuclei  $N_B$  and increases with the number of incident projectiles  $N_a$  per unit of area (= fluence  $\Phi$ ), with the number of target atoms  $N_A$  and with the probability of the interaction  $\sigma$  between these nuclei (given in an unit of area):

$$N_B = N_a/(cm^2) \cdot \sigma_{ab}(E) \cdot N_A = \Phi \cdot \sigma_{ab}(E) \cdot N_A. \quad (2.12)$$

The reaction rate per time unit,  $R$ , equals the number of produced radionuclides  $N_B$  per time unit:

$$R = N_a/(cm^2)/s \cdot \sigma_{ab}(E) \cdot N_A = \varphi \cdot \sigma_{ab}(E) \cdot N_A, \quad (2.13)$$

where the flux  $\varphi$  is the number of incident particles per time and per area and can be replaced by the product of the number of incident particles per volume  $n_a$  and their velocity  $v_a$ . The total reaction rate per time and volume unit,  $r$ , can be described by:

$$r = \varphi \cdot \sigma_{ab}(E) \cdot n_A = n_a v_a \cdot \sigma_{ab}(E) \cdot n_A, \quad (2.14)$$

where  $n_A$  is the number of target nuclei per volume. The dimension of the cross section is an area. It is convenient to use barn as unit, which equals  $10^{-28} m^2 = 10^{-24} cm^2$ , approximately the area of a nucleus.

From the theoretical point of view (based on [Segré, 1977]), the transition probability per time unit,  $w$ , from an initial state  $i$  to a final state  $f$  can be described by Fermis golden rule:

$$w_{i \rightarrow f} = \frac{2\pi}{\hbar} \langle |H_{if}|^2 \rangle \frac{dn}{dE}. \quad (2.15)$$

The density of the final states  $dn/dE$  in the finite volume  $\Omega$  is:

$$\frac{dn}{dE} = \frac{4\pi\Omega}{(2\pi\hbar)^3} p_b^2 \frac{dp_b}{dE}, \quad (2.16)$$

where  $p_b$  is the momentum of the free particle  $\mathbf{b}$ .  
 $\langle |H_{if}|^2 \rangle$  is the average value of the square of the matrix element  $H_{if}$ , which is a transition rate and described by:

$$H_{if} = \int \psi_f^* U \psi_i d\tau, \quad (2.17)$$

where  $\psi_f^*$  and  $\psi_i$  are the wave functions of the initial and final states and are normalized in the volume  $\Omega$ .  $U$  is the interaction energy in the region of the nucleus. Only this small region of the nucleus contributes to the matrix element  $H_{if}$ , which is approximately described by:

$$H_{if} = \frac{\langle U \rangle \cdot (\text{vol.nucleus})}{\Omega} \cdot e^{-G_a - G_b}, \quad (2.18)$$

where  $\langle U \rangle$  is an average of the interaction energy over the nuclear volume. The exponential term  $e^{-(G_a + G_b)}$  is the coefficient of transmission and describes the reduction of the wave function at the nucleus by the Coulomb repulsion, where

$$G_a \cong \frac{\pi Z_A Z_a e^2}{\hbar v_a} \quad (2.19)$$

is the Gamow Factor and describes the probability that a particle  $\mathbf{a}$  overcomes the Coulomb barrier of the nucleus  $\mathbf{A}$ .

Going back to equation 2.14, the transition probability,  $w$ , can be described in terms of the cross section  $\sigma$  by:

$$w_{i \rightarrow f} = n_a v_a \sigma_{A \rightarrow B}. \quad (2.20)$$

Comparing equation 2.15 - 2.18 with equation 2.20, the cross section is written now as a function of the velocity of the incident particle (non relativistic result):

$$\sigma_{ab} \propto \frac{p_b^2}{v_a v_b} \cdot e^{-2(G_a + G_b)} \quad (2.21)$$

$p_b$  ... momentum of the ejectile  
 $G_a, G_b$  ... Gamow Factor of the incident particle a and outgoing particle b  
 $e^{-(G_a + G_b)}$  ... transmission coefficient

Using equation 2.21, the cross section can be discussed as a function of the velocity or energy (= excitation function) of the incident (neutral or charged) particle. Various cases are discussed below and plotted in figure 2.4 (see [Segré, 1977] for more details).

**a) Uncharged incoming particles:**

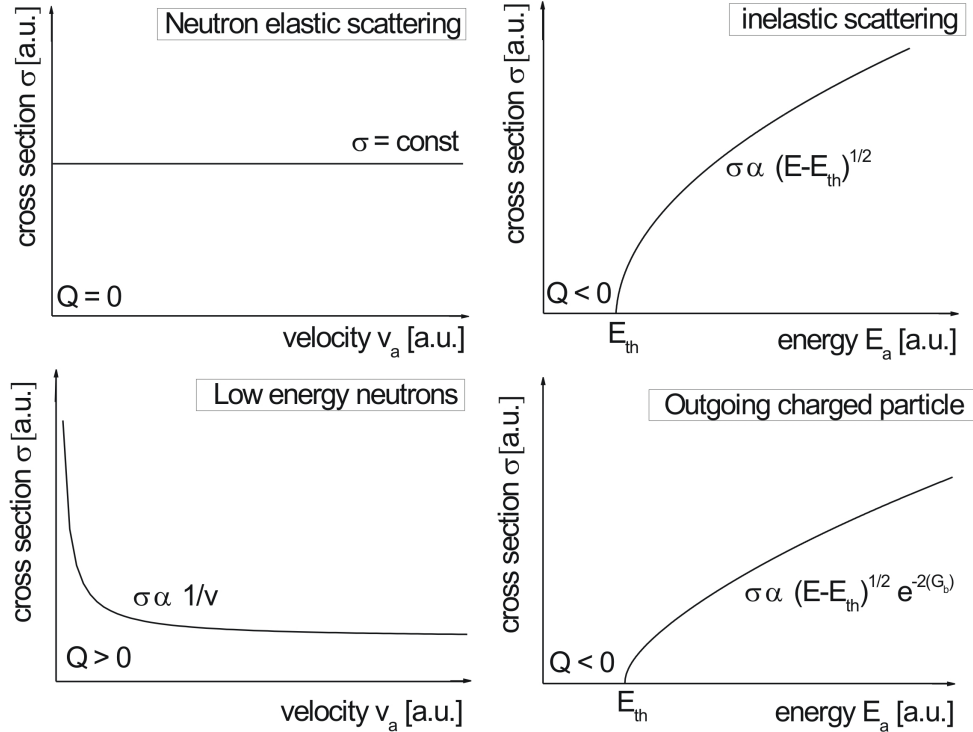
$G_a = 0$ , because the neutrons are not affected by the Coulomb barrier

- **Elastic scattering** (n,n) if  $Q = 0$   
 $v_a = v_b \longrightarrow \sigma_{ab} = \text{const}$  at low energy
- **Low energy projectile** (n, $\alpha$ ), (n,p), (n, $\gamma$ ) if  $Q > 0$ ,  $E_a \ll Q$ :  
 ( $v_b = \text{const}$  and  $e^{-2G_b} = \text{const}$  because it depends on the almost constant energy of the ejectile.)  
 $\longrightarrow \sigma_{ab} \propto \frac{1}{v_a}$
- **Inelastic scattering** (n,n') if  $Q < 0$ :  
 (the necessary kinetic energy of the projectile:  $E_{min}^a = -Q(1 + \frac{m_a}{m_A})$ )  
 Valid for particles having a kinetic energy slightly above the threshold energy, where  $v_a \cong \text{const}$  and  $v_b \propto \sqrt{E_a - E_{a,min}}$   
 $\longrightarrow \sigma_{ab} \propto \frac{p_b^2}{v_a v_b} \propto \sqrt{E_a - E_{a,min}}$
- **Outgoing charged particle** (n, $\alpha$ ), (n,p) if  $Q < 0$ :  
 (The difference between this reaction and the inelastic scattering is, that  $e^{-G_b}$  is a dominant parameter)  
 $\longrightarrow \sigma_{ab} \propto \sqrt{E_a - E_{min}^a} \cdot e^{-2(G_a + G_b)}$

**b) Charged incoming particles:**

- **Exothermic reaction** (p,n), ( $\alpha$ ,n), (p, $\gamma$ ) if  $Q > 0$ :  $E_a \ll Q$ :  
 ( $\frac{p_b^2}{v_b} \cdot e^{-2G_b} = \text{const}$ )  
 $\longrightarrow \sigma_{ab} \propto \frac{1}{v_a} \cdot e^{-(2G_a)}$

**A) Incident particles are neutral ( $G_a = 0$ ):**



**B) Incident particles are charged:**

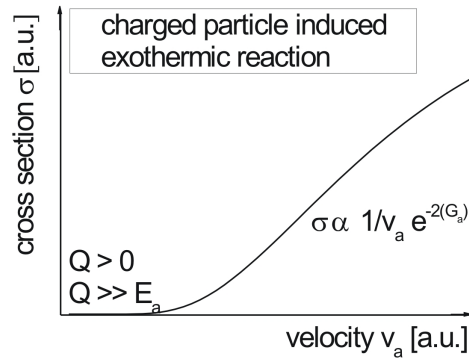


**Figure 2.4:** The behaviour of the cross section at low energy versus the velocity  $v$  or energy  $E$  of the incident particle. The four upper plots are excitation functions for neutral incident particles in the case of  $Q = 0$ ,  $Q > 0$  and  $Q < 0$ . The plot at the bottom shows the excitation function for a charged incident particle in the case of  $Q > 0$ .



### 3 Experimental background

In this chapter, natural abundances of the stable isotopes of iron, decay data of the radioactive isotope  $^{55}\text{Fe}$  and the experimental data set of neutron and proton capture cross sections on  $^{54}\text{Fe}$  are described. A section will also describe the Vienna Environmental Research Accelerator, VERA, where proton irradiations and the  $^{55}\text{Fe}$ -AMS measurements were carried out.

#### 3.1 Iron and its isotopes

One finds iron in the fourth period, the eighth group of the periodic table and it belongs to the transition metals. It has a density of  $7.874 \text{ g/cm}^3$ . Having an atomic number of 26 (=number of protons) one finds four stable isotopes Mn ( $Z = 25$ ) and cobalt Co ( $Z = 27$ ) (see figure 3.1). The most abundant isotope is  $^{56}\text{Fe}$  with 91.75%, followed by  $^{54}\text{Fe}$  with 5.85%,  $^{57}\text{Fe}$  with 2.12% and  $^{58}\text{Fe}$  with 0.28% (see table 3.1 for isotopic compositions and atomic masses [Rosman & Taylor, 1997],[Coplen *et al.*, 2002],[Wieser, 2006]).

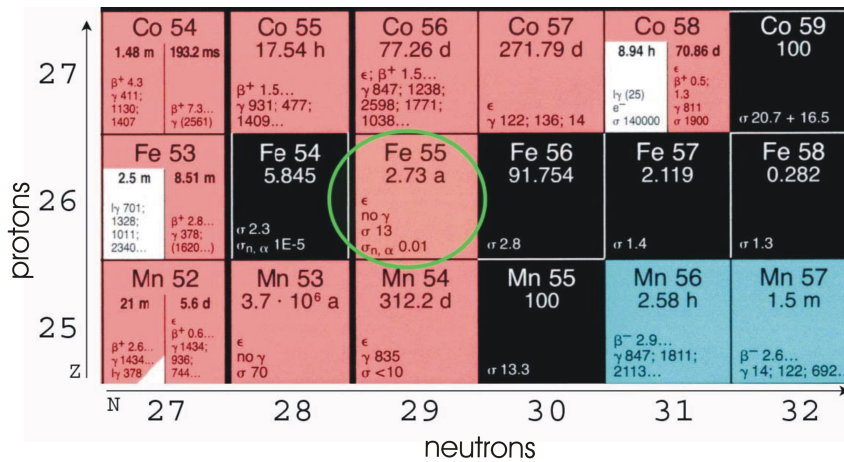


**Figure 3.1:** Extract from the chart of nuclides [Magill *et al.*, 2006] showing the isotopes of iron. The number of protons is plotted against the number of neutrons.

	isotope abundances [%]	atomic mass [u]
$^{54}\text{Fe}$	5.845(23)	53.94
$^{56}\text{Fe}$	91.754(24)	55.93
$^{57}\text{Fe}$	2.1191(65)	56.94
$^{58}\text{Fe}$	0.2819(27)	57.93
natural Fe	-	55.845(2)

**Table 3.1:** Stable isotopes of natural iron. The data for the isotopic composition is taken from [Rosman & Taylor, 1997] and the atomic mass data is taken from [Coplen *et al.*, 2002].

In this work, the isotope of interest is the radioactive  $^{55}\text{Fe}$ , which decays with a half-life of  $(2.744 \pm 0.009)$  years [Junde, 2008] by electron capture to the stable manganese  $^{55}\text{Mn}$  with a negligible  $\gamma$ -ray emission ( $10^{-7}\%$ ). The decay scheme is shown in figure 3.2.

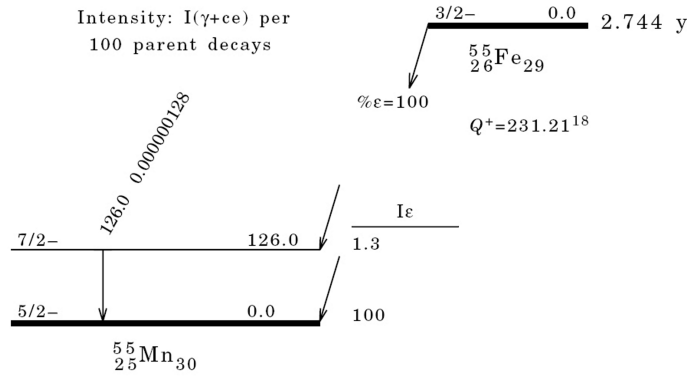


**Figure 3.2:** Decay scheme of  $^{55}\text{Fe}$  taken from [Junde, 2008]

### 3.2 Nuclear reactions on $^{54}\text{Fe}$

Two different nuclear reactions on  $^{54}\text{Fe}$  are of importance in the course of the thesis:

- $^{54}\text{Fe}(n,\gamma)^{55}\text{Fe}$
- $^{54}\text{Fe}(p,\gamma)^{55}\text{Co}$

The first one, the neutron capture on  $^{54}\text{Fe}$ , produces the radioactive isotope  $^{55}\text{Fe}$ . The AMS-measurement of the produced isotopic ratio  $^{55}\text{Fe}/^{54}\text{Fe}$  in combination with the neutron fluence data give the value of the thermal neutron capture cross section.

The second reaction, proton capture on  $^{54}\text{Fe}$ , produces radioactive  $^{55}\text{Co}$ -atoms, which decay by electron capture with a half-life of 17.53 h to  $^{55}\text{Fe}$ . An activity measurement of the produced radionuclide  $^{55}\text{Co}$  allows to calculate the isotopic ratio  $^{55}\text{Fe}/\text{Fe}$  and by this way an  $^{55}\text{Fe}$ -AMS standard of known isotopic ratio is produced.

In the next subsections both cases will be discussed in detail.

### 3.2.1 Neutron capture $^{54}\text{Fe}(n,\gamma)^{55}\text{Fe}$

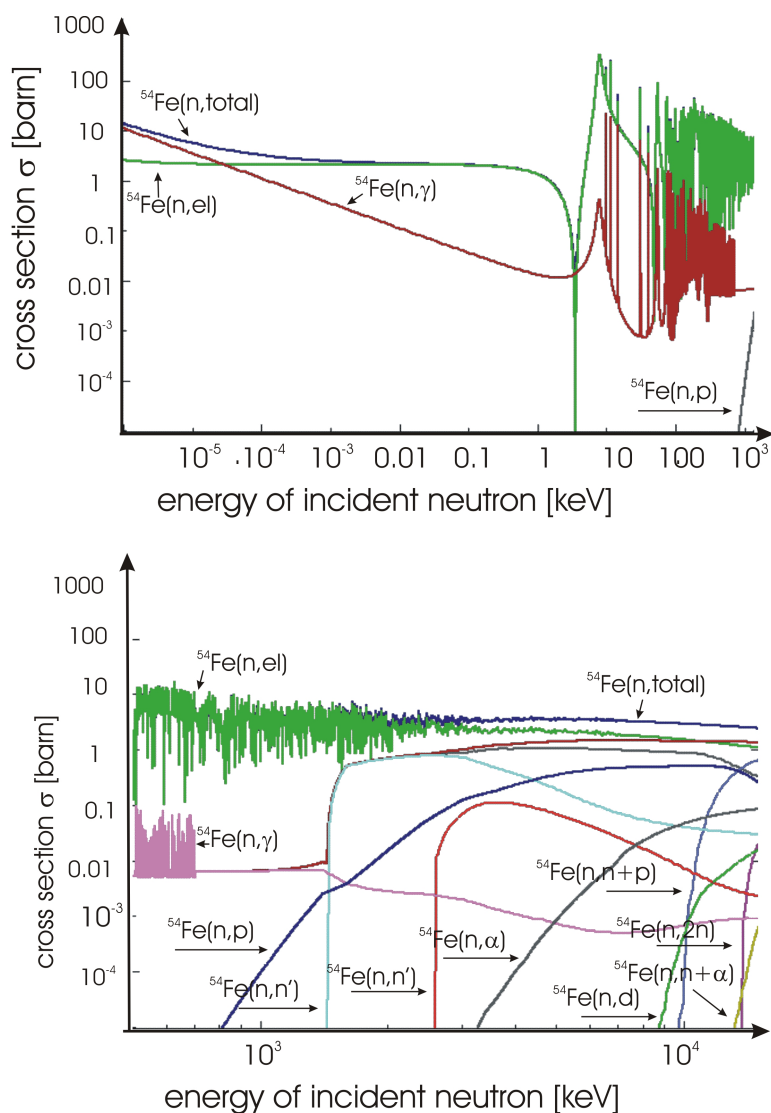


**Figure 3.3:** Some excitation functions of  $^{54}\text{Fe}(n,*)$ -reactions, taken from [Chadwick *et al.*, 2006]. The cross sections for the individual neutron induced reactions are plotted against the incident neutron's energy. The scales are both logarithmic.

When neutrons are bombarded on  $^{54}\text{Fe}$ , various nuclear reactions will take place. Data given in the "Evaluated Nuclear Data Formats" ENDF/B-VII.0 were used to find all those neutron induced nuclear reactions in dependence on the energy of the

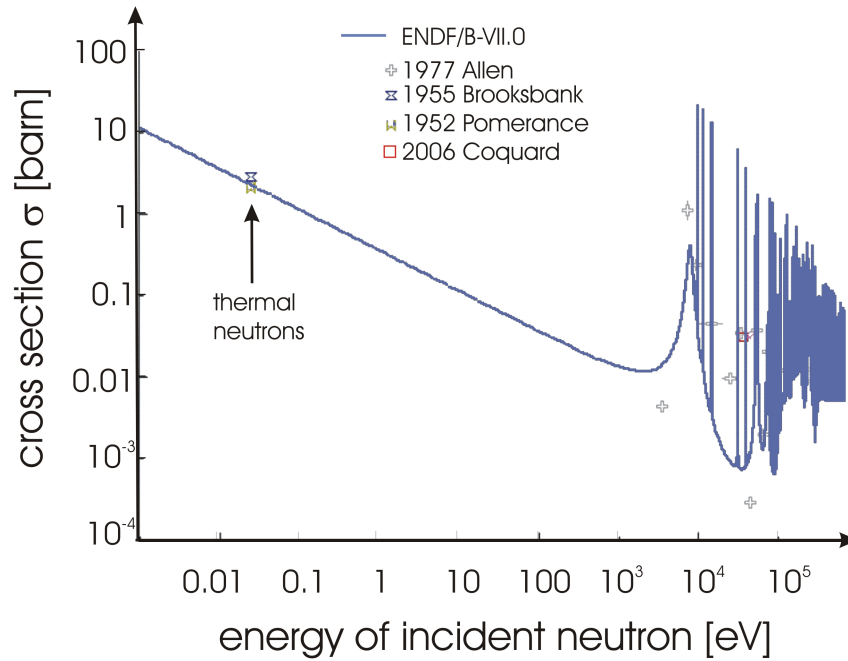
incident neutron. Figure 3.3 shows these excitation functions for neutron energies between 0.1 meV and 12 MeV. Below 1 keV only the (n,el) and (n, $\gamma$ )-reactions are competing, whereas (n, $\gamma$ ) decreases with  $1/v_n$  (as discussed in section 2.2). The resonances for the scattering and capture reactions observed between 10 keV and 1 MeV, are due to the excited states of the daughter nucleus. At few MeV, other nuclear reactions become dominant: the (n,p)-reaction, the inelastic scattering (n,n') (as  $Q < 0$ ), then the (n,d), (n,n+ $\alpha$ ), (n,n+p) and (n,2n) reactions are energetically possible as well.

Table 3.2 shows the specific open reaction channels for neutron induced reactions on all stable iron isotopes. It demonstrates, that for neutrons below 10 MeV no competing nuclear reaction channel exists to produce  $^{55}\text{Fe}$ .

$E_{th}$ [MeV]	Q-value [MeV]	$^{54}\text{Fe}(\text{n},*)$	products	$t_{1/2}$
0.00	9.30	(n, $\gamma$ )	$^{55}\text{Fe}$	2.74 y
0.00	0.84	(n, $\alpha$ )	$^{51}\text{Cr}$	27.70 d
0.00	0.09	(n,p)	$^{54}\text{Mn}$	312 d
0.00	0.00	(n,n)	$^{54}\text{Fe}$	stable
6.75	-6.63	(n,d)	$^{53}\text{Mn}$	$3.74 \cdot 10^6$ y
7.61	-7.47	(n,2p)	$^{53}\text{Cr}$	stable
7.84	-7.70	(n, $^3\text{He}$ )	$^{52}\text{Cr}$	stable
8.25	-8.10	(n,2 $\alpha$ )	$^{47}\text{Ti}$	stable
8.58	-8.42	(n,n+ $\alpha$ )	$^{50}\text{Cr}$	$>1.3 \cdot 10^{18}$ y
8.84	-8.67	(n,p+ $\alpha$ )	$^{50}\text{V}$	$1.4 \cdot 10^{17}$ y
9.02	-8.85	(n,n+p)	$^{53}\text{Mn}$	$3.74 \cdot 10^6$ y
$E_{th}$ [MeV]	Q-value [MeV]	$^{56}\text{Fe}(\text{n},*)$	products	$t_{1/2}$
0.00	7.65	(n, $\gamma$ )	$^{57}\text{Fe}$	stable
0.00	0.33	(n, $\alpha$ )	$^{53}\text{Cr}$	stable
0.00	0.00	(n,n)	$^{56}\text{Fe}$	stable
2.97	-2.91	(n,p)	$^{56}\text{Mn}$	2.58 h
7.75	-7.61	(n,n+ $\alpha$ )	$^{52}\text{Cr}$	stable
8.10	-7.96	(n,d)	$^{55}\text{Mn}$	stable
8.98	-8.83	(n,2 $\alpha$ )	$^{49}\text{Ti}$	stable
$E_{th}$ [MeV]	Q-value [MeV]	$^{57}\text{Fe}(\text{n},*)$	products	$t_{1/2}$
0.00	10.04	(n, $\gamma$ )	$^{58}\text{Fe}$	stable
0.00	2.40	(n, $\alpha$ )	$^{54}\text{Cr}$	stable
0.00	0.00	(n,n)	$^{57}\text{Fe}$	stable
1.94	-1.91	(n,p)	$^{57}\text{Mn}$	85.4 s
5.63	-5.53	(n,2 $\alpha$ )	$^{50}\text{Ti}$	stable
7.45	-7.32	(n,n+ $\alpha$ )	$^{53}\text{Cr}$	stable
7.78	-7.65	(n,2n)	$^{56}\text{Fe}$	stable
8.48	-8.33	(n,d)	$^{56}\text{Mn}$	2.58 h
9.51	-9.35	(n,t)	$^{55}\text{Mn}$	stable
$E_{th}$ [MeV]	Q-value [MeV]	$^{58}\text{Fe}(\text{n},*)$	products	$t_{1/2}$
0.00	6.58	(n, $\gamma$ )	$^{59}\text{Fe}$	44.5 d
0.00	0.00	(n,n)	$^{58}\text{Fe}$	stable
1.42	-1.40	(n, $\alpha$ )	$^{55}\text{Cr}$	3.50 m
5.56	-5.46	(n,p)	$^{58}\text{Mn}$	65.2 s / 3.0 s
7.78	-7.65	(n,n+ $\alpha$ )	$^{54}\text{Cr}$	stable
9.36	-9.20	(n,2 $\alpha$ )	$^{51}\text{Ti}$	5.76 m
9.90	-9.73	(n,d)	$^{57}\text{Mn}$	85.4 s

**Table 3.2:** Neutron induced reactions on the stable isotopes of iron. The data is taken from [Q-value Calculator, 2009] and the half-lives from [Nudat 2.4, 2009].

The aim of this work is to measure the cross section of  $^{54}\text{Fe}(\text{n},\gamma)^{55}\text{Fe}$  for thermal neutron energies with the use of reactor (thermalized) neutrons and with cold neutrons. Figure 3.4 shows the relevant energy region, including the existing experimental data points for thermal neutrons from [Brooksbank *et al.*, 1955] and [Pomerance, 1952] (see also table 3.3).



**Figure 3.4:** The excitation function of the  $^{54}\text{Fe}(n,\gamma)$ -reaction, taken from [Chadwick *et al.*, 2006]. The scales are both logarithmic.

	$E_{n,th}$ [eV]	$\sigma_{^{54}\text{Fe}(n,\gamma)}$ [barn]	$\pm$ uncertainty [%]
Brooksbank et al, 1955:	0.0253	2.9	15.0
Pomerance, 1952:	0.0253	(2.17)	8.0
	0.0253	2.25	8.0

**Table 3.3:** The neutron capture cross section values of  $^{54}\text{Fe}$ , published by [Brooksbank *et al.*, 1955] and [Pomerance, 1952] for thermal energies. The value of [Pomerance, 1952] was measured relative to gold, whose previous thermal neutron capture cross section  $\sigma_{^{197}\text{Au}(n,\gamma)}$  of  $95 \text{ barn} \pm 8 \%$  (for  $v_n = 2200 \text{ m/s}$ ) changed to  $(98.65 \pm 0.90) \text{ barn}$  (measured by [Mughabghab *et al.*, 1981]). The corrected value of the neutron cross-section is 2.25 barn.

### 3.2.2 Proton capture $^{54}\text{Fe}(p,\gamma)^{55}\text{Co}$

Several  $^{55}\text{Fe}/\text{Fe}$ -AMS reference materials were produced at VERA by irradiating Fe-samples with protons. When a  $^{54}\text{Fe}$ -atom captures a proton via the  $(p,\gamma)$ -reaction,  $^{55}\text{Co}$  is produced and decays with a half-life of  $(17.53 \pm 0.03) \text{ h}$  [Junde, 2008] to  $^{55}\text{Fe}$ .  $^{55}\text{Co}$ -activity measurements of the irradiated samples provide then the number of produced  $^{55}\text{Co}$ -atoms, which are assumed to equal the number of  $^{55}\text{Fe}$ -atoms after about 10  $^{55}\text{Co}$ -half-lives (see figure 3.5 for the decay scheme of  $^{55}\text{Co}$ ). By this way, the isotopic ratio of  $^{55}\text{Fe}/\text{Fe}$  of p-irradiated samples was determined and these Fe-samples could be used as reference material for AMS - measurements.

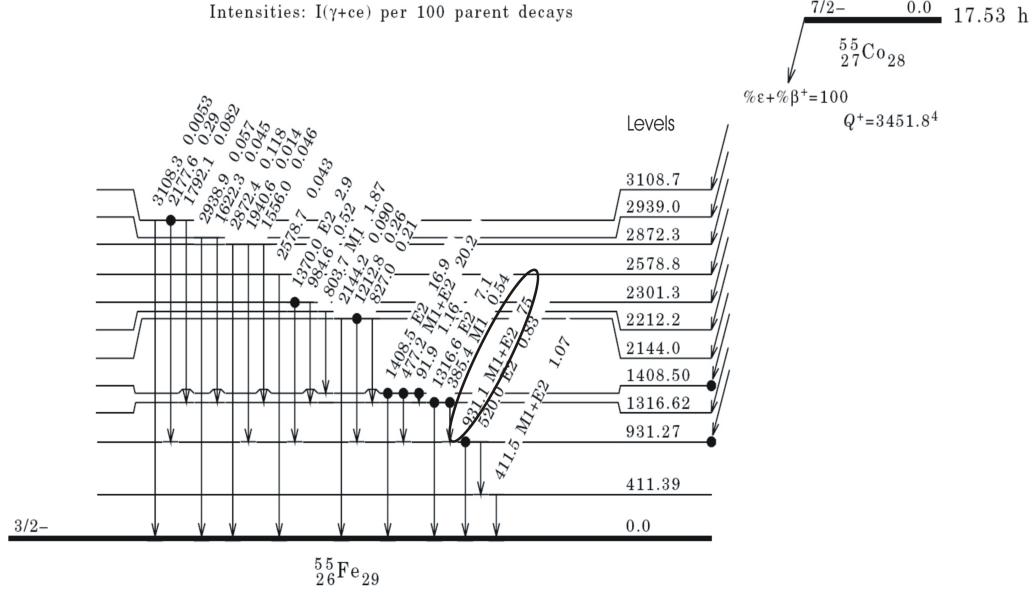


**Figure 3.5:** Decay scheme of  $^{55}\text{Co}$  taken from [Junde, 2008]

Prior to the first proton irradiation, it was helpful to know the proton capture cross section for  $^{54}\text{Fe}(p,\gamma)$  in order to estimate the expected number of produced  $^{55}\text{Co}$ -atoms. Table 3.4 shows those cross section values, measured by [Shakun *et al.*, 1986–87] and [Boukharouba *et al.*, 1992]. However, those very discrepant results allowed only very rough estimations of the production yield of  $^{55}\text{Co}$ .

	$E_p$ [MeV]	$\sigma_{^{54}\text{Fe}(p,\gamma)}$ [mbarn]	$\pm$ [mbarn]
Boukharouba et al., 1992:	3.03	0.53	0.17
	4.08	1.26	0.32
	5.02	2.1	0.42
	5.84	2.55	0.53
	6.05	2.64	0.56
Shakun et al., 1986-87:	4	0.049	0.01
	6	0.13	0.02
	8	0.15	0.02
	9	0.1	0.02

**Table 3.4:** Cross section values for  $^{54}\text{Fe}(p,\gamma)$ , measured by [Shakun *et al.*, 1986–87] and [Boukharouba *et al.*, 1992] for MeV-protons.

### 3 Experimental background

Table 3.4 shows, that the cross section for the (p, $\gamma$ ) reaction increases strongly with the energy of the incident protons (see also figure 2.4 in section 2.2). Thus, high energy protons will be favourable in order to increase the production yield of  $^{55}\text{Co}$ . With VERA a maximum proton energy of about 5.5 MeV was applied.

The open reaction channels for  $^{54}\text{Fe}(\text{p},*)$ -reactions are shown in table 3.5.

$E_{th}$ [MeV]	Q-value [MeV]	$^{54}\text{Fe}(\text{p},*)$	products	$t_{1/2}$
0.00	5.06	(p, $\gamma$ )	$^{55}\text{Co}$	17.5 h
0.00	0.00	(p,p)	$^{54}\text{Fe}$	stable
3.21	-3.15	(p, $\alpha$ )	$^{51}\text{Mn}$	46.2 m
8.58	-8.42	(p,p+ $\alpha$ )	$^{50}\text{Cr}$	$>1.3 \cdot 10^{18}$ y
9.02	-8.85	(p,2p)	$^{53}\text{Mn}$	$3.74 \cdot 10^6$ y
9.19	-9.03	(p,n)	$^{54}\text{Co}$	193 ms / 1.48 m
$E_{th}$ [MeV]	Q-value [MeV]	$^{56}\text{Fe}(\text{p},*)$	products	$t_{1/2}$
0.00	6.03	(p, $\gamma$ )	$^{57}\text{Co}$	272 d
0.00	0.00	(p,p)	$^{56}\text{Fe}$	stable
1.07	-1.05	(p, $\alpha$ )	$^{53}\text{Mn}$	$3.74 \cdot 10^6$ y
5.44	-5.35	(p,n)	$^{56}\text{Co}$	77.2 d
7.75	-7.61	(p,p+ $\alpha$ )	$^{52}\text{Cr}$	stable
9.13	-8.97	(p,d)	$^{55}\text{Fe}$	2.74 y
$E_{th}$ [MeV]	Q-value [MeV]	$^{57}\text{Fe}(\text{p},*)$	products	$t_{1/2}$
0.00	6.95	(p, $\gamma$ )	$^{58}\text{Co}$	9.04 h / 70.9 d
0.00	0.24	(p, $\alpha$ )	$^{54}\text{Mn}$	312 d
0.00	0.00	(p,p)	$^{57}\text{Fe}$	stable
1.65	-1.62	(p,n)	$^{57}\text{Co}$	272 d
5.52	-5.42	(p,d)	$^{56}\text{Fe}$	stable
7.45	-7.32	(p,p+ $\alpha$ )	$^{53}\text{Cr}$	stable
7.78	-7.65	(p,n+p)	$^{56}\text{Fe}$	stable
8.67	-8.52	(p,2 $\alpha$ )	$^{50}\text{V}$	$1.4 \cdot 10^{17}$ y
8.85	-8.70	(p,n+ $\alpha$ )	$^{53}\text{Mn}$	$3.74 \cdot 10^6$ y
$E_{th}$ [MeV]	Q-value [MeV]	$^{58}\text{Fe}(\text{p},*)$	products	$t_{1/2}$
0.00	7.36	(p, $\gamma$ )	$^{59}\text{Co}$	stable
0.00	0.42	(p, $\alpha$ )	$^{55}\text{Mn}$	stable
0.00	0.00	(p,p)	$^{58}\text{Fe}$	stable
3.14	-3.09	(p,n)	$^{58}\text{Co}$	9.04 h / 70.9 d
7.64	-7.51	(p,2 $\alpha$ )	$^{51}\text{V}$	stable
7.78	-7.65	(p,p+ $\alpha$ )	$^{54}\text{Cr}$	stable
7.96	-7.82	(p,d)	$^{57}\text{Fe}$	stable
9.37	-9.21	(p,t)	$^{56}\text{Fe}$	stable
9.98	-9.81	(p,n+ $\alpha$ )	$^{54}\text{Mn}$	312 d

**Table 3.5:** Proton induced reactions on the stable isotopes of iron. The data is taken from [Q-value Calculator, 2009] and the half-lives from [Nudat 2.4, 2009].

### 3.3 The facility VERA

In section **Outline** 1.2, a brief summary of this thesis was given. As mentioned there, the thesis is divided into two parts: The production of a  $^{55}\text{Fe}$ -AMS reference material by two independent methods and the determination of the thermal neutron capture cross section  $^{54}\text{Fe}(n,\gamma)$  via AMS. Most of the experiments were carried out at the Vienna Environmental Research Accelerator, VERA, and include proton irradiations of Fe-samples and a large number of  $^{55}\text{Fe}$ -AMS measurements.

In general, VERA is dedicated to Accelerator Mass Spectrometry AMS, but finds also applications in methods like PIXE (Proton Induced X-ray Emission), PIGE (Proton Induced Gamma Emission) and RBS (Rutherford Back Scattering).

The main idea of the AMS facility is to separate the isotopes of a sample according to their mass, energy, momentum and charge. Once separated and identified by their atomic number and mass, one can either count the individual isotopes (and their ratios like in AMS) or use them as an ion beam (e.g. for bombarding another sample). The components of VERA and applications will be described in the following section.

#### 3.3.1 The principle of accelerator mass spectrometry (AMS)

Accelerator mass spectrometry is a technique to separate ions with different masses. To realise the selection of a specific mass over charge  $M/q$  with a certain energy over charge  $E/q$  of a sample, one needs a combination of at least a magnetic and an electrostatic deflection and an electrostatic acceleration.

##### Electrostatic acceleration

Applying a certain voltage  $U$ , a single charged particle is accelerated in an electrical field to a certain energy  $E$ . A doubly negatively charged particle will be accelerated to twice the energy, but the ratio of energy  $E$  to charge  $q$  is constant and defined by the voltage  $U$ :

$$\frac{E}{q} = U. \quad (3.1)$$

The homogeneous electrostatic field in the tandem accelerator at VERA is realised by the division of the whole distance of acceleration into equally spaced electrostatic acceleration sections of annular electrodes, where the voltage applied to each following annular electrode is constantly increased by resistors.

##### Magnetic deflection

An uniform magnetic field  $B$ , normal to the plane of motion of the ion, leads to the selection of  $EM/q^2$  along the radius of curvature  $\rho_m$ :

$$\frac{ME}{q^2} = \frac{1}{2} (B\rho_m)^2, \quad (3.2)$$

where  $M$  is the mass of the selected ion of energy  $E$  on radius  $\rho_m$ .

### Electrostatic deflection

The uniform electrostatic field  $\epsilon$  of the electrostatic analyzer deflects the ions according to their energy over charge-ratio  $E/q$  along the radius  $\rho_e$  (see equation 3.3). It represents an additional selection of the wanted energy.

$$\frac{E}{q} = \frac{1}{2} \epsilon \rho_e \quad (3.3)$$

The electrostatic deflection is realised, e.g. by two concentric spherical conducting plates. The potential difference  $\Delta U$  between them leads to an electric field  $\epsilon$  which is indirectly proportional to their distance  $d$ :

$$\epsilon = \frac{U}{d}. \quad (3.4)$$

Selecting a certain energy  $E/q$  of the ion, one has to set the value of the applied voltage  $U$  as parameter according to equation 3.5 (by means of equation 3.3 and 3.4).

$$U = 2 \frac{E}{q} \frac{d}{\rho_e} \quad (3.5)$$

### Contaminations

Still, there is a variety of cases where the filters listed above are not sufficient to avoid contaminations from:

- Atomic isobars (different elements having the same mass number)
- Molecular isobars (Molecules with a mass, which equals the one of the isotope to be selected)
- Ions with values of  $M/q$  and  $E/q$ , which equal the ones of the radionuclide to be selected
- Ions with incorrect mass, energy or charge (e.g. adjacent mass isotopes), which mimic the path of ions of interest to the detector, because energy- or charge-changing collisions with the system components or residual gas occur. [Tuniz *et al.*, 1998]

The contributions coming from molecules are problematic in mass spectrometry (MS, with particle energies typically in the range of keV) but are solved in AMS (with particle energies typically in the order of MeV) as the molecules are dissociated

at the terminal of the tandem accelerator. Atomic isobars can be resolved, e.g. by an ionization chamber or by a gas filled analyzing magnet system. A TOF (Time-of-flight) system can be used as additional isotopic separation. In general, the sensitivity of AMS reaches abundance ratios of better than  $10^{-15}$ , depending on a variety of factors.

### 3.3.2 The main components

Figure 3.6 shows a schematic layout of the VERA facility.

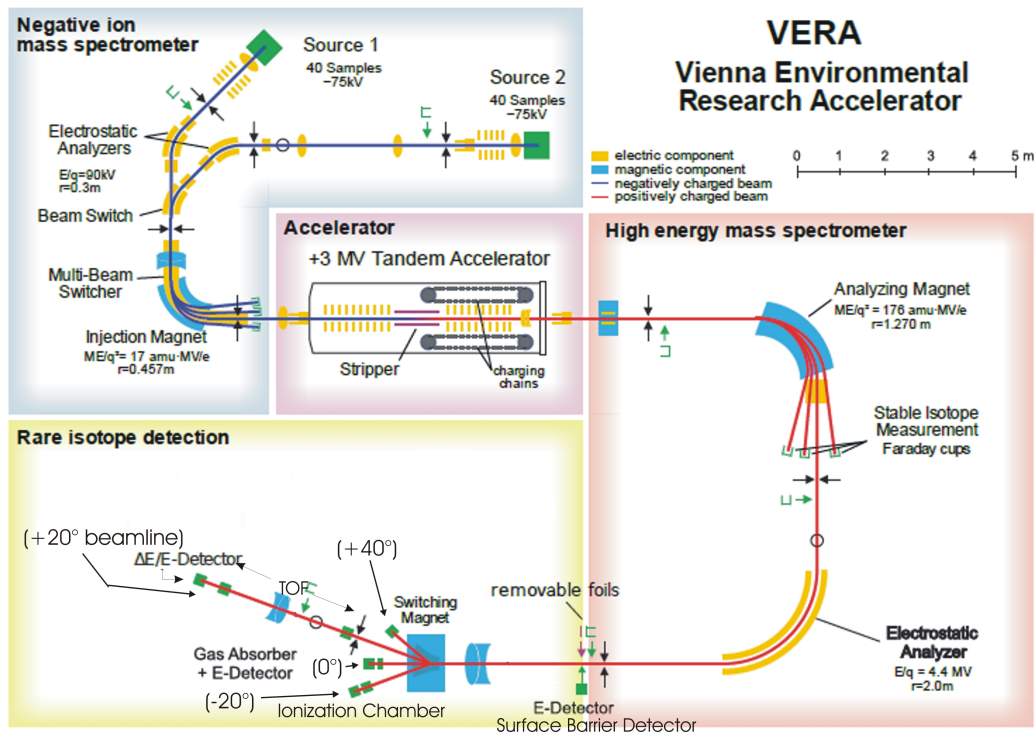


**Figure 3.6:** Schematical view of the Vienna Environmental Research Accelerator, based on a figure from Vockenhuber and Michlmayr.

#### Samples analyzed by AMS

The typical amount of sample mass required for AMS lies between  $\mu g$  and some  $mg$ . Pressed into sample holders (=cathodes), they are put into a wheel. At VERA, 40 cathodes can be placed in one wheel.

#### Ion source

Using a tandem accelerator, one has to inject negative ions, which are extracted from the sample by means of a caesium sputter source. A caesium reservoir is heated, its

vapour is guided through a tube to a very hot metal surface, where it is mostly ionized to  $Cs^+$  ions (due to its smaller ionization potential compared to the work function of tantal). As a ground potential is applied on the metal surface and a negative potential on the cathode wheel, the  $Cs^+$  ions are accelerated towards the sample. The geometry is chosen such that a focused Cs sputter beam is generated. In addition, caesium condenses on the top of the cooled sample and favours the formation of negative sample ions, which then will be accelerated by the extraction electrode.

An important quantity is the probability of producing negative ions. It depends mainly on the electron affinity of the element. Elements with an electron affinity  $< 0$  will not form negative ions. This can be an advantage if those elements are disturbing stable isobars and thus can not interfere the measurement of the rare isotope (of the same mass) (like the stable  $^{55}Mn$  during the measurement of  $^{55}Fe$ ). But it can be a disadvantage if it concerns the rare isotope which has to be measured. Then a molecule of the element has to be chosen to increase the production yield of negative ions.

#### Low energy injection system

The low energy injection system consists of **the preaccelerator, the 45° electrostatic analyzer (ESA), and the 90° injection magnet.**

Right after the preaccelerator, the negatively charged sample atoms have an energy of about 75 keV and pass then a 45° electrostatic analyzer (or 90° via two times 45° ESAs for samples in the second ion source, see figure 3.6).

The following 90° magnetic analyzer includes a **Multi Beam Switcher** called **MBS**. It allows to alternately inject isotopes of different masses without a change of the magnetic field (which would result in a very slow and badly reproducible process). If, e.g. the mass of the rare isotope is selected to fly through the magnetic analyzer along the radius  $\rho_m$ , every ion with the same constant magnetic rigidity  $ME/q^2$  (see equation 3.2) passes. As the energy of the ions is already constant (by means of the electrostatic elements) the selection occurs according to their masses. The bigger the mass the bigger the radius of the deflected ion. If one wishes to let pass a lighter ion one has to increase its energy so that it receives the same magnetic rigidity  $ME/q^2$  (see equation 3.2). In fast isotope switching, this is done by applying a certain voltage between 0 and +13 keV to the insulated vacuum chamber of the analyzing magnet so that the ions are accelerated just before entering the magnet chamber to get the same value of  $ME/q^2$  as the rare isotope. Just before leaving the magnet chamber, they are slowed down again and maintain their original energy.

At VERA it is possible to switch between four different MBS voltages, which are used to inject stable isotopes into Faraday Cups placed on the low energy and on the high energy side of the tandem accelerator to measure their currents, and to count the rare isotopes with a particle detector.

### Tandem accelerator

The end points of the tandem accelerator have earth potential, in the middle of the tandem accelerator lies the positive high-voltage terminal (up to +3 MV at VERA) and accelerates the negatively charged ions to energies of about 3 MeV. Through collisions with the gas stripper (placed directly in the terminal) the negatively charged ions convert to neutral ions and multiply - charged positive ions. Due to the loss of their electrons, molecules are dissociated. Converted in charge, the ions are accelerated a second time by the high difference of potential between the +3 MV terminal and the earthed end of the tandem accelerator. The pelletron system and the stabilising elements provide the voltage of the terminal.

The energy of the positive ion (with charge  $q$ ) after the tandem accelerator  $E_+$  is given in equation 3.6:

$$E_+ = [(U_i + U_T) \cdot \frac{M_+}{M_-} + qU_T] e, \quad (3.6)$$

where  $U_i \cdot e$  is the energy of the incident negative ion given in electron Volts,  $U_T$  is the terminal voltage and  $M_+/M_-$  is the ratio in mass of the outgoing positive ion and of the incident negative ion, respectively and has to be applied for molecules as their masses change while breaking up in the stripper gas.

### High energy side

The high energy side consists of a 90° magnetic analyzer (which sorts out different charge states and molecular fragments), a 90° electrostatic analyzer and an additional switching magnet leading to four different beamlines (the -20° beamline used for AMS and PIXE, the 0° energy beamline, the +20° TOF (Time Of Flight) beamline and the +40° beamline shown in figure 3.6) used all for AMS measurements of different radionuclides.

### Focusing elements

A **magnetic quadrupoles** consist of two north and two south poles. One quadrupole has a focusing effect in one axis, but a defocusing effect in the other axis. To achieve a focusing effect in both axis, two quadrupoles have to be placed in sequence, tilted by 90 degrees. An **electric quadrupole** works in an analogue way.

### Beam diagnostic elements

A couple of **slits** are placed along the beam tubes. Changing their aperture, the position and the profile of the ion beam can be specified. During the tuning procedure, the slits can be used to define the beam trajectory of the ions.

The **beam profile monitor** consists of a wire, which is moving across the beamline. By this way, a current is measured, when the ion beam crosses the wire and the profile of the beam is monitored.

### 3.3.3 Isotope ratios - Ion detection systems

The result of an AMS-measurement are ratios of rare to stable isotopes.

For this purpose, the **stable isotopes** are injected by means of the Multi Beam Switcher MBS (see section above) into Faraday Cups, two of them are placed at the low energy side and three of them on the high energy side. A **Faraday Cup FC** is a cup where the charge of the ions is collected and measured as current (not energy dispersive) and is used for isotope beams of high intensity (in the range of pA -  $\mu$ A). To prevent the escape of secondary electrons from the Cup an insulated negative electrode is mounted at the entering position of the cup.

The identification of rare isotopes can still be interfered by other ions (like isotopes and isobars). Looking at the properties of the ions (energy  $E$ , mass  $M$ , velocity  $v$ , atomic number  $Z$  and charge  $q$ ) it becomes obvious to use energy-, mass- or/and  $Z$  dispersive detectors to identify the rare radionuclides.

If the ion is totally stopped inside the detector material one measures its total energy, e.g. in the case of the **surface barrier detector**.

If a detector is used, whose thickness is smaller than the ion range, one measures  $\Delta E$ , a fraction of the total energy (described by the Bethe - Bloch - equation, 3.7), which is proportional to the square of the atomic number  $Z$  (and thus selective to isobars) (e.g. **ionization chamber**). The residual energy can then be measured by another detector.

The separation of different masses (at the same value of energy) can be done by a distinction of velocity and is thus selective to isotopes (e.g. **time-of-flight detector**).

Such types of detection systems were used for the AMS - measurement of  $^{55}\text{Fe}$  and are discussed in detail in the following section.

#### Surface barrier detector

The so-called SB-detector, a surface barrier detector, is positioned after the high energy Electrostatic Analyzer ESA (see figure 3.6). The incident ions ionize the atoms of the silicon detector and hence produce electron - hole pairs, which are separated by an imposed electrical field gradient. The anode collects the drifting electrons, the cathode collects the formed holes and both electrodes contribute to the produced time integrated current pulse (which is proportional to the energy of the ions). Figure 3.7 shows a typical spectrum of  $^{55}\text{Fe}$  acquired by the surface barrier detector.  $^{55}\text{Fe}$  is detected between channel number 750 and 900. Below channel number 750, the detected background is visible. At very low energies, a sharp peak

is seen, which comes from scattering effects.

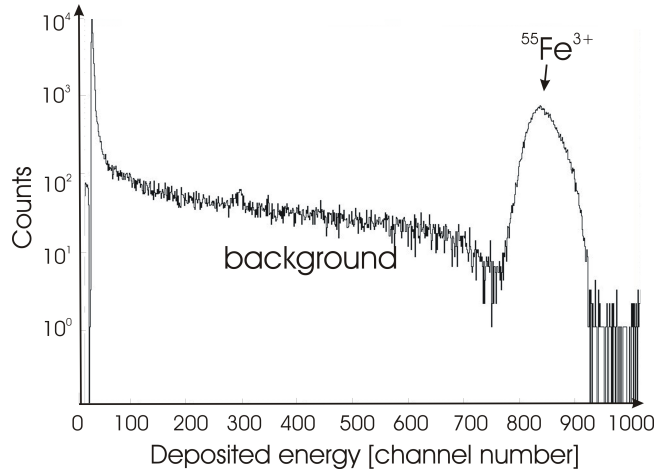


**Figure 3.7:** A typical spectrum of  $^{55}\text{Fe}$ , measured by the surface barrier detector

### Ionization chamber

The ionization chamber was built by [Forstner *et al.*, 2008] at VERA and is based on a design made by ETH Zürich [Döbeli *et al.*, 2004]. For  $^{55}\text{Fe}$ -AMS measurements it was placed at the  $-20^\circ$ -(PIXE-) beamline (see VERA scheme in figure 3.6). It is filled with isobutane gas. The anode of the detector is divided into two parts, one at the front and one at the back section of the detector. Due to their bigger stopping power, ions with higher atomic number  $Z$  will lose more energy in the first section and will stop earlier in the detector than ions with lower  $Z$ . The signal processing of both anodes is individually performed and is described, e.g. in [Michlmayr, 2007], [Martschini, 2008].

$$-\frac{dE}{dx} \propto \frac{Z_i^2}{v_i^2} Z \cdot \ln\left(\frac{2m_e v_i^2}{I}\right) \quad (3.7)$$

Equation 3.7 describes the rate of energy loss of an incident charged particle (with atomic number  $Z_i$ , velocity  $v_i$ ) in matter (of atomic number  $Z$ ) due to ionization,  $m_e$  is the mass of the electron and  $I$  the ionization potential.

Figure 3.8 shows a typical spectrum of  $^{55}\text{Fe}$ -counts, which were acquired by the ionization chamber. The energy, which is deposited in anode 1, the first section of the ionization chamber, is plotted on the horizontal axis; a greater energy loss corresponds to higher  $Z$  ions or to ions of higher energy. The energy, deposited in anode 2, the second section of the ionization chamber, is plotted on the vertical axis. The intensity bar on the right side shows the colour code for the number of detected counts. The total energy loss of the ion, which is represented by the sum of anode

1 and anode 2, is constant because the ion is stopped inside the ionization chamber. Variations of the ions energy loss in the single anodes lead to the slope of the peak, seen in figure 3.8.

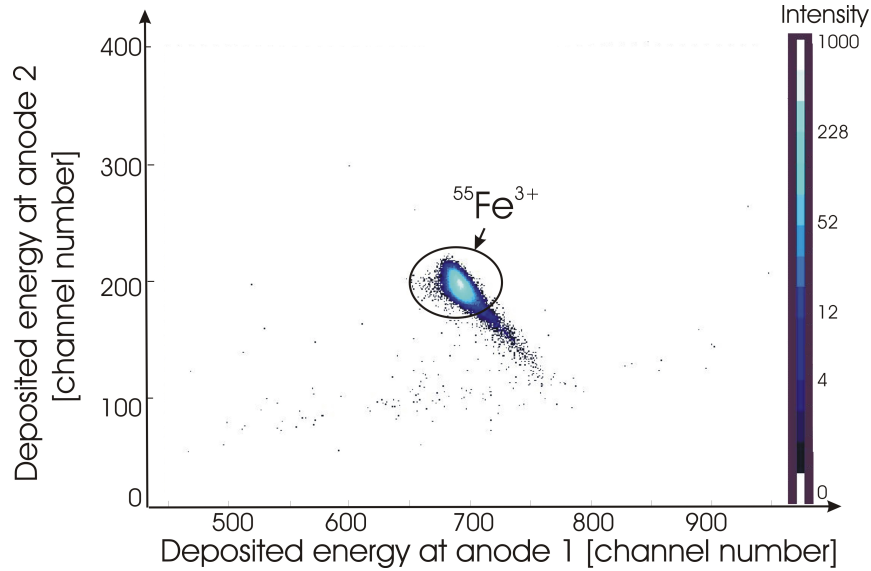


**Figure 3.8:** A typical spectrum of  $^{55}\text{Fe}$ , measured by the ionization chamber.

#### TOF detector

The Time-Of-Flight (TOF) detector at the  $+20^\circ$ -beamline consists of following components:

- a micro-channel plate detector (for the start signal)
- a second micro-channel plate detector at a horizontal distance of 2.8 m (for the stop signal)
- an ionization chamber (Bragg type) (for the energy measurement).

Flying through a thin carbon foil, the highly energetic ion is knocking out electrons, which are then accelerated to a grid and further to the micro channel plate. The latter multiplies the number of produced electrons to generate the start signal. The generation of the stop signal follows the same principle. The energy of the ion is measured with the Bragg detector. The time, which passes between the start and stop signal, is converted into an amplitude signal (by a TAC (Time-to-Amplitude converter)) and rises with the mass of the isotope for the same energy (or  $E \cdot M$  as defined by the preceding components, the magnetic and the electrostatic deflectors). This becomes clear in the following short calculation:

$$\Delta t = ToF = \frac{s}{v} = s \cdot \frac{1}{\sqrt{2E/m}}$$

Converting the units of [E]=J, [m]=kg into the commonly used [E]=MeV and [m]=amu, one gets equation 3.8 (given in nanoseconds, ns):

$$ToF(ns) \approx 2.8(m) \cdot 72 \sqrt{\frac{m(amu)}{E(MeV)}} \quad (3.8)$$

Using equation 3.8, one gets the time, which a  $^{55}\text{Fe}$ - ion of 12 MeV energy needs for passing a distance of 2.8 m:

$$TOF_{55\text{Fe}} \approx 431.6 \text{ ns}$$

At the position of the TOF-detector, all ions have the same  $M_x \cdot E_x/q^2$  value, because they all passed the selective electrostatic and magnetic analyzers. Assuming that during the detection of  $^{55}\text{Fe}$ -ions a specific amount of stable iron isotopes also reaches the detector (as  $M_x \cdot E_x/q^2 = \text{const}$ ) one gets for the time of flight of the stable isotopes  $^{54}\text{Fe}$  and  $^{56}\text{Fe}$ :

$$\text{using } M_{55}E_{55} = M_{56}E_{56} \rightarrow E_{56} = \frac{M_{55}}{M_{56}}E_{55}$$

$$TOF_{56\text{Fe}} = ToF_{55\text{Fe}} \cdot \frac{M_{56}}{M_{55}} \approx 439.4 \text{ ns} \quad (\text{and } E_{56} \approx 11.8 \text{ MeV})$$

$$TOF_{54\text{Fe}} = ToF_{55\text{Fe}} \cdot \frac{M_{54}}{M_{55}} \approx 423.8 \text{ ns} \quad (\text{and } E_{54} \approx 12.2 \text{ MeV})$$

The time difference between the rare isotope and the stable ones is of about 8 ns. Depending on the electrical adjustments, the time resolution of the ToF- detector is about (0.8 - 1.2) ns (FWHM).

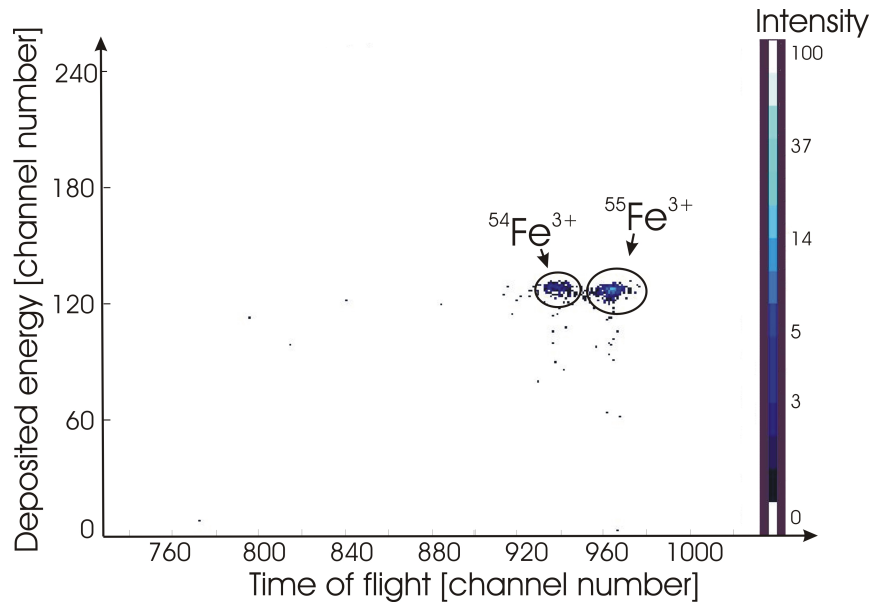


**Figure 3.9:** A typical spectrum of  $^{55}\text{Fe}$ , measured by the TOF spectrum

Figure 3.9 shows a typical spectrum of  $^{55}\text{Fe}$ , acquired by the TOF system at the  $+20^\circ$  beamline. On the horizontal axis, the Time-Of-Flight is plotted, which increases with increasing mass of the isotope. The residual energy of the ions, measured by an ionization chamber, is plotted on the vertical axis. The vertical axis is now selective to the different possible charge states, because an ion with more energy will have an higher charge state because  $E/q = \text{const.}$

More details concerning the ToF- detector (including the electronics of the ToF system) can be found in the diploma thesis of [Brandl, 1998], [Vockenhuber, 1999], [Valenta, 2001] and in [Vockenhuber *et al.*, 2003], [Steier *et al.*, 2005] and [Steier *et al.*, 2009].

# 4 Mathematical background

This chapter treats the mathematical background, needed in the course of the thesis:

- The production of radionuclides by activation (divided in the first, more theoretical section and the second, more applied one), for activity measurements with a high purity germanium diode.
- Several correction factors, which had to be considered for the activity measurement, are discussed in the third section.
- In the last section, basic equations from statistics are given, which are especially important for the evaluation of the  $^{55}\text{Fe}$ -AMS measurements.

## 4.1 Activation - Production of radionuclides

During the irradiation of a sample, two processes occur at the same time (valid for radionuclides):

1) The first one is the production of radionuclides  $N_x(t)$  with the production rate  $q(t)$ , (compare also 2.13, with  $\sigma_{ab} = \sigma(E)$  and  $N_A = N_0$ ):

$$q(t) = \varphi(t)\sigma N_0$$

$\varphi(t)$  ... number of incident particles (= projectiles) per area and time, flux [ $\text{cm}^{-2} \text{s}^{-1}$ ]  
 $\sigma$  ... cross section, probability for producing the radionuclide [ $\text{cm}^2$ ]  
 $N_0$  ... number of mother nuclei

2) The second one is the reduction of the produced radionuclides  $N_x(t)$  at time  $t$  because of their radioactive decay (with the decay constant  $\lambda$  [1/s]), described by

$$A = \lambda N_x(t)$$

$A$  ... Activity, number of decaying radionuclides per time

Combining both relations one gets the change of the number of daughter nuclides  $\frac{dN_x}{dt}$  at time  $t$ , described by equation 4.1:

$$\frac{dN_x(t)}{dt} = q(t) - \lambda N_x(t) \quad (4.1)$$

I) The solution of this differential equation leads to the number of produced daughter nuclei  $N_x(t)$  at time  $t$ :

$$\rightarrow N_x(t) = e^{-\lambda t} \cdot [N_x(0) + \int_0^t e^{\lambda\tau} q(\tau) d\tau] \quad (4.2)$$

II) Applying equation 4.2 for an irradiation time  $T_{irr}$ , assuming a constant flux  $\varphi = const$  of incident particles and  $N_t = const$ ,  $N_x(0) = 0$  one can write:

$$N_x(t_{irrE}) = \varphi\sigma N_0 \cdot e^{-\lambda t} \int_{t_{irrA}}^{t_{irrE}} e^{\lambda\tau} d\tau = \varphi\sigma N_0 \cdot \frac{1}{\lambda} (1 - e^{-\lambda T_{irr}})$$

Thus the activity (decays per second) at the end of the irradiation  $t_{irrE}$  (4.3) is (with  $A = N\lambda$ ):

$$A(t_{irrE}) = \varphi\sigma N_0 \cdot (1 - e^{-\lambda T_{irr}}) \quad (4.3)$$

For the total number of decays during the irradiation time, one has to integrate over the irradiation time:

$$\int_{t_{irrA}}^{t_{irrE}} A(\tau) d\tau = \underbrace{\varphi\sigma N_0 \cdot T_{irr}}_{N_{x,total}} - \underbrace{\varphi\sigma N_0 \cdot \frac{(1 - e^{-\lambda T_{irr}})}{\lambda}}_{N_x(t_{irrE})} \quad (4.4)$$

where the first term represents the total number of produced radionuclides  $N_{x,total}$ , and the second one represents the number of still existent radionuclides at the end of the irradiation interval.

If the activity of a sample is known, one can derive from 4.4 and 4.3 the total number of produced radionuclides  $N_{x,total}$ :

$$N_{x,total} = \varphi\sigma N_0 \cdot T_{irr} \stackrel{(4.3)}{=} A(t_{irrE}) \cdot \frac{T_{irr}}{(1 - e^{-\lambda T_{irr}})} \quad (4.5)$$

III) If the flux of incident particles  $\varphi$  is not constant as assumed above, one can divide the irradiation time  $T_{irr}$  in short time intervals  $T_{irr,k}$  of constant flux and sum it up:

$$\frac{T_{irr}}{(1 - e^{-\lambda T_{irr}})} \rightarrow \frac{1}{\sum_k \frac{\varphi_k}{\varphi} \frac{(1 - e^{-\lambda T_{irr,k}})}{T_{irr,k}} \cdot e^{-\lambda(t_{irr,E} - t_{irr,k})}} \quad (4.6)$$

$T_{irr,k}$	...	time intervals of constant flux $\varphi_k$
$t_{irr,k}$	...	end time of the time intervall $T_{irr,k}$
$t_{irr,E}$	...	end time of the whole irradiation
$e^{-\lambda(t_{irr,E} - t_{irr,k})}$	...	accounts for the decay of the produced radionuclides of time interval $T_{irr,k}$

with  $\sum_k T_{irr,k} = T_{irr}$  and  $\sum_k \varphi_k = \varphi$ .

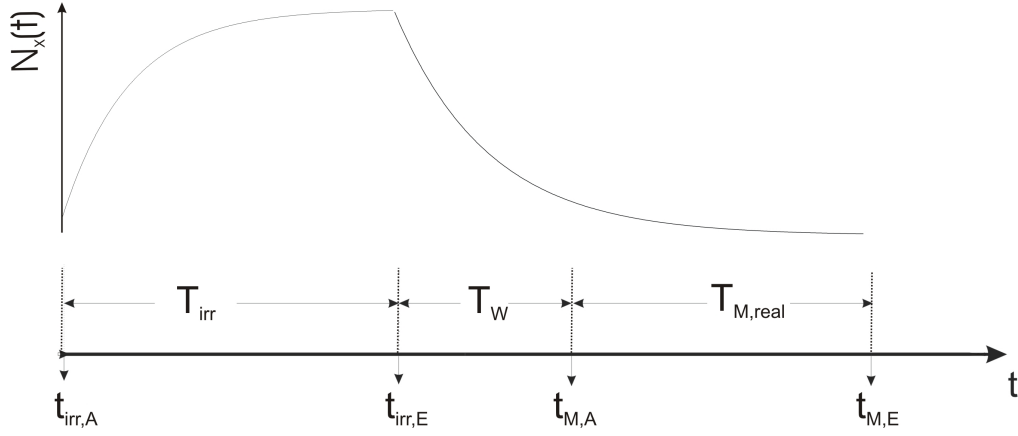


**Figure 4.1:** Scheme of the experimental time procedure. During the irradiation time  $T_{irr}$  the sample is activated and the number of produced radionuclides  $N_x(t)$  increases and approaches a constant value given by the balance of production and decay. In the waiting time  $T_W$  the produced radionuclides decay exponentially and are then measured during the time  $T_{M,real}$ .

## 4.2 Determination of produced $^{55}\text{Fe}$

### 4.2.1 The number of produced radioactive atoms

The total number of radionuclides  $N_{x,total}$ , which were produced during the irradiation time  $T_{irr}$ , is (for the derivation see equation 4.5):

$$N_{x,total} = \frac{A(t_{irr,E})}{\lambda} \cdot \frac{\lambda T_{irr}}{1 - e^{-\lambda T_{irr}}} \quad (4.7)$$

- $\lambda$  ... decay constant ( $= \ln(2)/t_{1/2}$ ) [1/s]
- $t_{irr,E}$  ... the end time of the irradiation
- $T_{irr}$  ... the duration of the irradiation
- $A(t_{irr,E})$  ... activity at time  $t_{irr,E}$

### 4.2.2 The activity of an irradiated sample

The number of decays per second (= activity  $A$ ) at time  $t_{M,A}$ , the start time of the data acquisition, equals the corresponding true (= corrected) count rate per second  $n_{true}(t_{M,A})$  of a certain  $\gamma$ -ray, divided by its emission probability  $p_\gamma$  [%] and by the detector efficiency  $\epsilon_\gamma$ :

$$A(t_{M,A}) = \frac{n_{true}(t_{M,A})}{\epsilon_\gamma p_\gamma}. \quad (4.8)$$

### 4.2.3 Correction factors for the true count rate per second

A  $\gamma$ -ray deposits its full energy in a detector (provided that it is stopped inside the detector completely). In the  $\gamma$ -ray spectrum (see figure 2.3) the  $\gamma$ -ray is then (ideally) represented by the full energy peak. The number of emitted  $\gamma$ -rays (with energy  $E_\gamma$ ) is represented by the content of the peak and is called net peak area  $N$ , if the background is subtracted.

The following corrections have to be taken into account to derive the true (= corrected) count rate per second,  $n_{true}$ , from the net peak area  $N$ .

#### Deadtime correction

Any detector has a certain deadtime  $\tau$ , in which emitted  $\gamma$ -rays or particles can not be measured because the electronic is busy to process data. The total dead time is then  $\tau n_{all}$ , because after any signal which is processed, the detector has a specific deadtime  $\tau$ , which is fixed by the electronics.

The number of counts, which were not measured during the total deadtime (=  $n_{true} \cdot \tau n_{all}$ ), is just the difference between the true count rate  $n_{true}$  and the measured one,  $n$ :

$$n_{true} - n = n_{true} \cdot \tau \cdot n_{all}$$

$$n_{true} = \frac{n}{1 - n_{all}\tau} = \frac{N/T_{M_{real}}}{1 - N_{all}/T_{M_{real}}\tau} = \frac{N}{T_{M_{real}} - N_{all}\tau}$$

$n_{true}$	...	true count rate per second
$n$	...	measured count rate per second
$\tau$	...	deadtime of the detector
$N$	...	net peak area content of a full energy peak at the energy $E_\gamma$
$N_{all}$	...	total number of acquired counts
$n_{all}$	...	total count rate per second of acquired counts
$t_{MA}$	...	start point of measurement
$T_{M_{real}}$	...	real time = the passed clock time since $t_{MA}$ [s]

With  $T_{M_{real}} - N_{all}\tau$  being the live time  $T_{M_{live}}$ , one can write for the true count rate per second  $n_{true}$ :

$$n_{true} = \frac{N}{T_{M_{live}}} \quad (4.9)$$

$T_{M_{live}}$	...	"On-line" time of the detector [s]
		( $T_{M_{live}}$ is smaller than $T_{M_{real}}$ and the total deadtime increases with the count rate)

### Decay Correction to the start time of the measurement

During the time  $T_{M_{real}}$  of the acquisition, the number of radionuclides decreases exponentially with  $N_x(t) = N(0) e^{-\lambda t}$ . Using the correction factor  $C_{decay_M}$  (see equation 4.10) one gets the count rate per second at the start point of the measurement [Debertin & Helmer, 1988]:

$$n_{true}(t_{M_A}) = n_{true} \cdot C_{decay_M} = n_{true} \cdot \frac{\lambda T_{M_{real}}}{1 - e^{-\lambda T_{M_{real}}}} \quad (4.10)$$

$T_{real}$  ... real time of the detector [s]  
 $\lambda$  ... decay constant ( $= \ln(2)/t_{1/2}$ ) [1/s]

#### 4.2.4 The calculated number of $^{55}\text{Fe}$ -atoms

The summary of the calculation steps above (4.7 - 4.10) gives the direct formula used for the activity  $A(t_{irr_E})$  at the end of the irradiation (see equation 4.11) and furthermore the total number of produced radionuclides (see equation 4.12):

$$A(t_{irr_E}) = \frac{N}{T_{M_{live}}} \cdot \frac{\lambda T_{M_{real}}}{1 - e^{-\lambda T_{M_{real}}}} \cdot \frac{1}{\epsilon_\gamma p_\gamma} \cdot e^{\lambda T_W} \quad (4.11)$$

$T_W$  ... the waiting time between the end of the irradiation  
 and the start of the measurement with the germanium detector

$$N_{x,total} = \frac{N}{T_{M_{live}}} \cdot \frac{\lambda T_{M_{real}}}{1 - e^{-\lambda T_{M_{real}}}} \cdot \frac{1}{\epsilon_\gamma p_\gamma} \cdot e^{\lambda T_W} \cdot \frac{\lambda T_{irr}}{(1 - e^{-\lambda T_{irr}})} \cdot \frac{1}{\lambda} \quad (4.12)$$

The only parameters, which contribute to the uncertainty of  $N_{x,total}$  are:  $N$ ,  $\epsilon_\gamma$  and  $p_\gamma$ , the others can be neglected. For most applications, the uncertainty of 4.12  $s(N_{x,total})$  is thus:

$$s_{N_{x,total}} = N_{x,total} \cdot \sqrt{\left(\frac{s_N}{N}\right)^2 + \left(\frac{s_{\epsilon_\gamma}}{\epsilon_\gamma}\right)^2 + \left(\frac{s_{p_\gamma}}{p_\gamma}\right)^2} \quad (4.13)$$

The uncertainty  $s_N$  is independent for each singular event and the uncertainties  $p_\gamma$  and  $\epsilon_\gamma$  are systematic uncertainties, which stay the same for each singular event.

#### 4.2.5 The calculated isotope ratio $^{55}\text{Fe}/\text{Fe}$

The isotopic ratio  $\frac{N_{x,total}}{N_{stable}}$  is calculated by the number of produced radionuclides  $^{55}\text{Fe}$  (see equation 4.12) divided by the number of stable nuclides (see equation 4.14).

$$N_{stable} = m \cdot \frac{a N_A}{m_{mol}} \quad (4.14)$$

$m$	...	mass of the sample [g]
$a$	...	abundance of a specific isotope [atomic percent]
$N_A$	...	Avogadro number
$m_{mol}$	...	molar mass of the sample [g/mol]

One mol consists of  $N_A = 6.02214 \cdot 10^{23}$  atoms (or molecules, dependent on the chemical composition) and weights  $m_{mol}$  gramms. 1 Mol of natural iron weights 55.845 g and consists of  $N_A$  Fe-atoms.

### 4.3 Correction factors for the germanium diode

#### 4.3.1 Coincidence summing correction

Coincidence summing occurs for radionuclides, which emit more than one  $\gamma$ -ray while decaying and thus, has to be taken into account in case of activity-measurements of  $^{55}\text{Co}$ . In the appendix, in section A.1.1, the calculation of coincidence summing is discussed in detail. Table 4.1 gives the calculated coincidence-summing correction factors for the 477, 931 and 1408 keV  $\gamma$ -rays of  $^{55}\text{Co}$  for the detector geometry (pos 4) used in this work.

isotope	$E_\gamma$ [keV]	$C_{coinc}$
$^{55}\text{Co}$	477.2	1.0293
$^{55}\text{Co}$	931.1	1.0095
$^{55}\text{Co}$	1408	0.9703

**Table 4.1:** Coincidence correction factors for the 477, 931 and 1408 keV  $\gamma$ -rays of the  $^{55}\text{Co}$  decay.

#### 4.3.2 Self - attenuation

The mass attenuation correction factors for  $^{55}\text{Co}$  (see equation 2.10 in section 2.1.2) are listed in table 4.2. Corrections are between 0.4 and 0.7 % for a 0.2 mm thick Fe-foil.

isotope	$E_\gamma$ [keV]	$C_{\text{Mass Attenuation}}$
$^{55}\text{Co}$	477.2	1.00679
$^{55}\text{Co}$	931.1	1.00490
$^{55}\text{Co}$	1408	1.00397

**Table 4.2:** Mass attenuation correction factors for a 477, 931 and 1408 keV  $\gamma$ -ray through 200 $\mu\text{m}$  thick iron foil.

## **Part I**

# **Part I: The production of a $^{55}\text{Fe}$ -AMS standard**



## 5 The standard production via



The production of an AMS reference material, of a defined  ${}^{55}\text{Fe}/{}^{56}\text{Fe}$ - ratio, is required in order to determine precisely the neutron capture cross section for  ${}^{54}\text{Fe}(\text{n},\gamma)$ . This chapter will summarize the production of several  ${}^{55}\text{Fe}$ -AMS reference materials via proton capture on  ${}^{54}\text{Fe}$ . Chapter 6 will describe a second, independent method which was used to produce a  ${}^{55}\text{Fe}$ -AMS reference material.

### 5.1 Principle

Several iron samples were irradiated with protons in order to produce a specific amount of radioactive  ${}^{55}\text{Co}$ -atoms (see equation 4.5) via proton capture ( $\text{p},\gamma$ ) on  ${}^{54}\text{Fe}$ . As  ${}^{55}\text{Co}$  ( $t_{1/2} = 17.53 \pm 0.03$  h [Junde, 2008]) decays to  ${}^{55}\text{Fe}$ , it is calculated that after 10  ${}^{55}\text{Co}$ -half-lives, the number of produced  ${}^{55}\text{Co}$ -atoms equals the number of produced  ${}^{55}\text{Fe}$ -atoms ( $t_{1/2} = 2.744 \pm 0.009$  years [Junde, 2008]).

Each  ${}^{55}\text{Co}$ -decay is followed by the deexcitation of  ${}^{55}\text{Fe}$  to its ground state, emitting among others the most common  $\gamma$ - ray of 931.1 keV with an emission probability  $p_\gamma$  of 75% (see also decay scheme of  ${}^{55}\text{Co}$  in figure 3.5). The number of emitted  $\gamma$ -rays is measured with a high purity germanium diode to determine the activity of the sample (see equation 4.8) and finally the amount of produced  ${}^{55}\text{Fe}$  atoms (see equation 4.7).

### 5.2 Preconsiderations

The isotopic ratio  $N_{55\text{Fe}}/N_{54\text{Fe}}$  of several irradiated iron samples, which shall be measured by AMS, is in the  $10^{-15} - 10^{-11}$  range. The isotopic ratio of the  ${}^{55}\text{Fe}$ -AMS reference material should be around  $10^{-12}$ , high enough to provide a high  ${}^{55}\text{Fe}$ -count rate for good statistics. The main parameters, which influence the isotopic ratio, are the proton capture cross section  $\sigma_{\text{p},\gamma}(E)$  on  ${}^{54}\text{Fe}$  and the proton fluence  $\Phi$ .

The cross section value  $\sigma_{\text{p},\gamma}(E)$  increases with increasing proton energy (2.1 mbarn or 0.09 mbarn for 5 MeV protons (see table 3.4)). Discrepant cross section values only allow a rough estimate of the required proton fluence, which is derived from equation 2.12:

$$\Phi = N_p / (\text{cm}^2) = \frac{N_{55\text{Co}} / N_{54\text{Fe}}}{\sigma_{\text{p},\gamma}(E)}. \quad (5.1)$$

Assuming a cross section  $\sigma_{p,\gamma}(E)$  of about 1 mbarn and  $N_{^{54}\text{Fe}}/N_{^{55}\text{Co}} \approx 10^{-12}$ , one gets  $\Phi \approx 10^{15}$  protons/cm<sup>2</sup>, which equals, e.g. a proton current of 100 nA/cm<sup>2</sup> for an irradiation time of nearly half an hour. But this value is by far too optimistic, because a 5 MeV proton experiences its total energy loss (see section 2.1.3 and Bethe-Bloch equation 3.7) within the first 80  $\mu\text{m}$  of the iron sample, which implies a decrease of the cross section. In addition, the amount of produced radionuclides decreases when the sample does not consist of 100%  $^{54}\text{Fe}$ -atoms.

After the irradiation, the radioactive isotope  $^{55}\text{Co}$  will not be distributed homogeneously in the sample, because the profile of the incident proton beam is Gaussian and because the 5 MeV protons don't penetrate the iron sample, but are stopped within the first 80  $\mu\text{m}$ .

The expected count-rate of the 931 keV  $\gamma$ - ray is determined:

A  $^{54}\text{Fe}$ -sample, 1 cm<sup>2</sup> in size and 100  $\mu\text{m}$  of thickness, weights about 80 mg and consists of  $N_{^{54}\text{Fe}} \approx 9 \cdot 10^{20}$  atoms. Thus, the number of required  $^{55}\text{Fe}$ -atoms is  $N_{^{55}\text{Fe}} \approx 9 \cdot 10^8$ . With an emission probability  $p_\gamma \approx 75\%$  and a detector efficiency  $\epsilon_\gamma \approx 0.4\%$ , the corresponding count-rate is about 27 counts per second. In this case, 1000 seconds measuring would be sufficient to get a statistic at uncertainty  $< 1\%$ .

## 5.3 Experimental procedure

### 5.3.1 Samples

Three different samples were irradiated with protons. Their isotopic and chemical specifications are shown in table 5.1. (For the composition of natural iron and the atomic masses see also table 3.1).

For the proton irradiations, the iron powder had to be pressed into pellets. Therefore, a sample press (for 9 mm pellets in diameter) was borrowed from Ao. Prof. Mag. Dr. Herwig Peterlik (University of Vienna) and based on this one, two new sample presses (for 6 mm and 9 mm pellets in diameter) were made in our mechanical workshop.

The middle picture in figure 5.1 shows the single pieces of the 6 mm sample press: a short stamp (6 mm in diameter), the matrix, which consists of the outer matrix (made out of carbid/hart metal) and the inner matrix (made out of glass ceramics), and the long stamp.

Iron powder is pressed to a pellet as follows:

First the short stamp is introduced into the matrix, the powder is added and the longer stamp is inserted. The powder, which lies now inside the matrix between both stamps, is pressed to a pellet by a hydraulic press (using a pressure of about 5t/cm<sup>2</sup>). Then the shorter stamp is taken out and with the longer stamp one presses out the

sample name	specifications (producer)	isotopic composition [%]	molar mass [g/mol]
<i>pg_A</i>	natural Fe-powder (Merck)	$^{54}\text{Fe}$ 5.85 $^{56}\text{Fe}$ 91.75 $^{57}\text{Fe}$ 2.12 $^{58}\text{Fe}$ 0.282	55.845(2)
<i>pg_B</i>	enriched $^{54}\text{Fe}$ -foil (STB)	$^{54}\text{Fe}$ 99.84 $^{56}\text{Fe}$ 0.14 $^{57}\text{Fe}$ < 0.01 $^{58}\text{Fe}$ < 0.01	53.94
<i>pg_C</i>	enriched $^{54}\text{Fe}$ -powder (STB)	$^{54}\text{Fe}$ 99.86 $^{56}\text{Fe}$ 0.13 $^{57}\text{Fe}$ 0.025 $^{58}\text{Fe}$ 0.0006	53.95

**Table 5.1:** Specification of the sample material, used for the (p, $\gamma$ ) irradiations.

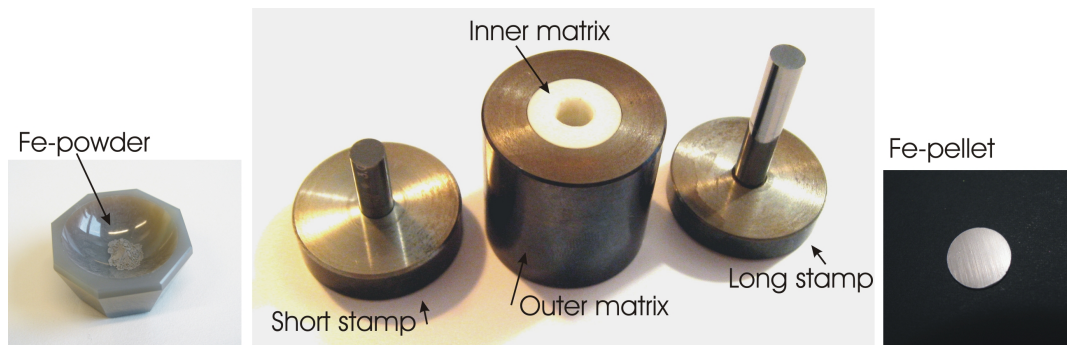


**Figure 5.1:** The left picture shows a natural iron powder in a mortar. The powder is then filled into the sample press and closed with the longer stamp in the middle picture. The right picture shows a typical iron pellet of 6 mm in diameter

iron pellet, slowly and carefully by means of the hydraulic press and an additional hart metal ring.

For the construction of the sample press, especially the material was of great importance. The material of the stamps has to stand great pressure ( $\approx 5 \text{ t/cm}^2$ ) and was chosen to be hart metal. Furthermore, it is important that the stamps fit exactly parallel into the inner matrix, which was made out of MACOR - Machinable Glass Ceramic. The matrices were not glued together (not stable enough) but were mounted during a heated phase of the outer hart metal. In the cooling phase the hart metal shrank onto the inner matrix.

### 5.3.2 Proton Irradiations at VERA

$\text{TiH}_2$  sputter cathodes were used for the production of negatively charged protons. The Fe samples were positioned between the analyzing magnet and the electrostatic analyzer on the high energy side (see beamline section 04 in figure 5.2). There are two beamline valves, which separate the small section of the irradiation position from the rest of the vacuum system. Therefore, it does not take a long time to vent that section, insert the sample holder (see figure 5.4) and to evacuate it.

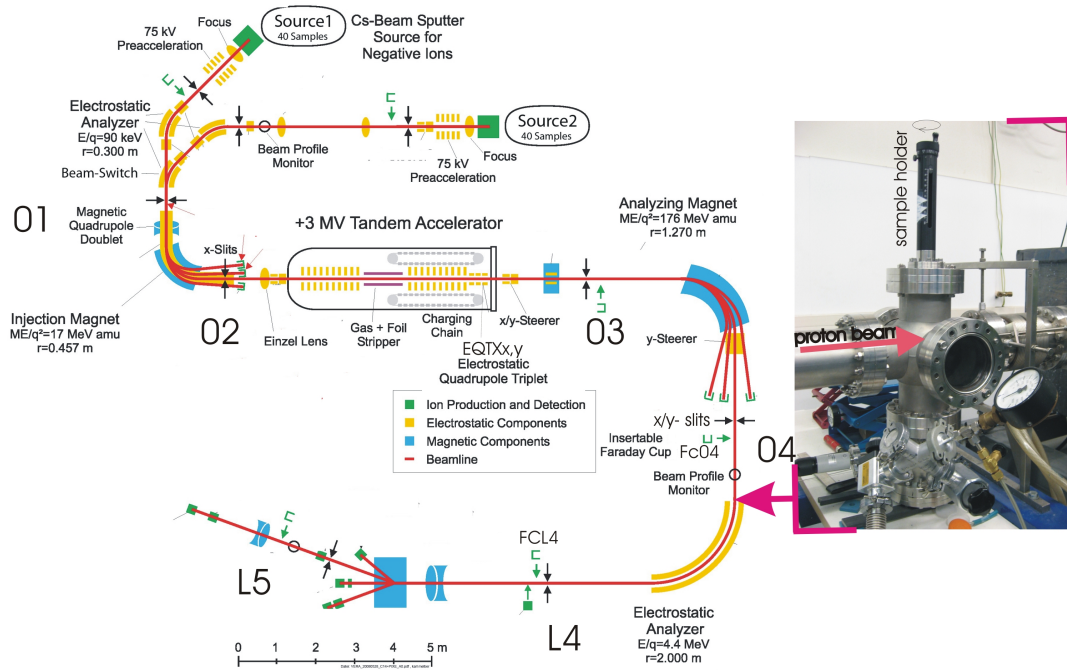


**Figure 5.2:** Position of the proton irradiation of the iron sample in section 04.

The only tricky point about the irradiation is to focus the beam right on the sample. For the irradiation of the first sample a ladder with five possible mounting positions was used (see left ladder in figure 5.3). For the tuning of the  $p^+$  beam the ladder was moved to force the protons pass a 4 mm aperture. Unfortunately the possibilities of detecting a current behind the ladder were limited, because the Faraday cup (and the beam profile monitor) in section 04 are located in front of the ladder and the next cup is positioned after the electrostatic analyzer in section L4 (see figure 5.2). However, the electrostatic analyzer is capable to analyze only proton energies of maximal  $\approx 4$  MeV and it is almost impossible to scale those protons from 4 MeV to 5.5 MeV, because every scale attempt causes a significant change of the beam trajectory so that the proton beam is not focused onto the sample anymore. So the first sample, pg\_A, was just irradiated at a proton energy of 4 MeV, using Faraday Cup FCL4 for monitoring the current of the proton beam.

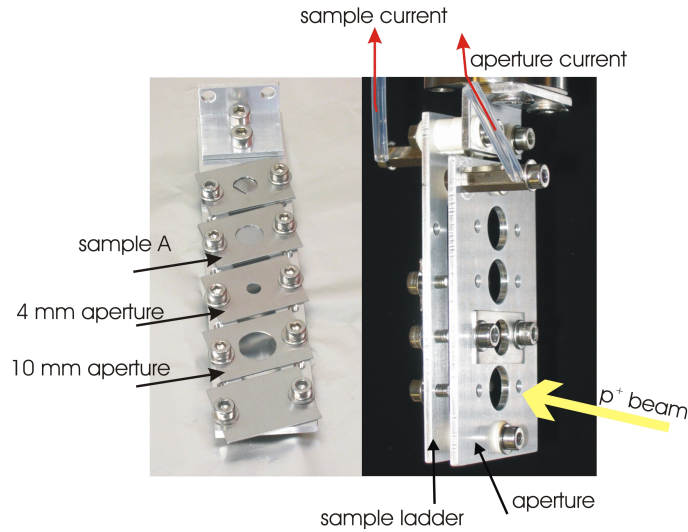


**Figure 5.3:** Sample holders. The left ladder with five different mounting positions was used for sample pg\_A. The right ladder, which consists of the front aperture and the rear sample ladder (each one connected to a wire for a current measurement) was used for samples pg\_B and pg\_C.

The advantage of a proton irradiation at 5.5 MeV instead of 4 MeV lies in the strong increase of the proton capture cross section (see table 3.4) and thus, lead to the construction of a new sample holder, which allows a (relative) current measurement (see right ladder in figure 5.3 and 5.4). Actually one can measure two different currents, one from the sample ladder and the second one from the aperture, which is mounted in front of the sample holder. With the movable aperture it is possible to monitor the position of the beam. In addition, the relative current measurement allows to monitor the irradiation history of the sample. For absolute current measurements, which were not needed here, e.g. a suppressor voltage would be required to prevent the escape from secondary electrons.

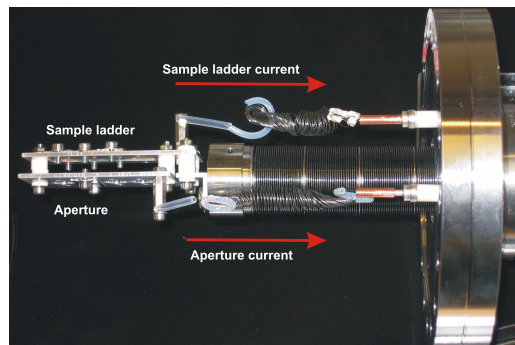


**Figure 5.4:** Side view of the sample holder, which is connected to the flange.

The proton beam, which has to be guided with minimal losses through all compo-

nents onto the iron sample, is described by the **tuning procedure**:

Selecting a tandem voltage of 2.7 MV, provide a proton energy of about 5.4 MeV. In the first step all components on the low energy side were tuned by guiding an attenuated proton beam of about 60 nA to Faraday Cup FC04. Then the terminal voltage TV and the steerers in section 04 were optimized, followed by the quadrupols and the steerers in section 03, which needed to be optimized together, because they influence each other.

In the case of sample pg\_A, which was irradiated with an proton energy of about 4 MeV (at a terminal voltage of 2 MV), the tuning was performed optimizing the proton current at Faraday Cup FCL4, situated after the electrostatic analyzer.

Sample pg\_B and pg\_C were irradiated at a higher terminal voltage of 2.7 MV, resulting in a proton energy of 5.4 MeV. In these cases, the beam was optimized to the sample position by measuring the beam current on the aperture and the sample ladder (see figure 5.3, 5.4).

All details concerning the proton irradiations are summarized in table 5.2. Figure 5.5 shows the time dependent proton current during the irradiation time  $T_{irr}$  on sample pg\_B and pg\_C.

sample name	mass m [mg]	Energy $E_{p^+}$	Mean current $I_{p^+}$ [nA]	Duration $T_{irr}$ [min]	Irradiation End $t_{Irr,E}$
(A) pg_Fe9mm	47.24(2)	4 MeV	$\approx 148$	113	17.07.2008 13:03:00
(B) pg_54FeFoil	53.96(2)	5.5 MeV	$\approx 163$	265	25.08.2008 17:00:00
(C) pg_54Fe6mm	47.45(2)	5.5 MeV	$\approx 287$	211	30.9.2008 17:17:00
	47.45(2)	5.5 MeV	$\approx 156$	148	3.10.2008 11:08:00

**Table 5.2:**  $^{54}\text{Fe}(p,\gamma)$  Irradiations at VERA. The uncertainty of the mass is given in brackets and corresponds to the last given number.

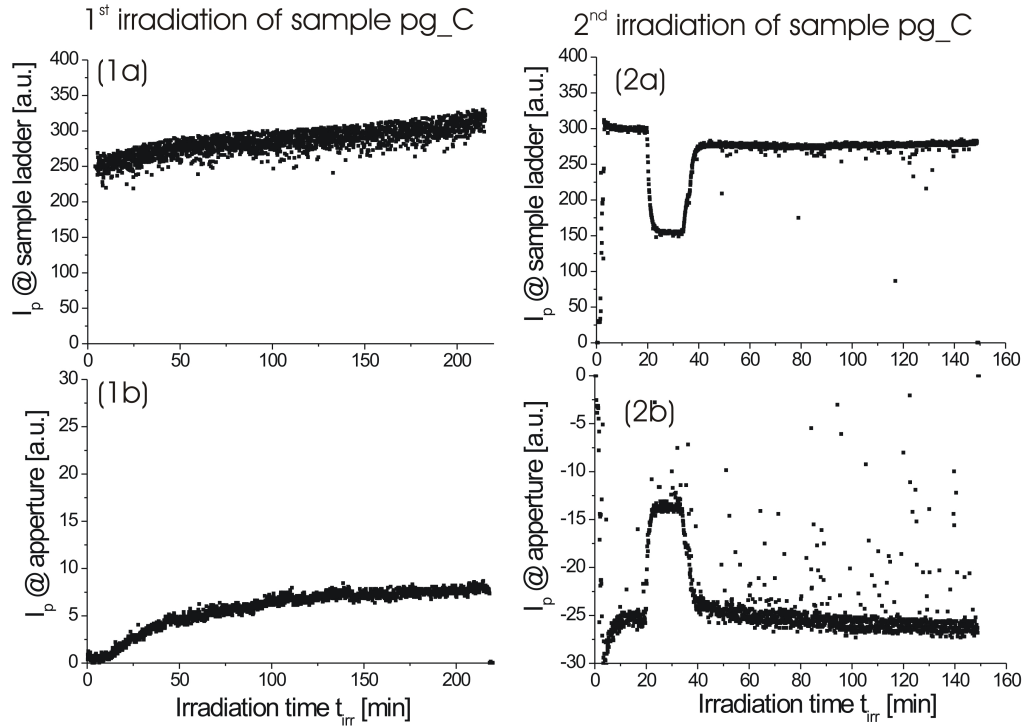


**Figure 5.5:** Proton current in arbitrary units versus irradiation time  $t_{irr}$ . The deposited charge on (a) the sample ladder and (b) the aperture is measured as the integral of the current. (1) The left figures correspond to the first irradiation and (2) the right ones to the second irradiation of sample pg\_C. During the second irradiation, the current drops from around 300 a.u. to about 150 a.u. and increases after about 20 minutes to about 280 a.u. At the same time, the current measured at the aperture increases drastically. This indicates a shift of the proton beam from the sample to the aperture.

### 5.3.3 Activity measurement of $p^+$ -irradiated samples

Directly after the proton irradiation, each sample was measured with a high purity germanium diode (HPGe) to determine the amount of produced radionuclides  $N_{55Co}$  (using equation 4.12). The final results are listed in table 5.9, but first, the activity measurement and the single contributions to the uncertainty of  $N_{55Co}$  are discussed.

Figure 5.6 shows the spectrum of the activated sample pg\_A, which was measured one hour with the HPGe diode. (See also figure 2.3 for the explanation of a typical Ge spectrum.) The net peak area was determined with the Software WIRUK [Friedman], which allows to set the region of interest individually for each peak and then to subtract the background.

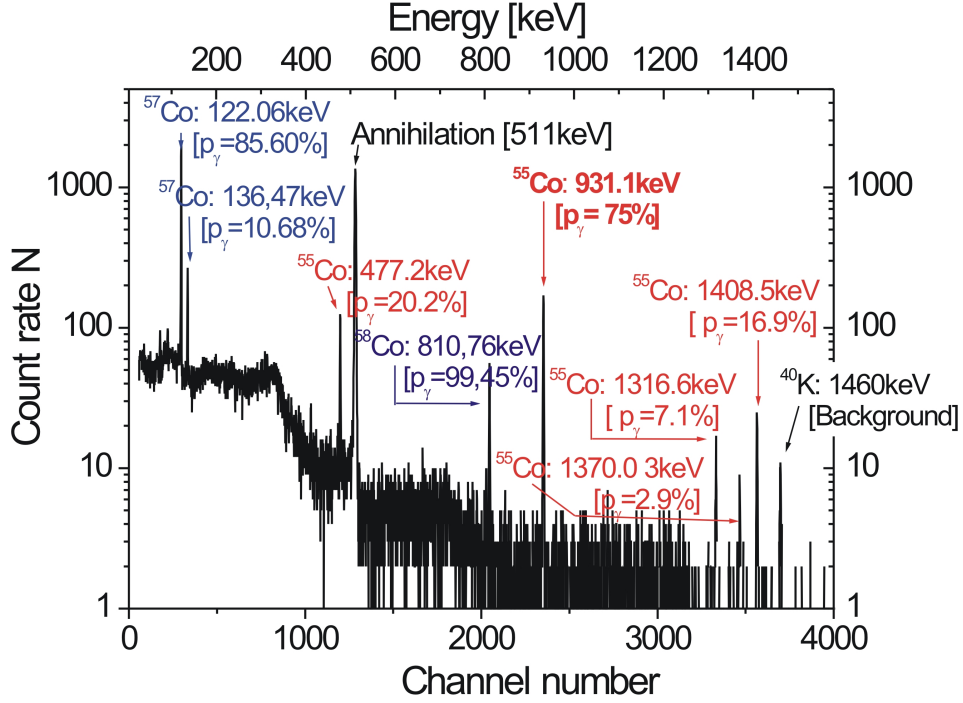


**Figure 5.6:** Spectrum of the irradiated sample pg\_A, acquired within one hour measuring time with the HPGe.

The measuring conditions and possible influences to systematical uncertainties can be summarized as follows:

The background of the detector is suppressed by a lead shielding. Dead-time losses were small enough ( $< 0.1\%$ ) and were corrected by the live-time of the detector (see equation 4.9). The contribution to the uncertainty from a displacement of the sample position can be neglected ( $< 0.1\%$ ). Pile-up could be neglected because of the small total count-rate ( $< 1000$  counts per second).

The uncertainty of the activity measurement comes from three parameters (see also equation 4.13):

The uncertainty contribution of emission probability of the  $\gamma$ - rays  $s_{p_\gamma}$ , counting statistics  $s_N$  and the efficiency of the HPGe diode  $s_{\epsilon_\gamma}$ . The first one is estimated to  $\pm 4.7\%$  for  $^{55}\text{Co}$  [Junde, 2008] and the contribution from the statistics was kept below  $\pm 1\%$  by an appropriate choice of the counting time. The uncertainty of the efficiency is about 2 % and is discussed in detail in appendix A.

## 5.4 Results and discussion for $^{54}\text{Fe}(p,\gamma)^{55}\text{Co}$ -activations

### 5.4.1 Comparison of isotopic ratios $^{55}\text{Fe}/\text{Fe}$ , deduced from the activity measurements

#### Sample pg\_A

Sample pg\_A, consisting of natural Fe, a pellet with 9 mm in diameter (see table 5.2 for details), was measured with the Ge-diode 60 times, each spectrum acquired for 1 hour. After the eighth hour, the germanium diode did not acquire anymore and was started again after the 20th hour. The counting rate at the beginning of the measurement was about 0.2 counts per second for the 931 keV  $\gamma$ -line. For better counting statistics, spectrum 1.-8., 21.-40 and 40.-60 were summed up and then analysed with WIRUK. The amount of produced  $^{55}\text{Fe}$  was then calculated individually for each of the three sum-spectra. The weighted mean of  $N_{^{55}\text{Co},total}$  (including only statistical uncertainties  $\sigma_i^w$ ) divided by the amount of stable  $^{54}\text{Fe}$  (and  $^{56}\text{Fe}$ ) lead to the results given in table 5.3 and 5.9.

$E_\gamma$ [keV]	$C_{coinc}$	$N_{^{55}\text{Fe},total}$	$\sigma_i^w$ [%]	$s_{p_\gamma}$ [%]	$s_{\epsilon_\gamma}$ [%]	$s_m$ [%]	$^{55}\text{Fe}/^{56}\text{Fe}$	$^{55}\text{Fe}/^{54}\text{Fe}$	$s_{stat.}$ [%]	$s_{syst.}$ [%]
931	1.0095	$6.84 \cdot 10^6$	0.90	4.7	2.0	0.042	$1.46 \cdot 10^{-14}$	$2.30 \cdot 10^{-13}$	0.90	5.1
477	1.0293	$7.23 \cdot 10^6$	1.3	8.4	2.0	0.042	$1.55 \cdot 10^{-14}$	$2.43 \cdot 10^{-13}$	1.3	8.7

**Table 5.3:** The amount of produced  $^{55}\text{Fe}$ -atoms in sample pg\_A after proton irradiation: Comparison of the two main  $\gamma$ -rays at 931 keV and 477 keV.

#### Sample pg\_B

Sample B, an iron-foil, highly enriched in  $^{54}\text{Fe}$  (see table 5.2 for details), was measured with the Ge-diode 60 times (per one hour measuring time). After the first spectrum, the HPGe diode "crashed" and was started again after 17 hours. After 30 hours the sample was turned around to study the influence of photon attenuation and sample positioning. The weighted mean of  $N_{^{55}\text{Co},total}$  over all acquired spectra (including only statistical uncertainties) divided by the amount of stable  $^{54}\text{Fe}$  lead to the results given in table 5.4 and 5.9.

$E_\gamma$ [keV]	$C_{coinc}$	$N_{^{55}\text{Fe},total}$	$\sigma_i^w$ [%]	$s_{p_\gamma}$ [%]	$s_{\epsilon_\gamma}$ [%]	$s_m$ [%]	$^{55}\text{Fe}/^{54}\text{Fe}$	$s_{stat.}$ [%]	$s_{syst.}$ [%]
931	1.0095	$6.21 \cdot 10^8$	0.11	4.67	2.0	0.04	$1.03 \cdot 10^{-12}$	0.11	5.1
477	1.0293	$6.37 \cdot 10^8$	0.20	8.42	2.0	0.04	$1.06 \cdot 10^{-12}$	0.20	8.7
1408	0.9703	$5.88 \cdot 10^8$	0.31	8.42	2.0	0.04	$9.78 \cdot 10^{-13}$	0.31	4.6

**Table 5.4:** The amount of produced  $^{55}\text{Fe}$ -atoms in sample pg\_B after proton irradiation: Comparison of the three main  $\gamma$ -rays at 931 keV, 477 keV and 1408 keV, measured with the HPGe-diode at VERA.

### Sample pg\_C

After the first irradiation, sample pg\_C, a 6 mm iron pellet, highly enriched in  $^{54}\text{Fe}$  (see table 5.2 for details), was measured with the Ge-diode 7 times in a series of 1 hour measurements. Then it was turned around and the measurement-series continued.

$N_{55\text{Co},total}$  was measured for each spectrum and their weighted mean (only statistical uncertainties contributed to the weight), was then divided by the number of stable  $^{54}\text{Fe}$ -isotopes. The results for three different  $\gamma$ -rays are listed in table 5.5.

$E_\gamma$ [keV]	$C_{coinc}$	$N_{55\text{Fe},total}$	$\sigma_i^w$ [%]	$s_{p_\gamma}$ [%]	$s_{\epsilon_\gamma}$ [%]	$s_m$ [%]	$^{55}\text{Fe}/^{54}\text{Fe}$	$s_{stat.}$ [%]	$s_{syst.}$ [%]
931	1.0095	$3.77 \cdot 10^8$	0.15	4.7	2.0	0.04	$7.13 \cdot 10^{-13}$	0.15	5.1
477	1.0293	$3.89 \cdot 10^8$	0.23	8.4	2.0	0.04	$7.35 \cdot 10^{-13}$	0.23	8.7
1408	0.9703	$3.58 \cdot 10^8$	0.48	4.1	2.0	0.04	$6.78 \cdot 10^{-13}$	0.48	4.6

**Table 5.5:** The amount of produced  $^{55}\text{Fe}$ -atoms in sample pg\_C after the first proton irradiation: Comparison of the three main  $\gamma$ -rays at 931 keV, 477 keV and 1408 keV, measured with the HPGe-diode at VERA.

For a comparison, this pellet was also measured with a different Ge-diode at the Vienna Atominstitut (ATI). It was measured a couple of times, for different measurement times (half an hour, one hour and two hours). Table 5.6 shows the weighted mean of  $N_{55\text{Co},total}$  for the acquired spectra and the isotopic ratio  $^{55}\text{Fe}/^{54}\text{Fe}$  for three different  $\gamma$ -lines.

$E_\gamma$ [keV]	$N_{55\text{Fe},total}$	$\sigma_i^w$ [%]	$s_{p_\gamma}$ [%]	$s_{\epsilon_\gamma}$ [%]	$s_m$ [%]	$^{55}\text{Fe}/^{54}\text{Fe}$	$s_{stat.}$ [%]	$s_{syst.}$ [%]
931	$3.56 \cdot 10^8$	0.11	4.7	2.0	0.04	$6.73 \cdot 10^{-13}$	0.11	5.1
477	$3.43 \cdot 10^8$	0.20	8.4	2.0	0.04	$6.48 \cdot 10^{-13}$	0.20	8.7
1408	$3.63 \cdot 10^8$	0.27	4.1	2.0	0.04	$6.86 \cdot 10^{-13}$	0.27	4.6

**Table 5.6:** The amount of produced  $^{55}\text{Fe}$ -atoms in sample pg\_C after the first proton irradiation: Comparison of the three main  $\gamma$ -rays at 931 keV, 477 keV and 1408 keV, measured with the HPGe-diode at ATI (Vienna Atominstitut).

Three days after the first irradiation, sample pg\_C was irradiated a second time to produce a higher isotopic ratio  $^{55}\text{Fe}/^{54}\text{Fe}$ . Afterwards, it was measured with the HPGe-diode at VERA (20 spectra with an measuring time of 1 hour per spectrum).

After the second irradiation, the measured net peak areas will also contain a specific number of  $^{55}\text{Co}$ -radionuclides originating from the first proton irradiation. To take into account this contribution, the measured activity  $A(t_{irr2,E})$  in equation 4.7 has to be first subtracted by the determined number of radionuclides from the first irradiation  $N_{55\text{Co}}(t_{irr2,E}) \cdot \lambda_{55\text{Co}}$ . By this way, the number of  $^{55}\text{Co}$ -atoms are calculated, which are only produced during the second irradiation. The results are shown in table 5.7.

$E_\gamma$ [keV]	$C_{coinc}$	$N_{^{55}\text{Fe},total}$	$\sigma_i^w$ [%]	$s_{p,\gamma}$ [%]	$s_{\epsilon_\gamma}$ [%]	$s_m$ [%]	$^{55}\text{Fe}/^{54}\text{Fe}$	$s_{stat.}$ [%]	$s_{syst.}$ [%]
931	1.0095	$3.10 \cdot 10^8$	0.14	4.7	2.0	0.04	$5.86 \cdot 10^{-13}$	0.14	5.1
477	1.0293	$3.25 \cdot 10^8$	0.22	8.4	2.0	0.04	$6.14 \cdot 10^{-13}$	0.22	8.7
1408	0.9703	$2.96 \cdot 10^8$	0.36	4.1	2.0	0.04	$5.59 \cdot 10^{-13}$	0.36	4.6

**Table 5.7:** The amount of produced  $^{55}\text{Fe}$ -atoms in sample pg\_C after the second proton irradiation: Comparison of the three main  $\gamma$ -rays at 931 keV, 477 keV and 1408 keV, measured with the HPGe-diode at VERA.

The total amount of produced  $^{55}\text{Fe}$  radionuclides is the sum over both irradiations and is given in 5.8.

$E_\gamma$ [keV]	$C_{coinc}$	$N_{^{55}\text{Fe},total}$	$\sigma_i^w$ [%]	$s_{p,\gamma}$ [%]	$s_{\epsilon_\gamma}$ [%]	$s_m$ [%]	$^{55}\text{Fe}/^{54}\text{Fe}$	$s_{stat.}$ [%]	$s_{syst.}$ [%]
931	1.0095	$6.86 \cdot 10^8$	0.21	4.7	2.0	0.04	$1.30 \cdot 10^{-12}$	0.21	5.1
477	1.0293	$7.13 \cdot 10^8$	0.31	8.4	2.0	0.04	$1.35 \cdot 10^{-12}$	0.31	8.7
1408	0.9703	$6.53 \cdot 10^8$	0.60	4.1	2.0	0.04	$1.24 \cdot 10^{-12}$	0.60	4.6

**Table 5.8:** The amount of produced  $^{55}\text{Fe}$ -atoms in sample pg\_C after both proton irradiations: Comparison of the three main  $\gamma$ -rays at 931 keV, 477 keV and 1408 keV, measured with the HPGe-diode at VERA.

The final results of the  $^{55}\text{Fe}/\text{Fe}$  ratios of the samples pg\_A, pg\_B and pg\_C are listed in table 5.9.

### 5.4.2 Discussion about the isotopic ratios $^{55}\text{Fe}/^{54}\text{Fe}$

#### 477 keV - 931 keV - 1408 keV @VERA

The analysis of the 477 keV  $\gamma$ - peak leads to results, which are systematically 1-2% higher compared to the results coming from the 931 keV  $\gamma$ - peak.

The analysis of the 1408 keV  $\gamma$ - peak leads to results, which are systematically 1-2% smaller compared to the results coming from the 931 keV  $\gamma$ - peak.

In summary, the results taken from the 931 keV  $\gamma$ - peak deviates 1-2% from the other  $\gamma$ - peaks.

#### Coincidence summing correction $C_{coinc}$

The expectation to get a more precise  $^{55}\text{Fe}/^{54}\text{Fe}$ - ratio after a coincidence summing correction (discussed in chapter A.1.1) shows, that the scatter of the data is higher than expected. The resulting deviation of the  $^{55}\text{Fe}/^{54}\text{Fe}$ - ratio is up to 5%, comparing the 477 keV and 931 keV- analysis, and up to -10%, comparing the 1408 keV and 931 keV- analysis (see results for sample pg\_C in table 5.8). This can be due to the uncertainty of the total efficiency (3-10%). In addition, the threshold set for the total

efficiency values, was different than the threshold, set for the activity measurements. Still, the uncertainties of the coincidence summing corrected  $^{55}\text{Fe}/^{54}\text{Fe}$ - ratios are of the same order of magnitude as the standard deviation of the emission probabilities  $p_\gamma$ .

#### **477 keV - 931 keV - 1408 keV @ATI**

The analysis performed with the 477 keV  $\gamma$ - peak gives 3-4% smaller values than the results obtained from the 931 keV  $\gamma$ - peak. The analysis performed with the 1408 keV  $\gamma$ - peak is 1-2% larger than the results obtained from the 931 keV  $\gamma$ - peak (see results for sample pg\_C in table 5.6).

The relative deviations between the three  $\gamma$ - lines show a different behaviour for both germanium diodes. One possible reason for this deviation is, that the values from the Ge-diode at ATI were not coincidence summing corrected, because the total efficiency curve was not known. The deviation can not be due to the analysis method, because the net peak areas of all spectra were derived by the software WIRUK. Even the independent analysing program GENIE leads to results differing less than 1 %.

#### **Ge-diode ATI / VERA**

The deviation of the  $^{55}\text{Fe}/^{54}\text{Fe}$ - ratio obtained from the 931 keV  $\gamma$ - peak at VERA and at ATI is about 4%. The origin of this deviation lies probably in the limited knowledge of the full-energy peak efficiencies of the detectors, which have an uncertainty of about 2 %.

#### **Influence of mass attenuation**

The sample was turned upside down to study the influence of the photon attenuation in the sample itself. Using the mass attenuation coefficients listed in table 4.2, the count-rate was then corrected and no deviations were observed.

#### **5.4.3 Final Results of $^{55}\text{Fe}/^{54}\text{Fe}$**

The 931 keV  $\gamma$ -ray is the most intense  $\gamma$ -ray ( $p_\gamma = 75\%$ ) of the  $^{55}\text{Co}$ -decay. For this  $\gamma$ -ray, the coincidence summing correction is  $< 1\%$  and, therefore, causes the smallest correction compared to about  $\pm 3\%$  for the 931 keV and 1408 keV  $\gamma$ -ray.

As final  $^{55}\text{Fe}/^{54}\text{Fe}$  ratio, the values obtained from the 931 keV  $\gamma$ -ray analysis were taken and are listed in table 5.9.

sample	$E_\gamma$ [keV]	Reference Date	$^{55}\text{Fe}/^{54}\text{Fe}$ corr.	$s_{stat.}$	$s_{syst.}$
pg_Fe9mm (pg_A)	931	17.07.2008 13:03:00	$2.30 \cdot 10^{-13}$	0.90%	5.08%
pg_54FeFoil (pg_B)	931	25.08.2008 17:00:00	$1.03 \cdot 10^{-12}$	0.11%	5.08%
pg_54Fe6mm (pg_C)	931	03.10.2008 11:08:00	$1.30 \cdot 10^{-12}$	0.11%	5.08%

**Table 5.9:** Isotope ratios of three Fe samples, which were bombarded with protons to produce  $^{55}\text{Fe}$  via  $^{54}\text{Fe}(p,\gamma)^{55}\text{Co}$ .

#### 5.4.4 Measurement of the half-life of $^{55}\text{Co}$

As a by-product of the plenty activity measurements, the half-life of  $^{55}\text{Co}$  was measured.

The number of radionuclides decreases exponentially with time, described by  $N(t) = N(0)e^{-\lambda t}$  with  $\lambda = \ln 2/t_{1/2}$ . In this regard, the number of detected counts will decrease exponentially with time too and the half-life  $t_{1/2}$  can be derived if the detected counts are plotted against the time. This was done with the program Origin by two different approaches: an exponential fit and a linear fit. The pro and contras are discussed below.

#### Comparison of the different fit methods

First, one has to consider which count-rate has to be plotted against time: The net peak area, which was acquired during one hour, the count-rate per second or the true count-rate? If  $T_M \ll t_{1/2}$ , the count-rate at the beginning and at the end of the measuring time will be the same. In the case of  $^{55}\text{Co}$ , where 1 hour measuring time has to be compared to a half-life of 17 hours, both count-rates will differ from each other and the resulting count-rate per second will be valid for the middle of the irradiation time (not the time, where the integral is the same). In addition, one has to account for the dead time of the detector, which is not constant but which decreases with decreasing counting rate ( $\approx 10$  counts per second). Summing up, the true count-rate at the beginning of each HPGe-measurement  $n_{true}(t_{MA})$  (see equation 4.10) was plotted against time.

A linear fit of data points, which were transformed to a logarithmical scale, requires a background subtraction of the data points [Tagesen & Winkler, 1993]. This was already done during the peak analysis. In the exponential fitting, the function  $y = Ae^{-\ln 2/t}$  was used.

Both fits were performed including the statistical uncertainty of the count-rate ( $<1\%$ ) as weight. In the case of the exponential fit, the weight was  $1/s_{n_{true}}^2$  and in the case of the linear fit, where  $y = \ln(n_{true})$ , the weight was the relative uncertainty  $s_{n_{true}}/n_{true}$ . If the statistical uncertainty is bad, the half-life value, derived from the linear fit, is shifted to lower half-life values due to the asymmetry of the uncertainties in the logarithmical scale.

### Fitting results for sample pg\_B and pg\_C

Sample pg\_B was measured with the Ge-diode in a series of 1-hour measurements, in total 60 times ( $> 3 t_{1/2}$ ). Unfortunately the acquiring system crashed after the first spectrum. Data were accumulated again 16 h later. The position of the sample was not changed for the first 40 spectra. Then the sample was turned upside down and that's why the spectra 40 - 60 were corrected with the mass attenuation correction factors (given in table 4.2). The correction is of the order of 0.1%. The sample position towards the detector is well reproducible ( $< 0.1\%$  effects) and thus, can be neglected.

In figure 5.7, the true count-rate  $n_{true}(t_M)$  is plotted versus the measuring time  $t_M$ , where the left fit is exponential and the right one linear in a logarithmical scale.

The calculated true count-rates at the beginning of the measurements (see equation 4.9 and 4.10) were  $(10.432 \pm 0.063) s^{-1}$  for the 477 keV  $\gamma$ -line,  $(19.390 \pm 0.076) s^{-1}$  for the 931-  $\gamma$ -line and  $(2.961 \pm 0.029) s^{-1}$  for the 1408 keV  $\gamma$ -line and are represented by the parameter A.

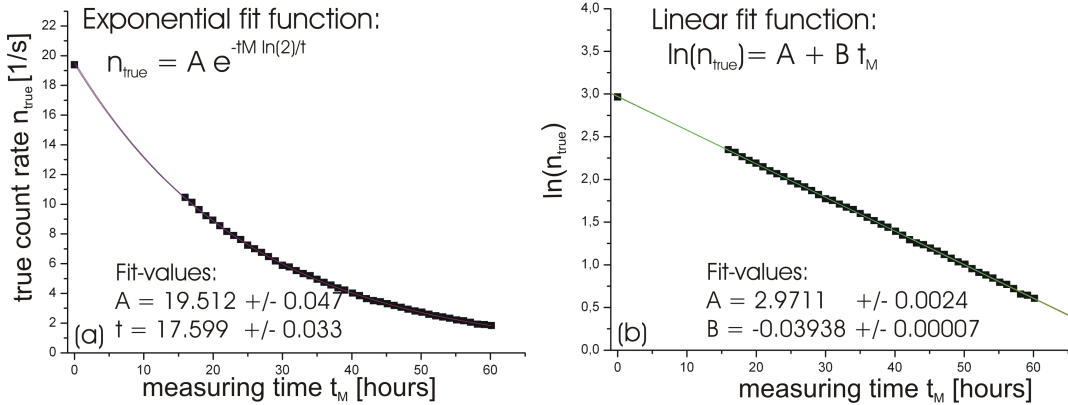


**Figure 5.7:** True count-rate  $n_{true}(t_M)$  plotted against the measuring time  $t_M$ . (a) On the left side is the exponential fit of  $n_{true}(t_{irr})$  and (b) the right side shows the linear fit of  $\ln(n_{true}(t_{irr}))$ . The half-life of  $^{55}\text{Co}$  is derived from the fitting parameters  $t$  and  $B$ , respectively.

Table 5.10 shows a summary of the fitting results for the three main  $\gamma$ -lines of the  $^{55}\text{Co}$ -decay of sample pg\_B. In addition, the influence of the amount of datapoints was studied. So, the column called "data" shows the datapoints, which were used for the evaluation. The values on the left side correspond to the results of the exponential fit and the right side correspond to the results obtained by the linear fit.

The more data points are used for a fit, the smaller is the uncertainty of the fit. The comparison of the half-life values obtained from the three  $\gamma$ -lines show good agreement to each other within  $1 \sigma$ . The linear fit agrees well with the exponential fit and shows only for the third evaluation (datapoints from spectra 16-40 h) a larger

deviation.

<b>(1) Exp. fit</b>		<b>(1) A</b>		$\frac{\chi^2}{f}$	<b>Data</b>	$E_\gamma$ keV	<b>(2) Lin. fit</b>		<b>A</b>	
$t_{1/2}$ [h]	$\pm$ [h]	[ $s^{-1}$ ]	$\pm$ [ $s^{-1}$ ]				$t_{1/2}$ [h]	$\pm$ [h]	[ $s^{-1}$ ]	$\pm$ [ $s^{-1}$ ]
17.565	0.062	10.476	0.047	1.412	0-60h	477	17.570	0.062	10.474	0.048
17.599	0.033	19.512	0.047	0.950	0-60h	931	17.602	0.033	19.513	0.047
17.402	0.093	2.939	0.020	1.154	0-60h	1408	17.416	0.092	2.938	0.020
17.52	0.12	0.38%			0-60h		17.53	0.12	0.38%	
17.767	0.088	10.389	0.050	1.075	0-40h	477	17.768	0.091	10.389	0.052
17.667	0.058	19.459	0.063	1.059	0-40h	931	17.669	0.058	19.460	0.063
17.42	0.14	2.937	0.024	0.920	0-40h	1408	17.42	0.13	2.938	0.022
17.62	0.18	0.58%			0-40h		17.62	0.17	0.59%	
17.89	0.14	10.313	0.085	1.065	16-40h	477	17.782	0.315	10.17	0.34
17.561	0.088	19.58	0.10	1.001	16-40h	931	17.72	0.14	19.21	0.30
17.66	0.21	2.894	0.037	0.877	16-40h	1408	17.73	0.54	2.83	0.16
17.70	0.27	0.89%			17-40h		17.75	0.65	2.10%	

**Table 5.10:** Half-life of  $^{55}\text{Co}$ . (1) The left values are calculated from the exponential fit. (2) The values on the right side are obtained from the linear fit. Three different time sections were used to study the influence of the number of used data points.

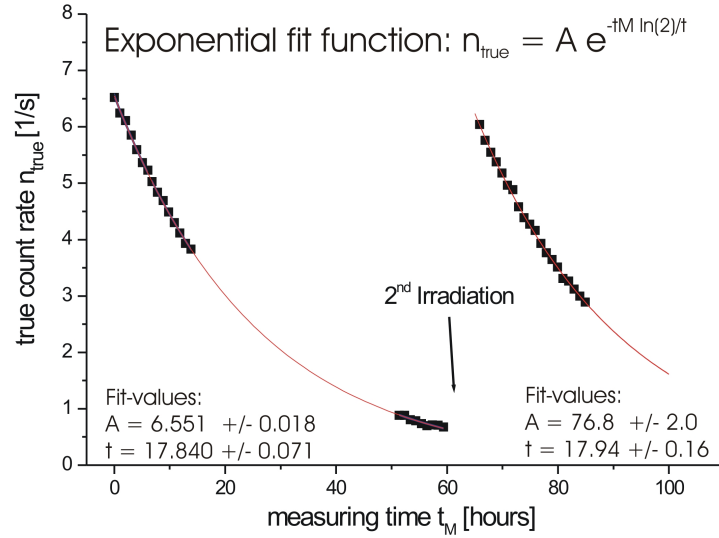


**Figure 5.8:** Exponential decay of the true count-rate  $n_{\text{true}}(t_M)$  with time after the first and the second proton irradiation. The half-life of  $^{55}\text{Co}$  is derived from the parameters of the exponential fit.

Figure 5.8 shows the fitting results for sample pg\_C, which was measured with the HPGe-diode after the first and also after the second proton irradiation.

It was shown, that a half-life of a radionuclide can be derived from sequential activity measurements, e.g. performed with a high purity germanium diode. The uncertainty of the result is independent of the uncertainty of the efficiency and of the emission probability of the  $\gamma$ -ray, etc. However, it is important to compare different fit results (from various evaluations) in order to deduce the uncertainty of the half-life.

The final result of the  $^{55}\text{Co}$  half-life from these data value was determined to  $(17.6 \pm 0.1)$  h and is in perfect agreement with the recommended value from [Junde, 2008] (see table 5.11).

	$t_{1/2}$ ( $^{55}\text{Co}$ ) [h]	$\pm$ [h]
This thesis	17.6	0.1
Junde, 2008	17.53	0.03

**Table 5.11:** The half-life of  $^{55}\text{Co}$ .

## 6 The standard production via an activity solution

The unsatisfying high systematic uncertainty of the  $^{55}\text{Fe}$ -AMS reference samples - produced via proton capture on  $^{54}\text{Fe}$  - lead to the preparation of another series of standards by means of a different, independent method, not limited by systematic uncertainties in the decay scheme of  $^{55}\text{Co}$ :

A dilution series of a certified, well-known  $^{55}\text{Fe}$ -activity standard solution (see [PTB, 2009]) was performed. The uncertainty of the standard solution is quantified to 1.57% ( $1\sigma$ ) by the PTB (Physikalische Technische Bundesanstalt Braunschweig, Germany). The activity of the standard solution on the reference date of the 1<sup>st</sup> October 2008 (00:00 CET) is  $(574.63 \pm 9.02)$  kBq, which equals  $(7.18 \pm 0.12) \cdot 10^{13}$   $^{55}\text{Fe}$ -atoms (using  $N = \frac{A}{\lambda}$ ). A certain known amount of stable  $^{56}\text{Fe}$ -atoms was added to get the  $^{55}\text{Fe}/^{56}\text{Fe}$  ratio of interest.

### 6.1 $^{55}\text{Fe}$ - activity standard solution

The specifications of the  $^{55}\text{Fe}$  activity solution from PTB are listed below:

- **The chemical composition of the aqueous solution:**  
HCl  $\equiv$  0.1 mol/L and FeCl<sub>3</sub>  $\equiv$  58 mg/L.
- **The mass of the solution:**  
 $m = (2.0022 \pm 0.0017)$  g
- **The specific activity**  
 $a = (278 \pm 9)$  kBq/g  
was determined with a liquid-scintillation spectrometer by the CIEMAT/NIST method [Kossert & Carles, 2006]. Its uncertainty is given at  $2\sigma$  (ISO, 1995) with a coverage probability of approximately 95%.

### 6.2 Experimental procedure

As tracer,  $^{56}\text{Fe}$  had to be added to the PTB- $^{55}\text{Fe}$  activity solution. Therefore, four 5 cm x 5 cm Fe-foils of natural isotopic composition were ordered from Goodfellow Cambridge Ltd. and dissolved in hydrochloric acid.

### 6.2.1 Dissolving the Fe-foils

Each goodfellow Fe-foil was cleaned with acetone, weighted with a SARTORIUS scale (see masses in table 6.1) and transferred into a glass bottle (250 ml). Concentrated hydrochloric acid was added (about 100 - 150 ml) for dissolving the foils and some drops of  $HNO_3$  were added for the acceleration of the dissolving process. The chemical composition of the dissolved Fe-foil is iron chloride ( $FeCl_3$ ).

	Mass [g]
Fe-foil #1	9.89222
Fe-foil #2	9.85122
Fe-foil #3	9.86155
Fe-foil #4	10.00662

**Table 6.1:** Masses of the Goodfellow Cambridge Ltd Fe-Foils. The uncertainty is  $\pm 0.00050$  g.

### 6.2.2 Dilution series

In the first step, a Master-solution "M" (stock solution) was produced. Then, two small amounts of the master-solution were further diluted with iron chloride  $FeCl_3$ . By this way, three samples (A0, A1 and A2) of different isotopic ratios were produced.

#### Master solution "M"

(PTB- $^{55}Fe$ ) + (Fe-foil #3)  $\rightarrow$  Master solution "M"

First of all it had to be ensured that the entire amount of activity standard solution from the ampule (PTB- $^{55}Fe$ ) was transferred into a glass bottle containing the iron chloride solution produced from dissolved Fe-foil #3. Therefore, the ampule was washed 7 times with distilled water. The glass bottle was then closed with a screw cap and was shaken several minutes to homogenise the isotopic ratio.

The 250 ml glass bottle was too heavy to be weighted with the scale. Therefore, the whole amount of the solution "M" was transferred into two plastic bottles (solution "M1" in bottle 1, solution "M2" in bottle 2). The 250 ml glass bottle was not washed afterwards because it would vary the mass of the single plastic bottle contents and thus, the respective percentage ratio of the iron content. The residue in the glass bottle ("Mr") was estimated to  $(1 \pm 0.5)$  ml out of 150 ml and was taken into account for further calculations.

Table 6.2 shows the masses of the empty plastic bottles 1 and 2, the filled bottles and the calculated mass of the solutions inside the bottles.

For further dilution steps,  $2 \times (\approx 1.5)$  ml were taken from the solution "M1" in bottle 1 ( $\approx 75$  ml) and filled into bottles M and A ( $\rightarrow$  solution "M1M" and "M1A"). The mass of the empty bottles M and A, the empty plastic bottle 1, the filled ones

and net mass of the solutions themselves are shown in table 6.3. Figure 6.1 shows the whole dilution series in a schematical view.

Weight of:	M1 [g]	±	M2 [g]	±	Mr [g]	±
Solution brutto	109.4704	0.0005	109.6878	0.0005		
Empty plastic bottle 1,2	26.48165	0.00050	24.55635	0.00050		
Solution netto	82.98875	0.00071	85.13145	0.00071	1.13	0.56
<b>Master solution netto M [sum]</b>	(169.25 ± 0.56) g					

**Table 6.2:** Mass of the Master-solution *M*, filled into bottle 1 (M1), bottle 2 (M2) and the residue (Mr), which was estimated to  $(1 \pm 0.5)$  ml out of 150 ml. The mass of the residue is determined by  $m_{Mr} = \frac{1}{150}(m_{M1} + m_{M2} + m_{Mr}) = \frac{1}{149}(m_{M1} + m_{M2})$

Weight of:	M1M [g]	±	M1A [g]	±	M1R [g]	±
Solution brutto	16.56531	0.00050	16.61141	0.00050	106.76290	
Empty centrifuge tube M, A; bottle 1	15.18175	0.00050	15.27392	0.00050	26.48165	
Solution netto	1.38356	0.00071	1.33749	0.00071	80.2813	0.0091
<b>Bottle 1 solution M1 [sum]</b>	(83.0023 ± 0.0091) g					

**Table 6.3:** Mass of M1 solution, filled into bottle M (M1M), bottle A (M1A), and the remaining rest M1R of solution M1. As a check, the sum of the masses of the single solutions M1M, M1A and M1R were compared with the measured mass of solution M1 before. The difference is less than 1‰.

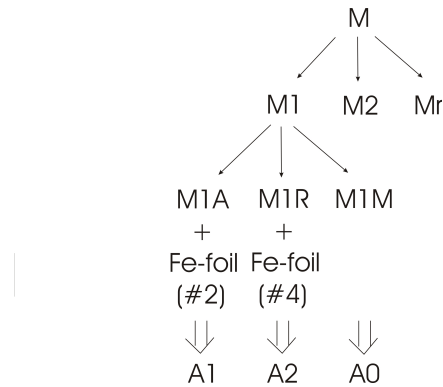


**Figure 6.1:** Schematical view of the performed dilution steps.

### Further Dilution

(M1R) + (Fe-foil #4) → A2;  
 (M1A) + (Fe-foil #2) → A1

Until now, the master solution "M" was not changed in its  $^{55}\text{Fe}/^{56}\text{Fe}$  ratio, but was just split in various partitions (solution "M1M", "M1A", "M1R", "M2", "Mr").

Further dilutions of those partitions by adding (stable) iron chloride lead to three different isotope ratios:

Solution "M1A" was mixed with the dissolved Fe-foil #4 and solution "M1R" ( $\approx 47.4\%$  of M1 solution) was mixed with the dissolved Fe-foil #2. In those dilution steps it is very important to wash the bottle with distilled water to ensure that the whole amount of solution "M1A" is mixed with the stable iron chloride. Table 6.4 shows the results for the produced solutions, including the masses of the solution, the percentage of the master solution, and the mass of the Fe-content.

	$M_{solution}$ [g]	$\pm$	Percentage of Master Solution [%]	$\pm$ [%]	$M_{Fe}$ [g] Fe	$\pm$	$M_{Fe}$ [g] + Fe-foil
M	169.25	0.56	100		9.8616	0.0005	
M1R	80.2813	0.0091	47.43	0.33	4.677	0.015	10.01
M1A	1.33749	0.00071	0.79	0.34	0.07793	0.00026	9.85
M1M	1.38356	0.00071	0.82	0.33	0.08061	0.00027	
M2	85.13145	0.00071	50.30	0.33	4.960	0.016	
Mr	1.13	0.56	0.67	49.33	0.066	0.032	

**Table 6.4:** Mass of solution, and the mass of the Fe-content inside the diluted solutions M1R, M1A, M1M, M2 and Mr.

### 6.3 Results and discussion

The results of the produced isotopic ratios of the dilution series are shown in 6.5.

The  $^{55}\text{Fe}$ -standard with the highest isotopic ratio is the Master Solution A0 with  $(7.35 \pm 0.12) \cdot 10^{-10}$ . It is for sure the most accurate one, compared to A1 and A2, because it was made without any additional dilution steps. The whole amount of the (PTB- $^{55}\text{Fe}$ ) standard solution was directly added to a glass bottle containing the dissolved Fe-foil of well known amount. The assumption, that no losses of this  $^{55}\text{Fe}$ -standard solution occurred, is justified by the multiple washing steps of the ampule, but was then checked by the AMS- measurements.

	$^{55}\text{Fe}/^{56}\text{Fe}$	$\pm$	$\pm$ [rel]	name
M	$7.35 \cdot 10^{-10}$			
M1R	$2.341 \cdot 10^{-10}$	$0.037 \cdot 10^{-10}$	1.57 %	A2
M1A	$5.767 \cdot 10^{-12}$	$0.091 \cdot 10^{-12}$	1.57 %	A1
M1M; M2	$7.35 \cdot 10^{-10}$	$0.12 \cdot 10^{-10}$	1.61 %	A0

**Table 6.5:** Isotopic ratio of the produced  $^{55}\text{Fe}$ - standards A0, A1 and A2. The reference date is 1<sup>st</sup> October 2008 (00:00 CET).

## Part II

# Part II: The neutron capture cross section of $^{54}\text{Fe}(n,\gamma)$



## 7 Neutron irradiations for the $^{54}\text{Fe}(\text{n},\gamma)$ -reaction

The main goal of this thesis is the measurement of the thermal neutron capture cross section on  $^{54}\text{Fe}$  via AMS. Two different reactors allowed neutron irradiations of Fe-samples:

- In March 2008, samples AI08\_FeM, AI08\_Fe2, AI08\_FeA2 and AI08\_FeA4 were irradiated with thermal neutrons at the TRIGA Mark-II reactor at the Vienna Atominstitut (at an irradiation position about 1 m from the reactor core).
- In November 2009, samples BP\_FeM\_Au3 and BP\_54Fe\_Au0 were irradiated with cold neutrons at the Budapest Research Reactor at an irradiation position far away from the reactor core.

All samples except BP\_54Fe\_Au0 were produced from natural Fe-powder (Merck), while BP\_54Fe\_Au0 was produced from enriched  $^{54}\text{Fe}$ -powder (STB) (see its isotopic compositions in table 5.1).

### 7.1 Principle

Equation 7.1 describes the dependence of the neutron capture cross section  $\sigma_{n,\gamma}$  on the number of incident neutrons per area, fluence  $\Phi$ , the number of target atoms  $N_{54\text{Fe}}$ , and the number of produced radionuclides  $N_{55\text{Fe}}$  (see also equation 2.12 in section 2.2.1 for details) (neglecting any decay corrections).

$$\sigma_{n,\gamma} = \frac{1}{\Phi} \frac{N_{55\text{Fe}}}{N_{54\text{Fe}}} \quad (7.1)$$

For the determination of the neutron capture cross section of  $^{54}\text{Fe}$ , the isotopic ratio  $N_{55\text{Fe}}/N_{54\text{Fe}}$  was measured with AMS (see section 3.3) and the neutron fluence  $\Phi$  (see equation 7.2) was determined by means of an activity measurement of Au-foils, which served as fluence monitor and were irradiated simultaneously with the iron samples.

$$\Phi = \frac{1}{\sigma_{n,\gamma} N_{197\text{Au}}} \cdot N_{198\text{Au}} \stackrel{(4.5)}{=} \frac{1}{\sigma_{n,\gamma} N_{197\text{Au}}} \cdot A(t_{\text{irr}E}) \frac{T_{\text{irr}}}{(1 - e^{-\lambda_{\text{Au}} T_{\text{irr}}})} \quad (7.2)$$

The activity  $A(t_{irrE})$  is given in equation 4.11.

In general, gold is used as standard for several neutron energies: it is monoisotopic  $^{197}\text{Au}$  and it has a well-known and high neutron capture cross section. In addition, the radioactive  $^{198}\text{Au}$  ( $t_{1/2} = (2.69517 \pm 0.00021)$  days [Auble, 1983]), which is produced by the neutron capture on  $^{197}\text{Au}$ , emits almost a single  $\gamma$ -ray ( $p_\gamma = 95.6$ ) and is thus, well suited for activity measurements.

As additional fluence monitor, Zr-foils were used. The stable isotopes of gold and zirconium and their natural abundances are listed in table 7.1.

	isotopic composition [%]
$^{197}\text{Au}$	100
$^{90}\text{Zr}$	51.45
$^{91}\text{Zr}$	11.22
$^{92}\text{Zr}$	17.15
$^{94}\text{Zr}$	17.38
$^{96}\text{Zr}$	2.8

**Table 7.1:** Isotopic composition of the stable isotopes of Zr and Au, which were used as fluence monitors.

## 7.2 Neutron irradiation at the TRIGA Mark-II reactor

### 7.2.1 The TRIGA Mark-II reactor

Several samples were irradiated with thermal neutrons produced at the TRIGA Mark-II reactor of the Vienna Atomintitut. The TRIGA Mark-II reactor, which is in operation since the year 1962, is a research reactor of the swimming-pool type and stands for Training, Research, Isotope Production and General Atomic. Its maximum continuous power output of 250 kW (thermal) provides a neutron flux  $\varphi$  of about  $1 \cdot 10^{13}$  n/cm<sup>2</sup>/s in the central irradiation tube and about  $4 \cdot 10^{11}$  n/cm<sup>2</sup>/s at our favoured irradiation position 1 m from the reactor core.

### 7.2.2 Experimental Procedure

Prior to this diploma thesis, in the year 2006, first iron samples were irradiated at the TRIGA Mark-II reactor and in March 2008 another series of irradiations was performed.

Four iron samples were prepared for the irradiations in March 2008: Samples AI08\_FeA2, AI08\_FeA4 and AI08\_Fe2 were Fe-pellets of 10 mm diameter, made out of 500-800 mg Fe-powder of natural composition. The pellets were then sandwiched by Zr-foils, serving as fluence monitors. The fourth sample, AI08\_FeM, was Fe-powder of natural composition filled into an Eppendorf tube (see following section for explanation) and was equipped with two Au-foils (Au11, Au19) and one Zr-foil.

The masses of the Au-foils were in the order of 0.5-2 mg and the masses of the Zr-foils  $\approx$  40-45 mg.

A comparison of the determined values for the neutron fluences, given in table 7.3, is discussed below and compilation of the neutron irradiations is given then in table 7.4.

### 7.2.3 Results and discussion of the neutron fluence

The neutron fluence was determined by activity measurements of  $^{198}\text{Au}$  and  $^{95}\text{Zr}$  with a HPGe detector (see equation 7.2). The parameters needed for these calculations are listed in table 7.2.

	$\sigma_{n,\gamma}$ [barn]	radioactive isotope	$t_{1/2}$ [d]	$E_\gamma$ [keV]	$p_\gamma$ [%]	$\epsilon_\gamma$ [%]
$^{197}\text{Au}$	98.65(9)	$^{198}\text{Au}$	2.69517(21)	411.8	95.6	0.967
$^{94}\text{Zr}$	0.0494(17)	$^{95}\text{Zr}$	64.03	724.2 756.7	44.3 54.4	0.541 0.519

**Table 7.2:** Parameters needed for the activity determination of the isotopes  $^{198}\text{Au}$  and  $^{95}\text{Zr}$ . The thermal neutron capture cross sections are taken from [Mughabghab, 2006] for  $^{197}\text{Au}$  and [Mughabghab *et al.*, 1981] for  $^{94}\text{Zr}$ . The half-lives are taken from [Auble, 1983] for  $^{197}\text{Au}$  and [Burrows, 1993] for  $^{94}\text{Zr}$ . The uncertainty of the detector efficiency  $\epsilon_\gamma$  is 2%.

#### Intensity distribution of the neutron flux

To check, whether the neutron flux is homogeneous inside the irradiation tube,  $\approx$  1 m from the core of the TRIGA Mark-II reactor, three and five Au-foils were stucked on two "Eppendorf tubes" (one Au-foil was inside): A cone-shaped "Eppendorf tube" is  $\approx$  4 cm high, has a volume of  $\approx$  15 ml and a diameter of  $\approx$  1 cm. Both Eppendorf tubes were irradiated for  $\approx$  1 minute and afterwards, the activities of all eight Au-foils were measured with the HPGe detector at two different detector positions, which differ only in the sample-detector distance ( $\approx$  4 cm for position 4, and  $\approx$  5 cm for position 5). The results obtained at position 5 are systematically 1-2 % higher, but are within the uncertainty of the detector efficiency ( $\approx$  2%).

The standard deviation of a single neutron fluence measurement (at  $1\sigma$ ) was 4-5 % for the Au-foils of a single Eppendorf tube and 7-8% for all 8 Au-foils. The standard deviation of the mean neutron fluence for an Eppendorf, was about 2.5 %. The standard deviation between the mean neutron fluence of the first and the second Eppendorf was about 8%.

This test-series showed, that the neutron fluence is not as homogeneous as it was assumed. The best way to attribute for this effect is to use neutron fluence monitors at several positions of the sample. In this regard, a defined form of the samples, e.g. pellets made out of powder, is favourable compared to Eppendorf tubes, filled with Fe-powder.

**Fluence monitors**

The fluence monitors used for the Fe-samples were zirconium and gold. The latter one allows more accurate measurements, due to the more precise neutron capture cross section value for  $^{197}\text{Au}$  ( $\pm 0.9\%$ , compared to  $\pm 3.44\%$  for  $^{95}\text{Zr}$ , see table 7.2). Even for the activity determination with the HPGe diode, Au-foils are favourable because  $^{198}\text{Au}$  emits almost a single  $\gamma$ -ray with an emission probability of 95.6%, where coincidence summing corrections can be neglected (see also section A.1.1). One disadvantage of using Au-foils is its high neutron capture cross section value, which results after an irradiation time of one minute in activities of about 30 kBq for 1 mg Au-foils, compared to 10 Bq for  $\approx 50$  mg Zr-foils.

	$\Phi$ [ $\text{cm}^{-2}$ ]	$\pm s_{total}$ [%]	$s_{stat}$ [%]	$s_{syst}$ [%]	$s_m$ [%]	$s_{\epsilon_\gamma}$ [%]	$s_{p_\gamma}$ [%]	$s_\sigma$ [%]
AI08_FeM:								
Au11_pos4	$2.09 \cdot 10^{14}$	2.3	0.2	2.3	1.1	2.0		0.1
_pos5	$2.14 \cdot 10^{14}$	2.3	0.3	2.3	1.1	2.0		0.1
Au19_pos4	$2.10 \cdot 10^{14}$	2.8	0.3	2.7	1.9	2.0		0.1
_pos5	$2.16 \cdot 10^{14}$	2.8	0.4	2.7	1.9	2.0		0.1
Zr104_pos4_724keV	$2.29 \cdot 10^{14}$	5.3	0.9	4.0	0.1	2.0	0.5	3.4
_757keV	$2.26 \cdot 10^{14}$	5.3	0.8	4.0	0.1	2.0	0.4	3.4
AI08_Fe2:								
Zr50_pos4_724keV	$2.38 \cdot 10^{14}$	5.3	0.9	4.0	0.1	2.0	0.5	3.4
_757keV	$2.43 \cdot 10^{14}$	5.3	0.8	4.0	0.1	2.0	0.4	3.4
Zr21_pos4_724keV	$2.43 \cdot 10^{14}$	5.3	0.9	4.0	0.1	2.0	0.5	3.4
_757keV	$2.41 \cdot 10^{14}$	5.3	0.8	4.0	0.1	2.0	0.4	3.4
AI08_FeA2:								
Zr105_pos4_724keV	$4.99 \cdot 10^{13}$	5.3	1.1	4.0	0.1	2.0	0.5	3.4
_757keV	$5.06 \cdot 10^{13}$	5.3	1.0	4.0	0.1	2.0	0.4	3.4
Zr147_pos4_724keV	$4.87 \cdot 10^{13}$	5.4	1.2	4.0	0.1	2.0	0.5	3.4
_757keV	$4.83 \cdot 10^{13}$	5.3	1.1	4.0	0.1	2.0	0.4	3.4
AI08_FeA4:								
Zr90_pos4_724keV	$2.82 \cdot 10^{13}$	5.4	1.2	4.0	0.1	2.0	0.5	3.4
_757keV	$2.94 \cdot 10^{13}$	5.3	1.1	4.0	0.1	2.0	0.4	3.4
Zr38_pos4_724keV	$2.91 \cdot 10^{13}$	5.4	1.2	4.0	0.1	2.0	0.5	3.4
_757keV	$2.80 \cdot 10^{13}$	5.3	1.1	4.0	0.1	2.0	0.4	3.4

**Table 7.3:** Comparison of the neutron fluence data, which were obtained from different fluence monitors (gold and zirconium foils) for each AI08 sample. Details about the irradiation data are given in table 7.7. Pos 4 and pos 5 denotes the positions of samples for the activity measurement.

The results for the neutron fluences for the irradiated Fe-samples, deduced from the different fluence monitors, are listed in table 7.3 and discussed below:

The standard deviation of the neutron fluences, which were obtained from Zr-foils was about 1 %. The values found for the neutron fluence from the Zr-foil and from the Au-foils, however deviate up to 4 %. For samples AI08\_Fe2, AI08\_FeA4 and AI08\_FeA2, the neutron fluence could only be determined with the Zr-foils and due to resulting higher uncertainty they serve as test samples. The neutron fluence for sample AI08\_FeM was determined with the Au-foils.

For the calculation of the mean neutron fluence and its uncertainty, correlations of different uncertainties were taken into account by using variance-covariance matrices in the generalized error-propagation law and are described by [Winkler, 1993] and [Winkler, 1998]. The final results for the neutron fluence values, which were used for further calculations, are given in table 7.4.

sample	Fluence Monitor	$T_{irr}[min]$	$t_{irr,E}$	$\Phi [n/cm^2]$	$\pm s_{\Phi} [\%]$
AI08_FeM	Au11, Au19	10	26.03.2008 10:05	$2.12 \cdot 10^{14}$	1.5
AI08_Fe2	Zr50, Zr21	10	26.03.2008 10:05	$2.41 \cdot 10^{14}$	4.0
AI08_FeA2	Zr105, Zr147	2	26.03.2008 09:41	$4.94 \cdot 10^{13}$	4.0
AI08_FeA4	Zr90, Zr38	1.22	26.03.2008 10:21	$2.85 \cdot 10^{13}$	4.0

**Table 7.4:** Overview of the irradiated samples at the TRIGA Mark-II reactor of the Vienna Atominstytut.

## 7.3 Neutron irradiation at the BRR

### 7.3.1 The Budapest Research Reactor (BRR)

In November 2008 two iron samples were irradiated with cold neutrons at the Budapest Research Reactor BRR. The tank-type reactor, which is moderated and cooled by light water, is in operation since the year 1959. Since then, it was upgraded twice: in 1967, from the initial thermal power of 2 MW to 5 MW and in the year 1986 to a thermal power of 10 MW. The maximum thermal neutron flux density in the core is about  $2.3 \cdot 10^{14} n/cm^2/s$ , but the irradiation of the iron samples was performed at the NIPS (neutron induced prompt gamma-ray spectrometry) station in the CNS (cold neutron source) measuring hall, adjacent to the reactor hall (see figure 7.1). The neutrons from the core are guided to the NIPS station via scattering along the so called neutron guide tube (inside made out of 25 x 100 mm<sup>2</sup> section float glass optical elements, which are coated with <sup>58</sup>Ni to favour the scattering process). The neutrons are scattered if their incident angle is smaller than the critical angle, which increases with decreasing velocity of the neutrons. In this regard, neutrons of lower energies are favoured and the NIPS station is far enough away from the core center to offer cold neutrons (< meV) for the irradiations. The neutron flux, which decreases with 1/distance in the evacuated neutron guide, is about  $4.5 \cdot 10^7 n/cm^2/s$  at the NIPS station (see <http://www.efnudat.eu/docs/iki.pdf> for details).

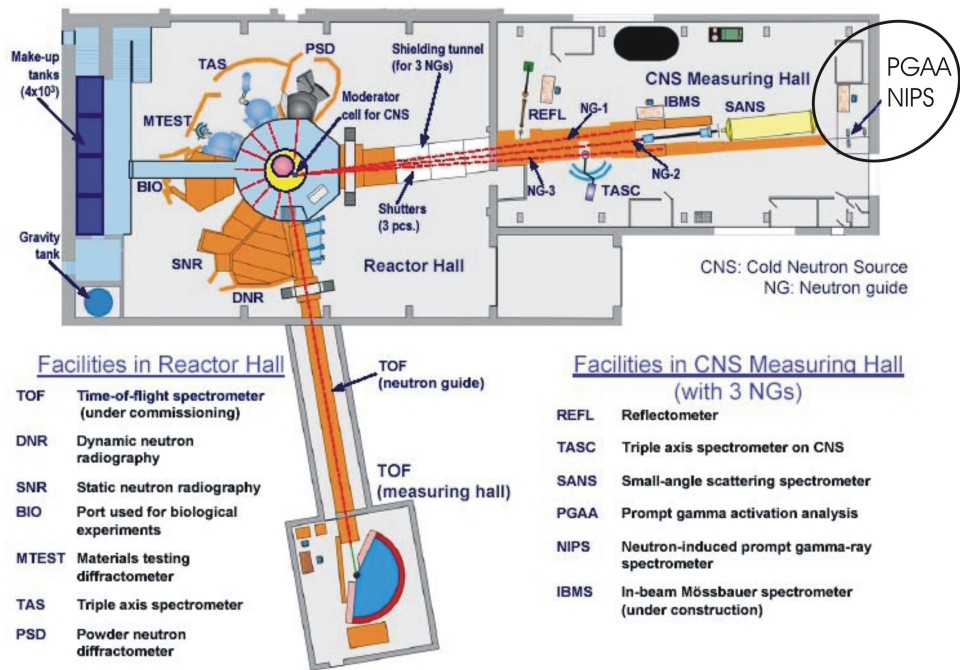


**Figure 7.1:** Layout of the horizontal neutron beam facilities at the BRR, taken from the webpage <http://www.kfki.hu/brr/indexen.htm>.

### 7.3.2 Experimental set-up

The experimental area is installed at the end of the neutron guide and is mainly used for prompt gamma activation analysis (PGAA), and neutron induced prompt gamma ray spectrometry (NIPS). The neutron beam at the NIPS station, where the irradiations of the iron samples took place, is collimated to a size of  $2 \times 2 \text{ cm}^2$ . The intensity of the neutrons depends strongly on the position and thus, the isotopic ratio  $^{55}\text{Fe}/\text{Fe}$  will not be homogeneously distributed over the sample area. Figure 7.2 shows a scheme of the irradiation position at the NIPS station.

### 7.3.3 Experimental procedure

Two iron samples, pellets of 6 mm in diameter, were prepared for the irradiations in November 2008 at IKI: BP\_FeM\_Au3 and BP\_54Fe\_Au0. As fluence monitors only gold was used: Au-powder homogeneously mixed with the Fe powder and 2 Au-foils at the front- and backside of sample BP\_FeM\_Au3. Sample BP\_FeM\_Au3 was made of Fe-powder of natural composition (Merck) and sample BP\_54Fe\_Au0 was made of Fe-powder, enriched in  $^{54}\text{Fe}$  (STB Isotope Germany GmbH) (see table 5.1 for details about the sample material).

#### Sample preparation

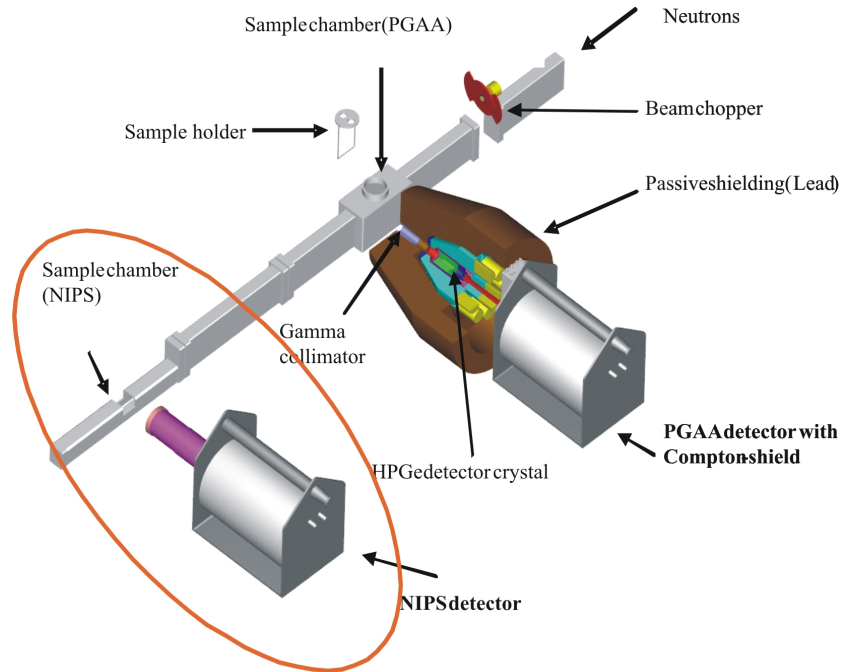


**Figure 7.2:** Fe samples were irradiated at the position "sample chamber (NIPS)" (left side), schematic view taken from [Szentmiklosi & Belgya, 2007].

For the mixture of the Fe-powder with the Au-powder, the amount of both materials were weighted each with a Sartorius scale (uncertainty  $< 1 \%$ ) and then pestled carefully in a mortar to homogenise the powder. Finally, out of this powder mixture, a pellet of 6 mm diameter was produced with a sample press (see figure 5.1), which was fabricated at the VERA-laboratory.

The Au-foils were of exactly the same size (6mm in diameter) as the pellets because they were punched with the same stamp. For the irradiation, the front Au-foil  $Au_{Front}$ , the sample pellet and the back Au-foil  $Au_{Back}$  formed a stack and were put into an aluminum holder of 6 mm diameter. This method ensured a determination of the neutron fluence, representative for the whole sample area of all samples due to exactly the same geometry.

The masses of the gold and iron contents of the samples, and those of the Au-foils are listed in table 7.5. The scheme in figure 7.3 shows sample BP\_54Fe\_Au0, which was additionally fixed with a small plastic ring, and the stack of sample BP\_FeM\_Au3 with the Au-foils in the aluminum holder. Each assembly was then shrink-wrapped in a teflon foil to be finally mounted on a sample holder with thin teflon strings at the NIPS irradiation position. An overview of the irradiations is given in table 7.7 and includes the values of the neutron fluences.

sample	m(Fe) [mg]	m(Au) [mg]	m(Au <sub>Back</sub> ) [mg]	m(Au <sub>Front</sub> ) [mg]
BP_FeM_Au3	55.650(2)	22.248(1)	14.92(1)	15.00(1)
BP_54Fe_Au0	45.182(2)	20.733(1)		

**Table 7.5:** Masses of the samples, which were used for the irradiations at the BRR. Au corresponds to the Au-powder mixed into the iron, whereas AuFront and AuBack correspond to the Au-foils, which were placed at the front and back side of the iron pellet.

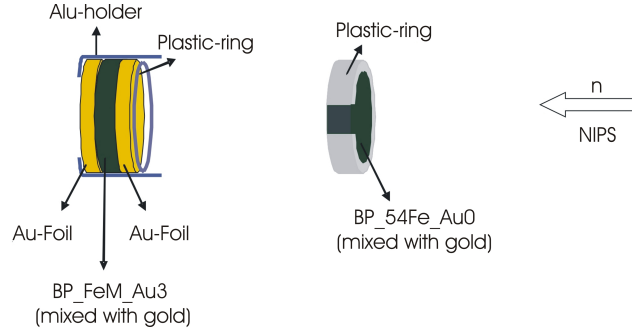


**Figure 7.3:** Scheme of the irradiation assembly.

### 7.3.4 Results and discussion of the neutron fluence

The neutron fluence was determined by an activity measurement with the HPGe detector at the Vienna Atominstiut three weeks after the irradiations in Budapest and the results are listed in table 7.6:

The front Au-foil received more neutrons compared to the back Au-foil. The arithmetic mean of those neutron fluences agrees with the value obtained from the Au-powder inside the pellet. This shows, that both methods are working for the determination of the neutron fluence. Each fluence monitor was remeasured a few days later. The values are reproducible with an uncertainty of 1-2 %. As weights for the weighted mean, only the statistical uncertainties  $s_{stat}$  were taken. The uncertainty of the weighted mean was always calculated as the maximum of the inner and outer weighted uncertainty (see equations B.6 and B.7 in section B.1.3). The systematic uncertainty  $s_{syst}$  is the square root of the sum of the variances of the masses, the dominating efficiency and the cross section value for Au. For the final value of the neutron fluence according to sample BP\_FeM\_Au3, the weighted mean of the three activity measurements was taken. The final values of the neutron fluences are shown in table 7.7.

## 7.4 Overview of neutron irradiated samples

Fluence Monitor	$\Phi$ [ $cm^{-2}$ ]	$s_{stat}$ [%]	$s_{syst}$ [%]	$s_{tot}$ [%]
<b>BP_FeM_Au3:</b>				
FeM_Au3_tab (1 <sup>st</sup> meas.)	$1.04 \cdot 10^{13}$	0.51	2.00	
FeM_Au3_tab (2 <sup>nd</sup> meas.)	$1.04 \cdot 10^{13}$	0.76	2.00	
<b>weighted mean</b>	<b><math>1.01 \cdot 10^{13}</math></b>	<b>0.43</b>	<b>2.00</b>	<b>2.05</b>
$Au_{Front}$ (1 <sup>st</sup> meas.)	$1.15 \cdot 10^{13}$	0.54	2.01	
$Au_{Front}$ (2 <sup>nd</sup> meas.)	$1.10 \cdot 10^{13}$	0.82	2.01	
$Au_{Back}$ (1 <sup>st</sup> meas.)	$9.43 \cdot 10^{12}$	0.59	2.01	
$Au_{Back}$ (2 <sup>nd</sup> meas.)	$9.48 \cdot 10^{12}$	0.85	2.01	
weighted mean $Au_{Front}$	$1.13 \cdot 10^{13}$	2.00	2.01	2.83
weighted mean $Au_{Back}$	$9.45 \cdot 10^{12}$	0.48	2.01	2.06
<b>Mean <math>Au_{Back}</math>-<math>Au_{Front}</math></b>	<b><math>1.04 \cdot 10^{13}</math></b>	<b>1.46</b>	<b>2.01</b>	<b>2.48</b>
<b>BP_54Fe_Au0:</b>				
54Fe_Au0 (1 <sup>st</sup> meas.)	$3.86 \cdot 10^{12}$	0.59	2.00	
54Fe_Au0 (2 <sup>nd</sup> meas.)	$3.97 \cdot 10^{12}$	0.94	2.00	
54Fe_Au0 (3 <sup>rd</sup> meas.)	$3.99 \cdot 10^{12}$	0.85	2.00	
<b>weighted mean</b>	<b><math>3.92 \cdot 10^{12}</math></b>	<b>1.09</b>	<b>2.00</b>	<b>2.28</b>

**Table 7.6:** Comparison of the results of the neutron fluence measurements for the irradiations at the BRR.

## 7.4 Overview of neutron irradiated samples

sample	Fluence Monitor	$T_{irr}[min]$	$t_{irr,E}$	$\Phi$ [n/cm <sup>2</sup> ]	$\pm s_{\Phi}$ [%]
AI06_Fe1*	Zr37, Au_3	1	23.02.2006 14:36:16	$2.41 \cdot 10^{13}$	2.2
AI06_Fe2*	Zr17, Zr34	10	23.02.2006 14:11:30	$2.41 \cdot 10^{14}$	4.3
AI06_Fe3*	Zr14	60	23.02.2006 13:58:45	$1.49 \cdot 10^{15}$	4.5
AI08_FeM	Au11, Au19	10	26.03.2008 10:05	$2.12 \cdot 10^{14}$	1.5
AI08_Fe2	Zr50, Zr21	10	26.03.2008 10:05	$2.41 \cdot 10^{14}$	4.0
AI08_FeA2	Zr105, Zr147	2	26.03.2008 09:41	$4.94 \cdot 10^{13}$	4.0
AI08_FeA4	Zr90, Zr38	1.22	26.03.2008 10:21	$2.85 \cdot 10^{13}$	4.0
BP_FeM_Au3	Au3, AuFront, AuBack	5449	10.11.2008 14:00	$1.04 \cdot 10^{13}$	2.1
BP_54Fe_Au0	Au0	1481	06.11.2008 14:00	$3.91 \cdot 10^{12}$	2.3

**Table 7.7:** Overview of the irradiated samples at the TRIGA Mark-II reactor of the Vienna Atominstiut and at the Budapest Research Reactor (BRR). \*AI06-samples were already available and were produced prior to this work.



## 8 AMS Measurements of $^{55}\text{Fe}$ @ VERA

In the year 1990, first test AMS measurements at the 14 MV tandem accelerator at Munich were performed for the isotope  $^{55}\text{Fe}$  by [Korschinek *et al.*, 1990]. It was shown, that the only isobar  $^{55}\text{Mn}^-$  is strongly suppressed and thus, the measurement of very low  $^{55}\text{Fe}$  concentrations is possible with AMS. The neighbouring isotopes  $^{54}\text{Fe}$  and  $^{56}\text{Fe}$  were effectively suppressed by the use of a Wien filter and a TOF system with an ionization chamber. The sensitivity for  $^{55}\text{Fe}/\text{Fe}$  was estimated to about  $8 \cdot 10^{-13}$ .

[Wallner *et al.*, 2007a] demonstrated the astrophysical interest in the production of  $^{55}\text{Fe}$  via neutron-capture on  $^{54}\text{Fe}$ . An upper detection limit of  $^{55}\text{Fe}/^{56}\text{Fe}$  of  $2 \cdot 10^{-15}$  was determined at the +3 MV Vienna Environmental Research Accelerator.

The technique of accelerator mass spectrometry (AMS) was already discussed in section 3.3. In the course of this thesis, 5 beam-times were carried out with 3 different detection setups. Iron samples, which were measured in this period, were irradiated at 6 different facilities, offering 5 different neutron energies. An accurate AMS measurement of the isotopic ratio  $^{55}\text{Fe}/\text{Fe}$  of all these samples requires a well-known  $^{55}\text{Fe}$ -AMS "standard" as reference material (see part I). The measurement of the thermal neutron capture cross section was the main goal of this thesis. In this regard, three beam-times are of main interest: the one performed in November 2008, January 2009 and March 2009. Table 8.1 shows an overview of those beam-times and includes details about the detection setups (see section 3.3.3), reference materials, the scaling factor (see equation 8.5), the measured sample materials and the corresponding  $^{55}\text{Fe}/\text{Fe}$  ratio of the blanks (see section 8.3.2).

Prior to a detailed discussion about those AMS - measurements, it is necessary to describe the different iron sample materials, their preparation, the tuning procedure of  $^{55}\text{Fe}$  and the evaluation of the measured data.

## 8.1 Overview of the sample material

The amount of a sample needed for the AMS - measurement of a sputter cathode lies in the range of a few mg. For each sample material, a blank material is needed to quantify the background signals. Both materials undergo the same chemical sample preparation. The important difference is, that the blank material was not irradiated and therefore, contains the radioactive isotope  $^{55}\text{Fe}$  only by its natural concentration, which is assumed to be negligible. The measured isotopic ratios of these blanks define the background level and specifies the limit of detection for each AMS - measurement.

Four sample materials, which differ in the chemical and isotopic composition, were used and are abbreviated by Fe, 54Fe, 54Fe<sub>2</sub>O<sub>3</sub>, Fe<sub>2</sub>O<sub>3</sub>-GF:

- **Fe-powder of natural composition** → **Fe**

Comment to the nomenclature: "FeA" refers to iron powder from Alfa Aesar GmbH & Co KG, and "FeM", "Fe" to iron powder from Merck KGaA.

7 samples were irradiated with thermal neutrons at the TRIGA Mark-II reactor of the Atominstitut of the Vienna Universities:

AI06\_Fe1, AI06\_Fe2, AI06\_Fe3, AI08\_FeM, AI08\_Fe2, AI08\_FeA2, AI08\_FeA4.

1 sample was irradiated with cold neutrons at the Budapest Research Reactor:  
BP\_FeM\_Au3.

1 sample was irradiated with protons at VERA:  
pg\_Fe9mm

- **Fe-powder enriched in  $^{54}\text{Fe}$**  → **54Fe**

The material was ordered from STB Isotope Germany GmbH (see table 5.1).

1 pellet was used for the proton irradiation at VERA:  
pg\_54Fe6mm.

1 pellet was used for the cold neutron irradiation at the Budapest Research Reactor:

BP\_54Fe\_Au0.

- **Fe-foil enriched in  $^{54}\text{Fe}$**  → **54Fe<sub>2</sub>O<sub>3</sub>**

1 foil, ordered at STB, was irradiated with protons at VERA:  
pg\_54FeFoil  $\equiv$  pg\_54Fe<sub>2</sub>O<sub>3</sub>

- **Fe-foil of natural composition** → **Fe<sub>2</sub>O<sub>3</sub>-GF**

4 foils, ordered at Goodfellows, were used for the dilution series to produce the  $^{55}\text{Fe}$ - AMS reference material: A0, A1, A2.

A short summary, where to find which information:

Table 7.7 contains informations about the neutron irradiations (including neutron fluences) and table 5.2 about the proton irradiations. The isotopic composition and molar masses of the irradiated samples can be found in table 5.1. Table 5.9 contains the results of the isotopic ratios of the pg\_samples and table 6.5 the ones of the standards from the dilution series.

All powder samples (except AI08\_FeM) were pressed to a pellet before the irradiation and had to be pestled again after the irradiations, to produce powder form for the AMS measurement and to ensure a well established homogenized material.

The Fe-foils were diluted in hydrochloric acid. The iron chloride resulted as product, was then heated and evaporated at a temperature of about 200°C. Some distilled water was added and the iron hydroxide was then filled into a 50 ml centrifuge tube. Afterwards, ammonia was added into this centrifuge tube and Fe precipitated. By centrifugation, the iron hydroxide is separated from the solution. This procedure (centrifugation and washing) was repeated several times. In the last step, the iron hydroxide is dried at a temperature of about 100°C and then combusted at about 600° to form iron oxide, which is then pestled to iron oxide powder. The chemical composition is Fe<sub>2</sub>O<sub>3</sub>. Some blank materials experienced the same chemical process, some were measured via AMS in their original foil form.

Each sample is pressed into a small sample holder (acts as cathode) and 40 cathodes were then loaded into the sample wheel (see description of the ion source in section 3.3.2). Both, the cathodes and the wheel, are made of copper to avoid mass interferences, which would be present in case of aluminum holders with  $m(^{27}\text{Al}_2) = \text{Mass } 54 = m(^{54}\text{Fe})$ .

## 8.2 Tuning procedure of $^{55}\text{Fe}$

Figure 8.1 shows a schematical view of VERA, including the names of the important tuning components. Both isotopes  $^{54}\text{Fe}$ ,  $^{56}\text{Fe}$  are measured as  $\text{Fe}^-$  at the low energy side in offset Faraday cups (MFC02-1, MFC02-2) and as  $\text{Fe}^{3+}$  at the high energy side in offset cups (MFC04-2, MFC04-3), as well.

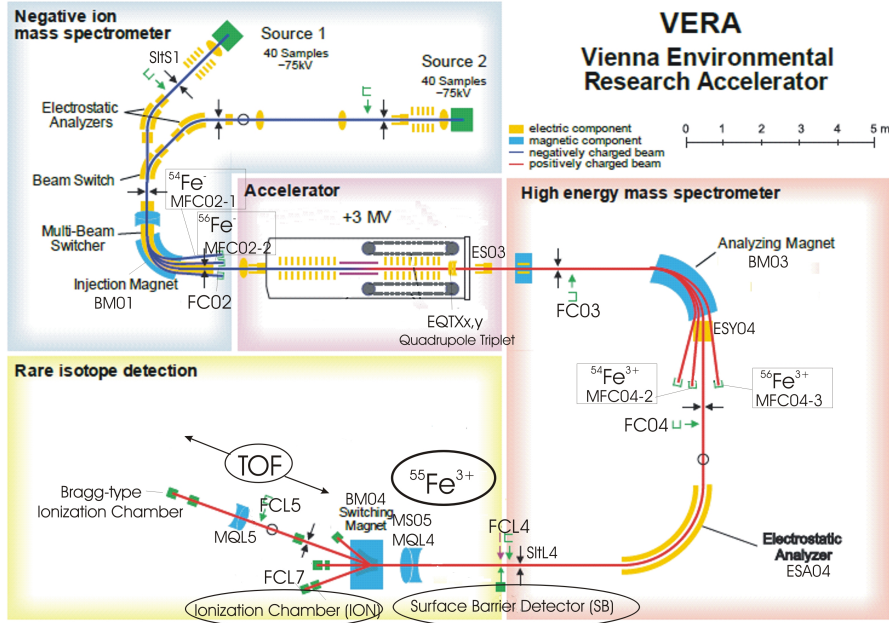


**Figure 8.1:** Schematical view of VERA, based on a figure from Vockenhuber and Michlmayr. The Faraday cups used for the current measurement of  $^{54}\text{Fe}$ ,  $^{56}\text{Fe}$  and detectors used for measurements of  $^{54}\text{Fe}$  are drawn into the scheme.

The tuning procedure was performed in the following order:

- **Switching on the source**
- **Tuning of the low energy side with  $^{56}\text{Fe}^-$**   
For tuning of VERA,  $\text{Fe}^-$  is extracted from a blank cathode and accelerated to an energy of about 75 keV at the low energy side. Due to the few  $^{55}\text{Fe}$ -atoms in the Fe-sample, it is necessary to tune the components of VERA with the stable  $^{56}\text{Fe}$ -beam by maximising the current in the Faraday Cups. The current measured with the Faraday Cup FC02 on the low energy side is in the range of hundred nA. The magnetic field of the injection magnet BM01 was about  $\approx 6570$  G and the applied MBSreg3 voltage  $\approx 7.1$  kV.
- **Tuning of the high energy side with  $^{56}\text{Fe}^{3+}$**   
The stripper gas pressure was set to  $5.1 \mu\text{m}$  barometric column, where the

charge state yield has a maximum. The terminal voltage of the tandem accelerator was between 2.7 and 3.1 MV. The magnetic field of magnet BM03 was set to 6570 G and the  $3^+$  charge state was selected, because it is the charge state of highest yield (see [Wallner *et al.*, 2007b]). The transmission, which is the ratio between the iron current on the high energy side and the iron current on the low energy side, is represented by  $^{56}\text{Fe}^{3+}/^{56}\text{Fe}^-$  measured in MFC04-3, respectively MFC02-2 and is  $> 20\%$ .

After several scans of components on the low energy side, a script batch called "automax" (see [Steier *et al.*, 2000]) optimized, first, the components on the low energy side and then on the high energy side by maximising the iron current in Faraday cup FC04. Then, the terminal voltage, the quadrupole triplet EQTX-x/y, the steerer ES03, ESY04 and the electrostatic analyzer ESA04 were optimized with Faraday Cup FCL4. The slits SltL4 on the beam line L4 were closed to an aperture of  $\pm 2$  mm (see figure 8.1).

If the current in Faraday Cup FC04 and FCL4 was found the same, the tuning procedure was okay and was continued till the detector position. In figure 8.1, three different detector positions are shown and each one requires a different tuning procedure. However, in each case one has to attenuate the  $^{56}\text{Fe}^{3+}$ -beam by a factor of  $10^7$ , because the maximal count rate for the detectors lies in the range of  $10^3 - 10^5$  counts per second and the number of  $^{56}\text{Fe}^{3+}$ -atoms of a 10-nA- $^{56}\text{Fe}^{3+}$ -beam is about  $2 \cdot 10^{10}$  atoms per second. The attenuation of the  $^{56}\text{Fe}$ -beam is done by narrowing slits SltS1 and by means of an attenuator, both located right after the preacceleration section of the ion beam.

- **Tuning of the attenuated  $^{56}\text{Fe}^{3+}$ -beam to the surface barrier detector**  
The attenuated  $^{56}\text{Fe}^{3+}$ -beam is now tuned to maximise the count rate in the surface barrier detector (see 3.3.3). Tuning includes mainly the components on the high energy side: terminal voltage, ESY04, ESA04, EQTX-x/y and ES03-x/y.
- **Tuning of the  $^{56}\text{Fe}^{3+}$ -beam to the ionization chamber**  
The  $^{56}\text{Fe}^{3+}$ -beam is tuned to the Faraday cup FCL7, located right after the ionization chamber. Then, it is attenuated and guided through a 3 mm open aperture to the ionization chamber at the  $-20^\circ$  beamline (see 3.3.3). The magnetic field of the magnet BM04 is about -8900 G. Following components are optimized by an automax tuning: ESA04, ESY04, MQL4-x/y, MS05-x/y, ES03-x/y and EQTX-x/y. The pressure of the ionization chamber was  $\approx 50 - 55$  mbar.
- **Tuning of the  $^{56}\text{Fe}^{3+}$ -beam to the Time-Of-Flight (TOF) detector**  
Before the attenuation of the beam, it is possible to use Faraday Cup FCL5 for the next tuning step. The start foil of the TOF-detector is retracted and the magnet BM04 is set to about +9100 G. Afterwards, an attenuated  $^{56}\text{Fe}^{3+}$ -beam is guided to the Bragg-type ionization chamber, situated at the end of

the Time-Of-Flight (TOF) section at the  $+20^\circ$  beamline. It is also possible to use only the Bragg detector by retracting both, the start and the stop foil. The automax is maximising the count rate of the Bragg detector by adjusting following components: ESA04, ESY04, MQL4-x/y, MS05-x/y, MQL5-x/y, ES03-x/y and EQTX-x/y.

Via coincidence measurements between the start foil, the stop foil and the Bragg detector, the transmission of the  $^{56}\text{Fe}^{3+}$ -beam through those TOF-components is checked.  $\approx 70\%$  of the detected  $^{56}\text{Fe}^{3+}$  atoms at the Start foil are also detected at the Stop foil (Start & Stop in coincidence) and  $\approx 60\%$  in the Bragg detector (Start & Bragg in coincidence). If all three detectors are in coincidence,  $\approx 50\%$  of the incident atoms are detected.

- **Scaling the  $^{56}\text{Fe}^{3+}$ -beam to  $^{55}\text{Fe}^{3+}$**

Finally, the isotope of interest,  $^{55}\text{Fe}^{3+}$ , is injected into the tandem accelerator by scaling the MBS voltage of register 3 (see paragraph 3.3.2) from 7.1 kV to 8.6 kV (magnetic rigidity of  $\text{ME}/q^2$  is kept constant). Following voltage values of the different registers of the Multi Beam Switcher were set for the measurement using the TOF beam-line (during the beam-time in January):

reg2:  $U_{MBS,reg2} \approx 1.7 \text{ kV} \rightarrow ^{56}\text{Fe}^-$   
reg1:  $U_{MBS,reg1} \approx 9.9 \text{ kV} \rightarrow ^{54}\text{Fe}^{3+}$   
reg0:  $U_{MBS,reg0} \approx 7.2 \text{ kV} \rightarrow ^{56}\text{Fe}^{3+}$   
reg3:  $U_{MBS,reg3} \approx 8.6 \text{ kV} \rightarrow ^{55}\text{Fe}^{3+}$

After the successful tuning, the  $^{55}\text{Fe}$ -AMS measurement was started.

## 8.3 The evaluation of acquired data

When the measurement is started, the cathodes in the sample wheel can be measured sequentially. A **run** corresponds to the measurement of a single cathode and each run was divided into 1000 cycles. The advantage is, that each **cycle** acquires data in fast switching mode during about 0.2 s (contains information of the currents and the  $^{55}\text{Fe}$  countrate) and is then evaluated separately. If the measured current or the transmission changes significantly within this short time intervall, the cylce is rejected. Sometimes it is even necessary to reject a whole run.

### 8.3.1 Measured isotopic ratio

For each run  $i$ , the isotopic ratios  $\left(\frac{N_{55,true}}{N_{56}}\right)_i$  and  $\left(\frac{N_{55,true}}{N_{54}}\right)_i$  are calculated.

The counted rate of  $^{56}\text{Fe}$ -atoms  $N_{56}/T_{real}$  is measured for each cycle as current  $I_i$  by Faraday cup MFC04-3, and was determined for each run with equation 8.1:

$$\frac{N_{56,i}}{T_{real}} = \frac{I_i}{e \cdot q} \quad (8.1)$$

$T_{real}$  ... measuring time of the detector of 1 run [s]  
 $e$  ... electrical charge [J]  
 $q$  ... selected charge state of the ions

The number of  $^{55}\text{Fe}$ -atoms,  $N_{55}$ , was counted with the detector by setting the corresponding region of interest in the acquired spectrum, and by correcting the number of counts for the deadtime of the used detector the count-rate was calculated. Each cathode was measured during  $r$  runs and its isotopic ratio was calculated by the arithmetic mean over the runs (see equation 8.2).

$$\left\langle \frac{N_{55}}{N_{56}} \right\rangle_{cat} = \frac{1}{r} \sum_i^r \left( \frac{N_{55,true}/T_{real}}{N_{56}/T_{real}} \right)_i \quad (8.2)$$

$N_{55,true}$  ... dead-time corrected number of counts, according to  $N_{55}/(1 - N_{all} \cdot \tau/T_{real})$   
 (see derivation of equation 4.9)

The statistical uncertainty of  $\left\langle \frac{N_{55}}{N_{56}} \right\rangle_{cat}$  is derived from the total number of counts:

$$s_{stat} \left( \left\langle \frac{N_{55}}{N_{56}} \right\rangle_{cat} \right) = \left\langle \frac{N_{55}}{N_{56}} \right\rangle_{cat} \cdot \frac{1}{\sqrt{\sum_i^r (N_{55})_i}} \quad (8.3)$$

For further calculations, the maximum between the statistical uncertainty and the standard deviation of the mean over the runs is taken for the uncertainty of the mean isotopic ratio of one cathode:  $s\left(\left\langle \frac{N_{55}}{N_{56}} \right\rangle_{cat}\right)$ .

### 8.3.2 Blank Correction

The Fe-blanks provide a very small  $^{55}\text{Fe}$  count-rate and thus, in the case of the blanks, first, the sum of the  $^{55}\text{Fe}$  count-rate measured during all runs was taken and then divided by the stable  $^{56}\text{Fe}$  count-rate, see equation 8.4. For the right treatment of uncertainties in the case of small signals, Feldman-Cousins limit setting was used [Feldman & Cousins, 1998].

$$\left(\frac{N_{55}/T_{real}}{N_{56}}/T_{real}\right)_{blk,cat} = \frac{\Sigma N_{55,true}}{\Sigma N_{56}} \quad (8.4)$$

Finally, the blank correction factor  $b_{55/56}^{rel}$  was calculated as arithmetic mean of  $\left(\frac{N_{55}}{N_{56}}\right)_{blk,cat}$  over the blank cathodes. If for all blank cathodes zero counts were measured, upper limits were used.

All isotopic ratios  $\left\langle\frac{N_{55}}{N_{56}}\right\rangle_{cat}$  of the sample cathodes are then corrected by subtracting the background value  $b_{55/56}^{rel}$ . Each blank material defines the background value for the specific sample material and was thus, treated individually for each sample material.

### 8.3.3 Determination of the scaling factor $f_{std}$

The mean scaling factor  $f_{std}$  is measured from cathodes, which contain the reference material of known isotopic ratio  $\left(\frac{N_{55}}{N_{56}}\right)_{nom}$ . Once known, all measured, blank-corrected isotopic ratios of the samples are corrected by  $f_{std}$  to derive absolute values of the isotopic ratios.

First, the scaling factor  $(f_{std})_{cat}$  is determined from the cathodes, which contain reference material:

$$(f_{std})_{cat} = \frac{\left\langle\frac{N_{55}}{N_{56}}\right\rangle_{cat} - b_{55/56}^{rel}}{\left(\frac{N_{55}}{N_{56}}\right)_{nom}} \quad (8.5)$$

$$(df_{stat})_{cat} = \frac{\sqrt{s\left(\left\langle\frac{N_{55}}{N_{56}}\right\rangle_{cat}\right)^2 + s\left(b_{55/56}^{rel}\right)^2}}{\left(\frac{N_{55}}{N_{56}}\right)_{nom}} \quad (8.6)$$

$$(df_{syst})_{cat} = (f_{std})_{cat} \cdot \frac{s\left(\left(\frac{N_{55}}{N_{56}}\right)_{nom}\right)}{\left(\frac{N_{55}}{N_{56}}\right)_{nom}} \quad (8.7)$$

Then, the **mean scaling factor**,  $f_{std}$ , was calculated as the weighted mean (equation B.5) over the cathodes. Only the statistical uncertainties of the AMS measurement  $(df_{stat})_{cat}$  (equation 8.6) contributed to the weight and the systematical uncertainty  $(df_{syst})_{cat}$  (equation 8.7) will be added at the end because it is the same for all cathodes.

$df_{rdm}$ , the random uncertainty of  $f_{std}$ , was calculated as maximum of the inner (statistical) and outer uncertainty of the weighted mean (see equations B.7 and B.6) and thus, contains already information about the reproducibility of the single runs and cathodes.

$df_{syst}$ , the systematic uncertainty of  $f_{std}$ , corresponds to the uncertainty of the nominal value of the reference material.

### 8.3.4 Determination of the final $^{55}\text{Fe}/\text{Fe}$ -ratios of the samples

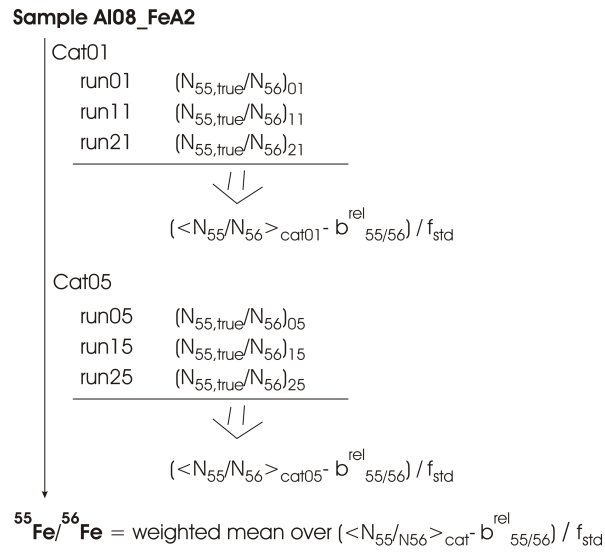


**Figure 8.2:** Schematical view of an exemplary evaluation of the isotopic ratio  $^{55}\text{Fe}/\text{Fe}$  of sample AI08\_FeA2, pressed into cathode Cat01 and Cat05 and measured during several runs.

Figure 8.2 gives an example for the determination of the final  $^{55}\text{Fe}/\text{Fe}$ -ratio of a sample by means of the previously mentioned equations. To summarize, the final (scaled) isotopic ratio  $^{55}\text{Fe}/\text{Fe}$  of a sample cathode is the blank corrected ratio divided by the scaling factor  $f_{std}$ . If a sample material was measured in several cathodes, the weighted mean of the individual  $^{55}\text{Fe}/\text{Fe}$ -ratio was calculated as final result of the AMS measurement.

One important comment with regard to the uncertainty of the final  $^{55}\text{Fe}/\text{Fe}$ -ratios: When the arithmetic mean over the single runs was calculated, always the statistical uncertainty (equation B.4) was compared with the standard deviation of the mean (equation B.3). For further calculations, then, the maximum of both values was taken and thus, contains already the reproducibility of the measurement.

In the final step, when the weighted mean over the single cathodes was calculated, the maximum between the inner (equation B.7) and outer (equation B.6) uncertainty of the weighted mean was taken, and thus, includes the reproducibility for different cathodes.

## 8.4 Results and discussion

### 8.4.1 Scaling factors and blank-correction factors for the beam-times

beam-time	wheel	reference	$f_{std}$	$df_{rdm}[\%]$	$df_{syst}[\%]$	material	$b_{55/56}$
November 2008:							
1108_TOF1	#1	AI08_Fe2	0.238	1.5	2.1	Fe	$1 \cdot 10^{-15}$
						Fe-mix	$2 \cdot 10^{-14}$
1108_TOF2a	#2	AI08_Fe2	0.210	2.9	2.1	Fe	$< 2 \cdot 10^{-14}$
1108_TOF2	#2	AI08_Fe2	0.312	1.1	2.1	Fe	$< 3 \cdot 10^{-15}$
1108_Bragg	#2	AI08_Fe2	0.585	1.0	2.1	Fe	
1108_ION	#2	AI08_Fe2	0.786	0.51	2.1	Fe	$< 7 \cdot 10^{-16}$
						Fe <sub>2</sub> O <sub>3</sub>	$< 2 \cdot 10^{-15}$
January 2009:							
0109_Bragg1	#1	AI08_Fe2	0.514	2.4	2.1	Fe	$3 \cdot 10^{-15}$
						Fe <sub>2</sub> O <sub>3</sub>	$< 3 \cdot 10^{-14}$
0109_Bragg2	#1	AI08_Fe2	0.440	3.0	2.1	Fe	$< 5 \cdot 10^{-15}$
						Fe <sub>2</sub> O <sub>3</sub>	$6 \cdot 10^{-15}$
0109_Bragg3	#1	AI08_Fe2	0.846	1.2	2.1	Fe	$1 \cdot 10^{-13}$
						Fe <sub>2</sub> O <sub>3</sub>	$7 \cdot 10^{-15}$
March 2009:							
0309_SB	#1	A0	0.809	0.95	1.6	Fe <sub>2</sub> O <sub>3</sub> -GF	$1 \cdot 10^{-11}$
						Fe	$2 \cdot 10^{-14}$
0309_ION1	#1	A0	0.905	0.67	1.6	Fe <sub>2</sub> O <sub>3</sub> -GF	$6 \cdot 10^{-14}$
						Fe	$< 1 \cdot 10^{-14}$
0309_ION2	#2	A0	0.836	0.68	1.6	Fe <sub>2</sub> O <sub>3</sub> -GF	$3 \cdot 10^{-13}$
						Fe	$4 \cdot 10^{-15}$

**Table 8.1:** Overview of the beam-times. In the left column, the date and the used detection setup are given for each beam-time. Column "reference" shows the sample material, which was used as reference material. The scaling factor  $f_{std}$  was measured relative to Faraday cup MFC04-3 ( $^{56}\text{Fe}^{3+}$ ) and its random and systematical uncertainties were derived in section 8.3.3.  $b_{55/56}$  defines the background value and is the scaled, mean blank value according to the beam-time and sample material.

In March 2009, the first beam-time took place, where the "accurate" AMS - standard A0 (see chapter 6) was measured relative to reference samples, which had been already used in November 2008 and January 2009 for normalization. Sample AI08\_Fe2 was measured in each beam-time and thus was chosen to serve as "secondary" reference standard for the AMS - measurements of November 2008 and January 2009. The nominal value  $\left(\frac{N_{55}}{N_{56}}\right)_{nom}$  of the A0 standard at 19.3.09 20:00, was  $(6.53 \pm 0.10) \cdot 10^{-10}$  (see section 6.3). The  $^{55}\text{Fe}/^{56}\text{Fe}$ -ratio of sample AI08\_Fe2 was measured, relative to the A0 standard, in March 2009 to  $(2.41 \pm 0.04) \cdot 10^{-11}$  (compare results in table 8.7) and this value was used as nominal value for the preceding AMS measurements.

The scaling factor  $f_{std}$  is shown in table 8.1 for the individual beam-times and it represents the transmission. Among others, a low transmission is due to losses of the rare isotope  $^{55}\text{Fe}$  in the beam section between the high energy Faraday cups and the detector position.

The blank value  $b_{55/56}$  in table 8.1 represents the scaled, mean  $^{55}\text{Fe}/^{56}\text{Fe}$ -ratio  $b_{55/56}^{rel}$  and is specific to the sample material. If 0 counts were measured, upper detection limits were calculated and are labeled by  $<$ .

### Sample Material: Fe

The lowest background level for Fe-blanks was observed at the TOF detection position and was about  $10^{-15}$ . If only the Bragg detector of the TOF section is used, the transmission rises at least by a factor of two. The background level rised surprisingly during the third measurement in January 0109\_Bragg3 and was probably due to the unstabilities of the tandem accelerator, because at that time, the tandem accelerator could only be operated with one chain instead of two. The detection position of the surface barrier detector shows the highest background value of about  $10^{-14}$ .

### Sample Material: $\text{Fe}_2\text{O}_3$

The background level of the  $\text{Fe}_2\text{O}_3$  blanks tend to produce a slightly larger background, but this could be just a statistical effect, because only very few cathodes (1-2) were used for blank measurements of the  $\text{Fe}_2\text{O}_3$  material, compared to 4 - 6 cathodes for blank measurements of the Fe mettalic material. This blank material was produced from Fe-powder, which was dissolved in the same way as Fe-foils, described above in chapter 8.1.

### Sample Material: $\text{Fe}_2\text{O}_3$ -GF

The background level is enhanced for the  $\text{Fe}_2\text{O}_3$ -GF blanks by a factor of 1000 at the detection position of the surface barrier detector and by a factor of up to 100 for the ionization chamber. Moreover, the isotope ratio  $^{54}\text{Fe}^{3+}/^{56}\text{Fe}^{3+}$  of the "Goodfellow  $\text{Fe}_2\text{O}_3$ -GF blanks", measured at the high energy side, seem to be systematically lower by a factor of about 3 %, compared to other samples of natural composition.

#### 8.4.2 $^{55}\text{Fe}/^{56}\text{Fe}$ versus $^{55}\text{Fe}/^{54}\text{Fe}$

These iron samples, enriched in  $^{54}\text{Fe}$ , nearly don't contain any stable  $^{56}\text{Fe}$  ( $< 1$  %) and therefore, the  $^{55}\text{Fe}/^{54}\text{Fe}$ -ratio has to be used, measured at Faraday cup MFC04-2.

The nominal value of the  $^{55}\text{Fe}/^{54}\text{Fe}$ -ratio was calculated by multiplying the known  $^{55}\text{Fe}/^{56}\text{Fe}$  ratio by a factor of  $A_{56}/A_{54}$ , where A stands for the abundances of natural iron (see isotopic composotions listed in 3.1).

The values for the scaling factors,  $f_{std,56}$  and  $f_{std,54}$ , which are obtained for the measurement of  $^{56}\text{Fe}$  in offset Faraday cup MFC04-3 and  $^{54}\text{Fe}$  in offset Faraday cup

MFC04-2 deviate up to 10 % as some fractionation effects and differences in the current measurements will occur. This is not problematic, because the isotopic ratios of the samples are measured by the same way as the reference material. The comparison of the final, scaled  $^{55}\text{Fe}/^{56}\text{Fe}$ -ratio and  $^{55}\text{Fe}/^{54}\text{Fe}$ -ratio of the samples shows an agreement to the natural abundances within 1-2 % if the sample material and reference material are the same.

The background values of  $^{55}\text{Fe}/^{54}\text{Fe}$ ,  $b_{55/54}$ , are in the range of  $10^{-14}$  for the detection positions TOF, Bragg and ION for those enriched samples.

### 8.4.3 A0, A1, A2 standards

	<b>A1</b>		<b>A2</b>		<b>A0</b>	
	$^{55}\text{Fe}/^{56}\text{Fe}$ [ $10^{-12}$ ]	$s_{random}$ [%]	$^{55}\text{Fe}/^{56}\text{Fe}$ [ $10^{-10}$ ]	$s_{random}$ [%]	$^{55}\text{Fe}/^{56}\text{Fe}$ [ $10^{-10}$ ]	$s_{random}$ [%]
calculated	4.87	1.6	1.98	1.6	6.21	1.6
1108_TOF1	–	–	–	–	–	–
1108_TOF2a	–	–	–	–	–	–
1108_TOF2	–	–	–	–	–	–
1108_Bragg	–	–	–	–	–	–
1108_ION	–	–	–	–	–	–
0109_Bragg2	–	–	–	–	–	–
0309_ION1	4.72	3.2	2.016	0.45	–	–
0309_ION2	4.63	3.5	–	–	–	–

**Table 8.2:** The calculated (results taken from table 6.5) and measured absolute isotopic ratios  $^{55}\text{Fe}/^{56}\text{Fe}$  of the samples from the dilution series. "-" means that a sample was not measured in the corresponding beamtime. The random uncertainty includes the statistical uncertainty of the sample itself and the reproducibility of the single runs and cathodes. For uncertainties due to the scaling factor  $f_{std}$ , see table 8.1. The reference date is 1.6.2009.

Table 8.2 shows the results of all determined isotopic ratios  $^{55}\text{Fe}/^{56}\text{Fe}$  for samples A1 and A2 relative to A0. The random uncertainty, which was discussed in section 8.3.3, includes only the statistical uncertainty of the sample and the reproducibility over the measured runs and cathodes. The uncertainties from the scaling factor is not included here. For comparison, the isotopic ratios  $^{55}\text{Fe}/^{56}\text{Fe}$  for samples A1, A2 and A0 were calculated to the reference date 1.6.2009 (compare table 6.5).

For the determination of the weighted mean over the single beam-times, the random uncertainty of the scaling factor  $df_{rdm,56}$  (in table 8.1) was then taken into account. That final result of the isotopic  $^{55}\text{Fe}/^{56}\text{Fe}$  - ratio is shown in table 8.3. The contribution of the systematic uncertainty of the scaling factor  $df_{syst}$  is shown separately, labeled by  $s_{syst}$ .

The samples from the dilution series show a high background (count-rate, which is unresolvable from  $^{55}\text{Fe}$  signals in the range of  $10^{-11}$ ) for the SB detection position

	$^{55}\text{Fe}/^{56}\text{Fe}$	$s_{\text{random}}$ [%]	$s_{\text{syst}}$ [%]
A1	$4.68 \cdot 10^{-12}$	2.40	1.57
A2	$2.016 \cdot 10^{-10}$	0.81	1.57

**Table 8.3:** The absolute isotopic ratios  $^{55}\text{Fe}/^{56}\text{Fe}$  of the samples from the dilution series. Data are measured ratios scaled to A0. The reference date is 1.6.2009, 12:00.

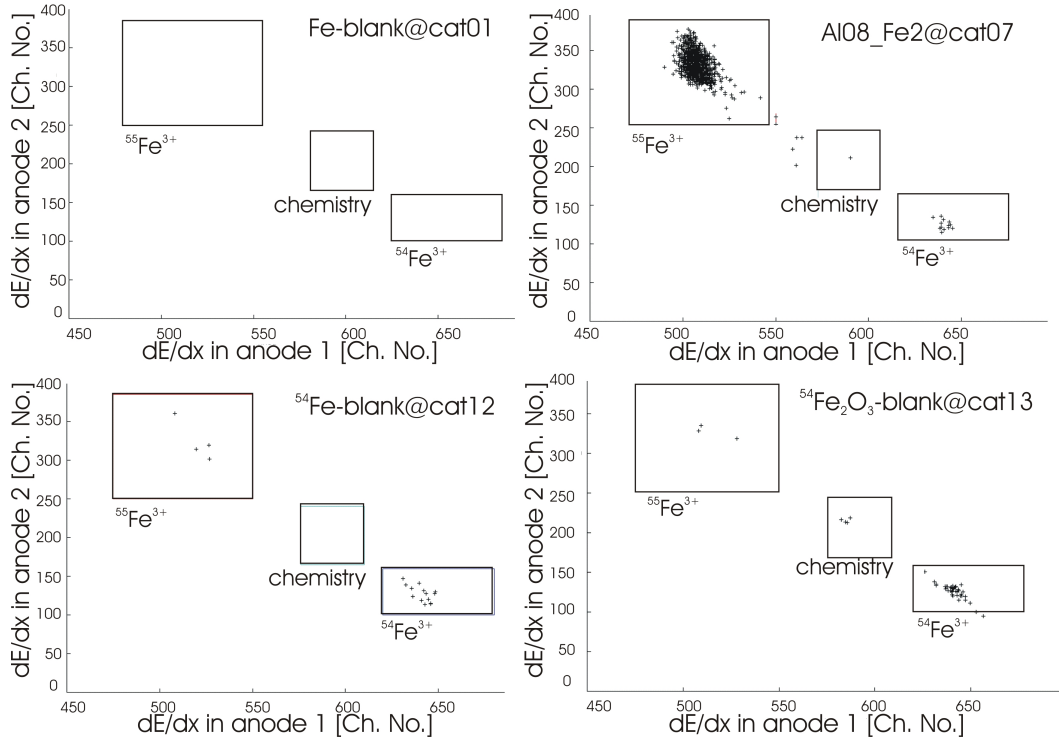


**Figure 8.3:** Comparison of spectra, which were measured by the compact type ionization chamber (March 2009) for different sample cathodes. Samples, which were treated chemically, show in between the  $^{55}\text{Fe}$ -bin and the  $^{54}\text{Fe}$ -bin some counts, labeled by "chemistry".

(was already shown by [Wallner *et al.*, 2007b]). This is a disadvantage of those diluted standards for the SB position and is probably caused by the sample material itself (dissolved Fe-foils, ordered at Goodfellow), contamination effects or chemistry preparation effects. An additional Fe-foil from Goodfellow should be dissolved in order to check, if the blank material was maybe contaminated in the course of the dilution series by the high isotopic ratios of the A0 standards. Then, an additional beam-time could demonstrate, if the new blank material also causes such a high background value and moreover, if this background is maybe smaller at the TOF detection position. For the detection positions of the TOF-detector and the ionization chamber, the diluted standards work fine.

To summarize, the dilution was a good method to produce an accurate AMS standard. For the understanding of the cause of this enhanced background rates, figures

8.3 and 8.4 show some spectra, acquired with the ionization chamber. The energy, which is deposited in the first anode is plotted on the horizontal axis and the energy, which is deposited in the second anode of the ionization chamber is plotted on the vertical axis (see also paragraph about the ionization chamber in chapter 3.3.3). Compared to  $^{55}\text{Fe}$ , isotope  $^{54}\text{Fe}$  is detected at a slightly higher channel number of Anode 1, because it has a higher energy, and thus a higher energy loss compared to  $^{55}\text{Fe}$  (according to  $ME/q^2 = \text{const}$ ). The samples from the dilution series show a significant higher background, compared to the Fe,  $^{54}\text{Fe}$ ,  $^{54}\text{Fe}_2\text{O}_3$  samples (in figure 8.3). On the left side in figure 8.3, the same sample material ( $\text{Fe}_2\text{O}_3$ -GF-blank) is shown, where cathode 10 was pressed before and cathode 02 was pressed after pressing the  $10^{-10}$  A0 standard. Cathode 02 shows a count-rate in the  $^{55}\text{Fe}$ -bin, which is higher by a factor  $\approx 10$ . A piece of one Goodfellow Fe-foil, which was not treated chemically, was also pressed into a cathode and showed a significantly lower background.

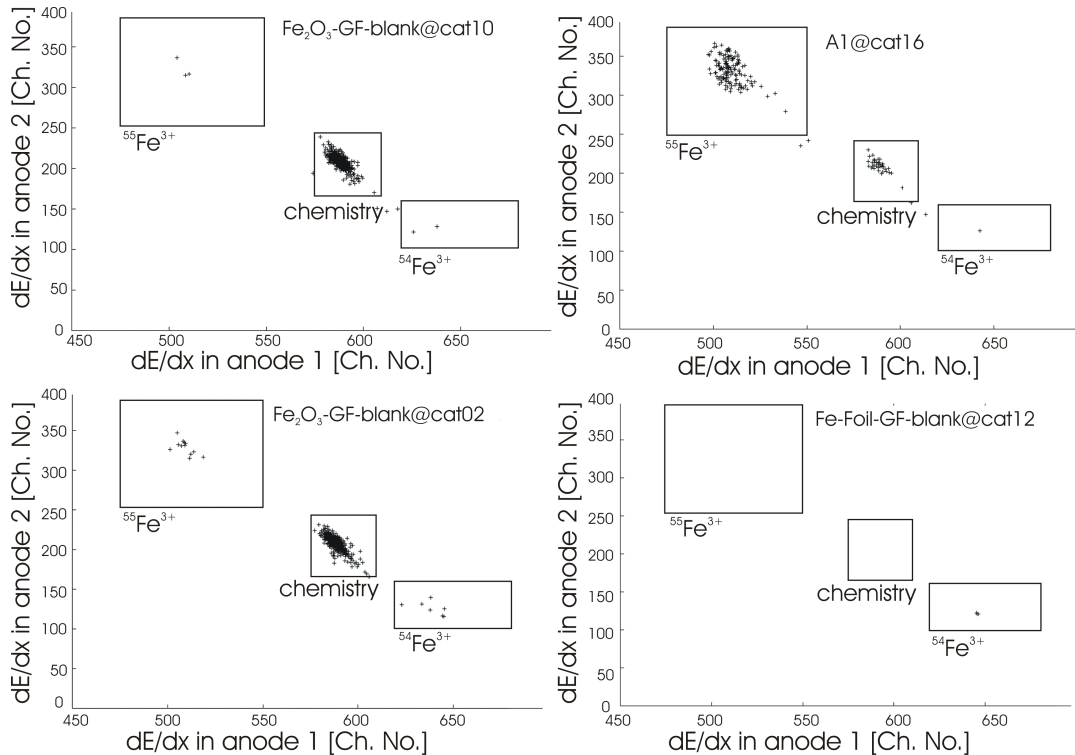


**Figure 8.4:** Comparison of spectra, which were measured by the compact type ionization chamber (March 2009) for samples, which were made in the dilution series to produce a  $^{55}\text{Fe}$ -AMS standard. Samples, which were treated chemically, show in between the  $^{55}\text{Fe}$ -bin and the  $^{54}\text{Fe}$ -bin some counts, labeled by "chemistry".

## 8.4.4 pg\_standards

	pg_A		pg_B		pg_C		pg_C-Mix	
	$^{55}\text{Fe}/^{56}\text{Fe}$	$s_{stat}$	$^{55}\text{Fe}/^{54}\text{Fe}$	$s_{stat}$	$^{55}\text{Fe}/^{54}\text{Fe}$	$s_{stat}$	$^{55}\text{Fe}/^{54}\text{Fe}$	$s_{stat}$
	[ $10^{-14}$ ]	[%]	[ $10^{-13}$ ]	[%]	[ $10^{-13}$ ]	[%]	[ $10^{-12}$ ]	[%]
calculated	1.17	5.2	8.50	5.1	11.0	5.2	1.07	5.2
1108_TOF1	0.4	200	–	–	–	–	1.48	7.7
1108_TOF2a	–	–	11	16	14	19	–	–
1108_TOF2	–	–	9.8	8.4	7.5	12	–	–
1108_Bragg	–	–	–	–	–	–	–	–
1108_ION	–	–	9.2	8.9	7.1	7.9	–	–
0109_Bragg2	–	–	–	–	–	–	–	–
0309_ION1	–	–	–	–	–	–	–	–
0309_ION2	–	–	8.55	2.8	–	–	–	–

**Table 8.4:** The calculated (results taken from table 5.9) and measured absolute isotopic ratio  $^{55}\text{Fe}/^{56}\text{Fe}$  of sample pg\_A and the absolute isotopic ratio  $^{55}\text{Fe}/^{54}\text{Fe}$  of the remaining samples from the proton irradiation. The reference date is 1.6.2009.

	55/54 (*)	$s_{stat}$ [%]	$df_{std,syst}$ [%]
pg_A	$4 \cdot 10^{-15}$	–	2.1
pg_B	$8.77 \cdot 10^{-13}$	5.0	2.1
pg_C	$7.44 \cdot 10^{-13}$	11	2.1
pg_C-Mix	$1.48 \cdot 10^{-12}$	7.8	2.1

**Table 8.5:** Isotopic ratios  $^{55}\text{Fe}/^{54}\text{Fe}$  of the pg\_samples. (\*)  $^{55}\text{Fe}/^{56}\text{Fe}$  of the pg\_A sample. The reference date is 1.6.2009.

The isotopic ratio of sample pg\_A (Fe-pellet of natural composition) lies in the range of  $10^{-14}$ . Such a low ratio leads to few counts only and therefore has very bad statistics. In this regard, the value of  $(4.1 + 8.1 - 2.9) \cdot 10^{-15}$  leads to an isotopic ratio which lies between  $1.2 \cdot 10^{-14}$  and  $1.2 \cdot 10^{-15}$ . The original aim to produce an AMS standard can not be done with iron samples of natural composition, because the isotopic ratio has to be greater for a standard to provide better statistics. But it was shown, that the AMS measurement of  $^{55}\text{Fe}$  reaches ultra-low isotopic ratios and the measured and calculated values agree within the uncertainties.

Sample pg\_B (Fe-foil, enriched in  $^{54}\text{Fe}$ , chemically treated before AMS measurements  $\rightarrow$   $^{54}\text{Fe}_2\text{O}_3$ ) was measured in the beam-times 1108\_TOF2a, 1108\_TOF2, 1108\_ION and 0309\_ION2. The uncertainty of the calculated value of  $^{55}\text{Fe}/^{54}\text{Fe}$  is about  $\pm 5.1$  % and the statistical uncertainty of the measured value is about 5%. The absolute deviation from both values is about 3.3% and is in good agreement within the given uncertainties.

Sample pg\_C (Fe-powder, enriched in  $^{54}\text{Fe} \rightarrow ^{54}\text{Fe}$ ) was measured in beam-times 1108\_TOF2a, 1108\_TOF2, 1108\_ION and 0309\_ION2 and shows a larger deviation than one would expect. One problem, which occurred when the pellet was pestled to powder as preparation before the AMS measurement, was, that the smash size of the iron corns was not equal for all corns, but sometimes were clustered to bigger ones. It was not possible to pestle them properly and because of that, some inhomogeneities of the isotopic ratios within the sample may be responsible for these results. Moreover, sample pg\_C-Mix, which is a mixture of a small amount of sample pg\_C with Fe-powder of natural composition (Fe Merck), showed an opposite deviation to the calculated isotopic ratio. Taking the mean of both samples, the calculated result show better agreement. This confirms the assumption of isotopic inhomogeneities within the sample. We expect a strongly varying isotope ratio over the sample area due to different proton intensities.

#### 8.4.5 AI06 and AI08 samples

Table 8.6 shows the measured isotopic ratios  $^{55}\text{Fe}/^{56}\text{Fe}$  of the AI06 samples. They are not used for the calculation of the neutron capture cross section, but show, how reproducible the AMS measurements are. The inner statistical uncertainty of their mean is about 1.5 - 4 % and the standard deviation of the mean is around 2 - 3 %. The single measurement has a standard deviation of about 4 - 5 %, which agrees perfectly with the statistical uncertainty of 4 - 6 % of the single measurement. Summing up, samples AI06\_Fe1 and AI06\_Fe2 show a good reproducibility.

	AI06_Fe1		AI06_Fe2		AI06_Fe3	
	$^{55}\text{Fe}/^{56}\text{Fe}$ [ $10^{-12}$ ]	$s_{\text{random}}$ [%]	$^{55}\text{Fe}/^{56}\text{Fe}$ [ $10^{-11}$ ]	$s_{\text{random}}$ [%]	$^{55}\text{Fe}/^{56}\text{Fe}$ [ $10^{-11}$ ]	$s_{\text{random}}$ [%]
1108_TOF1	1.41	4.8	1.41	3.1	–	–
1108_TOF2a	–	–	1.57	5.4	–	–
1108_TOF2	–	–	1.38	3.1	–	–
1108_Bragg	–	–	1.45	1.8	–	–
1108_ION	–	–	1.39	1.0	–	–
0109_Bragg2	–	–	–	–	–	–
0309_ION1	1.51	5.8	–	–	9.10	0.90
0309_ION2	–	–	–	–	–	–

**Table 8.6:** The absolute isotopic ratios  $^{55}\text{Fe}/^{56}\text{Fe}$  of samples, which were irradiated with neutrons at the TRIGA Mark-II reactor at the Vienna Atominstitut in 2006. The reference date is the 1.6.2009.

Table 8.7 shows the measured isotopic ratios  $^{55}\text{Fe}/^{56}\text{Fe}$  of the AI08 samples. The uncertainties of the single measurements are about 2 % for AI08\_Fe2, AI08\_FeM and about 4 % for AI08\_FeA2, AI08\_FeA4. These higher values of the statistical uncertainty is due the isotopic ratios, which are smaller for the latter one by a factor

of 10 ( $10^{-11} \rightarrow 10^{-12}$ ).

For samples AI08\_Fe2 and AI08\_FeM, the inner statistical uncertainty of the mean is less than 1% and the standard deviation is about 1 - 1.5 %. For samples AI08\_FeA2 and AI08\_FeA4, the statistical uncertainty of the mean is 3 % and their standard deviation is smaller than 1 %.

Summing up, a reproducibility at a level of 1-2% can be reached.

AI08_	FeM		Fe2		FeA2		FeA4	
	$^{55}\text{Fe}/^{56}\text{Fe}$ [ $10^{-11}$ ]	$s_{\text{random}}$ [%]	$^{55}\text{Fe}/^{56}\text{Fe}$ [ $10^{-11}$ ]	$s_{\text{random}}$ [%]	$^{55}\text{Fe}/^{56}\text{Fe}$ [ $10^{-12}$ ]	$s_{\text{random}}$ [%]	$^{55}\text{Fe}/^{56}\text{Fe}$ [ $10^{-12}$ ]	$s_{\text{random}}$ [%]
1108_TOF1	–	–	–	–	4.87	2.2	2.93	3.5
1108_TOF2a	2.30	3.1	–	–	5.08	1.4	–	–
1108_TOF2	2.20	1.3	–	–	4.79	3.5	2.79	6.7
1108_Bragg	2.26	1.7	–	–	–	–	–	–
1108_ION	2.20	0.7	–	–	4.88	3.0	–	–
0109_Bragg2	–	–	–	–	4.84	4.7	2.66	11
0309_ION1	2.26	2.1	2.45	1.4	–	–	2.80	6.7
0309_ION2	–	–	2.38	1.0	–	–	–	–

**Table 8.7:** The absolute isotopic ratios  $^{55}\text{Fe}/^{56}\text{Fe}$  of samples, which were irradiated with neutrons at the TRIGA Mark-II reactor at the Vienna Atominstitut in March 2008. The reference date is the 1.6.2009.

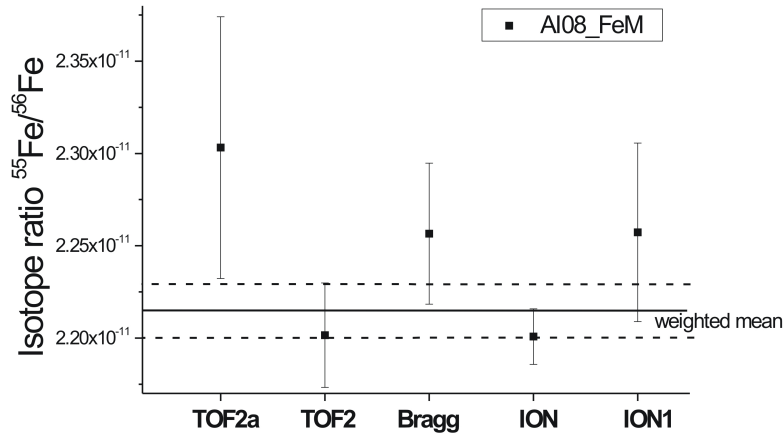


**Figure 8.5:** The  $^{55}\text{Fe}/^{56}\text{Fe}$  - ratio of sample AI08\_FeM, which was measured at different beam-times.

### 8.4.6 BP samples

Table 8.8 shows the measured isotopic ratios  $^{55}\text{Fe}/^{56}\text{Fe}$  of the BP samples. Sample BP\_FeM\_Au3 was measured three times, but the AMS measurement series in January 0109\_Bragg3 was not used for the final values of the isotopic ratio, because of unstable accelerator conditions. The uncertainties of the single measurements are between 3 and 8 % for BP\_FeM\_Au3 and about 1% for BP\_54Fe\_Au0.

For sample BP\_FeM\_Au3, the inner uncertainty of the weighted mean is about 3% and the outer uncertainty of the weighted mean is about 4.5 %, which is within the random uncertainties of the single measurements.

	BP_FeM_Au3		BP_54Fe_Au0	
	$^{55}\text{Fe}/^{56}\text{Fe}$ [ $10^{-12}$ ]	$s_{\text{random}}$ [%]	$^{55}\text{Fe}/^{54}\text{Fe}$ [ $10^{-12}$ ]	$s_{\text{random}}$ [%]
1108_TOF1	–	–	–	–
1108_TOF2a	–	–	–	–
1108_TOF2	–	–	–	–
1108_Bragg	–	–	–	–
1108_ION	–	–	–	–
0109_Bragg2	1.2	8.1	–	–
0309_ION1	–	–	–	–
0309_ION2	1.36	3.1	7.85	1.1

**Table 8.8:** The absolute isotopic ratios  $^{55}\text{Fe}/^{56}\text{Fe}$  of samples, which were irradiated with neutrons at the Budapest Research Reactor in November 2008. The reference date is the 1.6.2009.

#### Outlook

Up to now, sample BP\_FeM\_Au3 and BP\_54Fe\_Au0, which were irradiated at the Budapest Research Reactor at IKI, were measured during two beamtimes with a statistical uncertainty of about 2 % and < 1 % (for beam-time 0309\_ION2). The random uncertainty, which includes the reproducibility of the AMS-measurements (of several runs and cathodes), rised the uncertainty to about 3 % and 1 %. Additional beam-times would be useful to check the reproducibility of the measured values and to lower the statistical uncertainty of about 2 %.

## 9 Determination of the neutron capture cross section of $^{54}\text{Fe}(n,\gamma)$

Table 3.3 and figure 3.4 in chapter 3 contain information about the only two existing data for the thermal neutron capture cross section of  $^{54}\text{Fe}(n,\gamma)$  from [Brooksbank *et al.*, 1955] and [Pomerance, 1952].

One of the main goal of this thesis was the determination of the neutron capture cross section for the  $^{54}\text{Fe}(n,\gamma)$ -reaction, calculated by equation 9.1:

$$\sigma_{^{54}\text{Fe}(n,\gamma)} = \frac{N_{^{55}\text{Fe}}}{N_{^{56}\text{Fe}}} \cdot \frac{1}{\Phi} \cdot \frac{A_{^{56}\text{Fe}}}{A_{^{54}\text{Fe}}} \quad (9.1)$$

$N_{^{55}\text{Fe}}/N_{^{56}\text{Fe}}$  ...  $^{55}\text{Fe}/^{56}\text{Fe}$  ratio, measured with AMS (see chapter 8)  
 $\Phi$  ... Neutron fluence (see section 7.4)  
 $A_{^{54}\text{Fe}}, A_{^{56}\text{Fe}}$  ... Abundances of isotopes  $^{54}\text{Fe}$  and  $^{56}\text{Fe}$  (see table 3.1)

For sample BP\_54Fe\_Au0, highly enriched in  $^{54}\text{Fe}$ , the isotopic ratio  $^{55}\text{Fe}/^{54}\text{Fe}$  was measured instead of  $^{55}\text{Fe}/^{56}\text{Fe}$ . In that case, equation 9.2 was used for the determination of the cross section:

$$\sigma_{^{54}\text{Fe}(n,\gamma)} = \frac{N_{^{55}\text{Fe}}}{N_{^{54}\text{Fe}}} \cdot \frac{1}{\Phi} \quad (9.2)$$

### 9.1 Results of the cross section of $^{54}\text{Fe}(n,\gamma)$

#### 9.1.1 Samples irradiated with thermal neutrons

Table 9.1 and figure 9.1 show the results for the samples, which were irradiated with thermal neutrons at the TRIGA Mark-II reactor at the Vienna Atominstitut. Table 9.1 includes the absolute isotopic ratios  $^{55}\text{Fe}/^{56}\text{Fe}$ , which were calculated as the weighted mean over the different beam-times, the neutron fluences  $\Phi$ , and the deduced neutron capture cross sections of  $^{54}\text{Fe}(n,\gamma)$ .

For the calculation of the mean neutron capture cross section value  $\sigma_{^{54}\text{Fe}(n,\gamma)}$  and its uncertainty, first, the uncertainties of the neutron fluences and the uncertainties of the isotopic ratios were split into their statistical/random and their systematic uncertainties. Then, variance-covariance matrices were used to account for the correlated, systematical uncertainties ([Winkler, 1993] and [Winkler, 1998]). The final result for the neutron capture cross section  $\sigma_{^{54}\text{Fe}(n,\gamma)}$  is given in table 9.2. The uncertainty  $s_\sigma$  includes both, the systematical and the statistical uncertainties.

## 9 Determination of the neutron capture cross section of $^{54}\text{Fe}(n,\gamma)$

	$^{55}\text{Fe}/^{56}\text{Fe}$	$s_{\text{random}}$ [%]	$d f_{\text{syst}}$ [%]	$\Phi$ [1/cm <sup>2</sup> ]	$s_{\Phi}$ [%]	$\sigma_{^{54}\text{Fe}(n,\gamma)}$ [barn]	$s_{\sigma}$ [%]
<b>AI08_FeM</b>	$2.214 \cdot 10^{-11}$	0.67	2.1	$2.12 \cdot 10^{14}$	1.5	2.21	2.7
<b>AI08_Fe2</b>	$2.41 \cdot 10^{-11}$	1.4	1.6	$2.41 \cdot 10^{14}$	4.0	2.12	4.5
<b>AI08_FeA2</b>	$4.85 \cdot 10^{-12}$	1.7	2.1	$4.94 \cdot 10^{13}$	4.0	2.08	4.8
<b>AI08_FeA4</b>	$2.88 \cdot 10^{-12}$	2.3	2.1	$2.85 \cdot 10^{13}$	4.0	2.15	5.1

**Table 9.1:** The determined isotopic ratios  $^{55}\text{Fe}/^{56}\text{Fe}$  of samples, which were irradiated with neutrons at the TRIGA Mark-II reactor at the Vienna Atominstitut in March 2008. The reference date of the isotopic ratios is 1.6.2009. For the determination of the cross section of the corresponding neutron capture on  $^{54}\text{Fe}$ ,  $^{55}\text{Fe}/^{56}\text{Fe}$  was corrected to the end time of the irradiations.

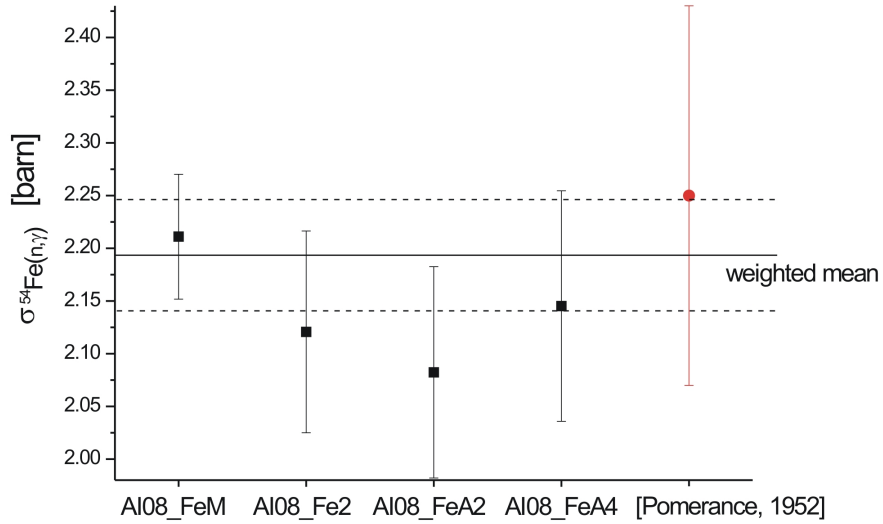


**Figure 9.1:** Results of the thermal neutron capture cross section  $\sigma_{(n,\gamma)}$  for  $^{55}\text{Fe}$ , obtained from samples which were irradiated at the TRIGA Mark-II reactor at the Vienna Atominstitut. The weighted mean is indicated by the black line and its uncertainty is indicated by the dashed lines. Correlations between the samples were taken into account. The results agree well with the cross section value from literature.

	$\sigma_{^{54}\text{Fe}(n,\gamma)}$ [barn]	$s_{\sigma}$ [barn]	$s_{\sigma}$ [%]
<b>AI08_samples</b>	2.195	0.054	2.4

**Table 9.2:** The determined neutron capture cross section  $\sigma_{^{54}\text{Fe}(n,\gamma)}$  for thermal neutron energies.

### 9.1.2 Samples irradiated with cold neutrons

Table 9.3 shows the results for the BP samples. It includes the absolute isotopic ratios  $^{55}\text{Fe}/^{56}\text{Fe}$  and  $^{55}\text{Fe}/^{54}\text{Fe}$ , the neutron fluences  $\Phi$  and the deduced neutron capture cross sections  $\sigma_{^{54}\text{Fe}(n,\gamma)}$ .

	$^{55}\text{Fe}/\text{Fe}$	$s_{\text{random}}$ [%]	$df_{\text{syst}}$ [%]	$\Phi$ [ $1/\text{cm}^2$ ]	$s_{\Phi,\text{stat}}$ [%]	$s_{\Phi,\text{syst}}$ [%]	$\sigma_{^{54}\text{Fe}(n,\gamma)}$ [barn]	$s_{\sigma}$ [%]
<b>BP_FeM_Au3</b>	$1.36 \cdot 10^{-12}$	3.19	1.57	$1.04 \cdot 10^{13}$	0.43	2.00	2.36	4.10
<b>BP_54Fe_Au0</b>	$7.85 \cdot 10^{-12}$	1.88	1.57	$3.92 \cdot 10^{12}$	1.09	2.00	2.29	2.66
				(* $3.97 \cdot 10^{12}$ )	0.01	1.18		

**Table 9.3:** The determined absolute isotopic ratio  $^{55}\text{Fe}/^{56}\text{Fe}$  of sample BP\_FeM\_Au3, and  $^{55}\text{Fe}/^{54}\text{Fe}$  of sample BP\_54Fe\_Au0 which were irradiated with cold neutrons at the Budapest Research Reactor in november 2008. The reference date of the isotopic ratios is 1.6.2009. (\*) The second value of the neutron fluence was determined independently for sample BP\_54Fe\_Au0 at the BRR. The cross section  $\sigma_{^{54}\text{Fe}(n,\gamma)}$  refers to thermal neutron energies.

For the determination of the cross section of thermal neutron capture on  $^{54}\text{Fe}$ ,  $\sigma_{^{54}\text{Fe}(n,\gamma)}$ ,  $^{55}\text{Fe}/^{56}\text{Fe}$  was corrected to the end time of the neutron irradiations. The value of the neutron fluence of sample BP\_54Fe was also determined at the BRR, and thus, could be improved to  $(3.961 \pm 0.0414) \cdot 10^{12} \text{ n/cm}^2$  ( $\pm 1\%$ ), calculated as the weighted mean. Within the uncertainties, the neutron capture cross section values fit perfectly. The final value of the neutron capture cross section was deduced from the weighted mean of the single  $\sigma_{^{54}\text{Fe}(n,\gamma)}$ -values, and also in this case, correlations between the systematical uncertainties of the  $\sigma_{^{54}\text{Fe}(n,\gamma)}$ -values were taken into account ([Winkler, 1993] and [Winkler, 1998]).

The samples were irradiated by cold neutrons, but the neutron fluence was determined using the neutron capture cross section value for thermal neutrons for  $^{197}\text{Au}$ , and thus, the  $\sigma_{^{54}\text{Fe}(n,\gamma)}$  results correspond to thermal energies as well (valid for a  $1/v$  energy dependence).

	$\sigma_{^{54}\text{Fe}(n,\gamma)}$ [barn]	$s_{\sigma}$ [barn]	$s_{\sigma}$ [%]
BP_samples	2.328	0.060	2.57

**Table 9.4:** The determined neutron capture cross section  $\sigma_{^{54}\text{Fe}(n,\gamma)}$  at thermal neutron energies.

## 9.2 Discussion

Comparing the results listed in table 9.2 and table 9.4, the cross-section value obtained with the samples irradiated at the TRIGA Mark-II reactor deviates about  $2\sigma$  from the value obtained from the samples irradiated at the Budapest Research Reactor (table 9.4). One reason for the different values could be due to the different irradiation conditions at the two reactors. The TRIGA Mark-II reactor does not offer perfect thermal conditions and a fraction of epithermal neutrons, which could be up to few percent, would lower the spectrum-averaged mean cross-section value. To quantify this epithermal fraction, an additional neutron irradiation should be performed at the TRIGA reactor:

A sandwich of cadmium-gold-cadmium will be irradiated and compared to an independently irradiated pure gold sample. Afterwards, the activity of both gold samples will be measured. The gold of the sandwich sample is activated by epithermal neutrons, because  $^{113}\text{Cd}$  absorbs the neutrons of thermal energies (its cross section is by two orders of magnitude higher with  $(2.06 \pm 0.02) \cdot 10^4$  barn [Mughabghab *et al.*, 1981]), but lets pass the neutrons of higher energies.

The irradiation conditions at the Budapest Research Reactor are well established (as discussed in chapter 7.3), the energy spectrum of the neutrons well known and thus, the final result for the neutron capture cross-section value is derived from the BP\_samples.

In table 9.5, the final results for the thermal neutron capture cross section of  $^{54}\text{Fe}$  are compared to the data from literature.  $\sigma_{^{54}\text{Fe}(n,\gamma)}$  of this work is about 3 % higher, compared to the value of [Pomerance, 1952] and agrees perfectly within the uncertainties. The uncertainty could be reduced from 8.0 % to 2.6 %.

	$\sigma_{^{54}\text{Fe}(n,\gamma)}$ [barn]	$s_\sigma$ [barn]	$s_\sigma$ [%]
this work (from BP_samples)	2.328	0.060	2.6
Pomerance, 1952	2.25	0.18	8.0

**Table 9.5:** Comparison of the neutron capture cross section values  $\sigma_{^{54}\text{Fe}(n,\gamma)}$  for thermal neutron energies.

# 10 The half-life of $^{59}\text{Ni}$

## 10.1 Introduction

The interest in the half-life of  $^{59}\text{Ni}$  is connected to several aspects of cosmo-science:

- $^{59}\text{Ni}$  is produced by cosmic rays in meteorites and in the lunar surface, mainly by the reaction  $^{58}\text{Ni}(n,\gamma)$ . The history of such meteorites (some fell, e.g. in Antarctica) can be studied by the intercomparison of cosmogenic radioisotopes inside the samples, due to their different half-lives.  $^{59}\text{Ni}$  has a half-life, which lies between that of  $^{14}\text{C}$  with  $t_{1/2} = 5730$  y and those of longer lived nuclides like  $^{36}\text{Cl}$ ,  $^{26}\text{Al}$ ,  $^{10}\text{Be}$ ,  $^{53}\text{Mn}$  with half-lives in the range of  $10^5 - 10^6$  y [Nishiizumi *et al.*, 1981]. In addition, lunar samples provide information about the solar cosmic ray (SCR) particles, which produce  $^{59}\text{Ni}$  by the reaction  $^{56}\text{Fe}(\alpha,n)$  in the first millimeters of the lunar surface [Kutschera *et al.*, 1993]. This information is also stored in meteorites but is lost when they enter the thick atmosphere of earth. Summing up,  $^{59}\text{Ni}$  is capable to deduce the preatmospheric size of a meteorite and the depth of a specific sample, which are further coupled to the thermal neutron flux produced by galactic cosmic ray (GCR) interactions in the meteorite [Kutschera *et al.*, 1993].
- $^{59}\text{Ni}$  is produced in fusion environments as activation product, mainly by the reaction  $^{60}\text{Ni}(n,2n)$  from 14-MeV neutrons. Such long-lived radionuclides can lead to significant long-term waste. To provide safety and design analyses, parameters like production cross sections, total induced activities and their decay scheme have to be studied [Wallner *et al.*, 2007b]. Moreover, such activation calculations in fusion reactor design require a high accuracy.

The half-life of  $^{59}\text{Ni}$  was first measured by [Nishiizumi *et al.*, 1981] to  $(76\,000 \pm 5000)$  y. It was calculated by the relation between the number of produced radioisotopes  $N_x$  and the activity  $A$  ( $T_{1/2} = \ln 2 \cdot N_x/A$ ), but the method applied was independent of any neutron capture cross sections. The number of  $^{59}\text{Ni}$  atoms were measured via isotope dilution mass-spectrometry and the activities were determined with an Xe-filled X-ray counter.

In the year 1994, [Rühm *et al.*, 1994] determined the  $^{59}\text{Ni}$  half-life via neutron irradiation of a  $^{58}\text{Ni}$ - and an enriched  $^{54}\text{Fe}$ - sample, where the latter one served as fluence monitor. That half-life value of  $^{59}\text{Ni}$  was calculated relative to the half-life of  $^{55}\text{Fe}$  by  $T_{1/2,Ni} = T_{1/2,Fe} \cdot (N_{59Ni}/A_{59Ni}) / (N_{55Fe}/A_{55Fe})$ , where the number of produced

radionuclides  $N_{^{55}\text{Fe}}$  was determined by  $(N_{0,^{54}\text{Fe}} \cdot \sigma_{^{54}\text{Fe}(n,\gamma)} \cdot \Phi)$  and thus, is directly coupled to the value of the thermal neutron capture cross section  $\sigma(^{54}\text{Fe}(n, \gamma))$ . The activity of both radionuclides  $^{59}\text{Ni}$  and  $^{55}\text{Fe}$  were measured with a silicon detector.

Their result of  $(108\,000 \pm 13\,000)$  y [Rühm *et al.*, 1994] is discrepant ( $\approx 2.5\sigma$ ) to the recommended  $^{59}\text{Ni}$  half-life value of  $(76\,000 \pm 5000)$  y ([Nishiizumi *et al.*, 1981]).

The uncertainty of the value of [Rühm *et al.*, 1994] ( $\pm 12\%$ ) was dominated by the uncertainty of the neutron capture cross section values, the used efficiency calibration and fluorescence yields. In 2007, that half-life value could already be renormalized to  $(97 \pm 9)$  kyr [Wallner *et al.*, 2007b] using more accurate data, but the uncertainty of  $\pm 9.3\%$  was still dominated by the uncertainty of the neutron capture cross section of  $^{54}\text{Fe}(n,\gamma)$  ( $\pm 8\%$ ). The precise measurement of  $\sigma(^{54}\text{Fe}(n,\gamma))$  in this thesis scales the recent half-life value to  $92700 \pm 5000$  years. The total uncertainty was reduced to 5.4%.

## 10.2 Scaling the half-life of $^{59}\text{Ni}$

The half-life of  $^{59}\text{Ni}$  was determined by [Rühm *et al.*, 1994] using equation 10.1:

$$T_{1/2, Ni} = T_{1/2, Fe} \cdot \frac{(N_{0,58} \cdot \sigma_{58(n,\gamma)} \cdot \varphi T_{irr,58})_{Ni}}{(N_{0,54} \cdot \sigma_{54(n,\gamma)} \cdot \varphi T_{irr,54})_{Fe}} \cdot \frac{A(t_{irr_E})_{Fe}}{A(t_{irr_E})_{Ni}}, \quad (10.1)$$

$T_{1/2, Ni}, T_{1/2, Fe}$	...	Half-life of $^{59}\text{Ni}$ , $^{55}\text{Fe}$ [s]
$N_{0,58}, N_{0,54}$	...	Number of $^{58}\text{Ni}$ , $^{54}\text{Fe}$ atoms
$\sigma_{58(n,\gamma)}, \sigma_{54(n,\gamma)}$	...	Neutron capture cross section for $^{58}\text{Ni}$ , $^{54}\text{Fe}$
$\varphi$	...	Neutron flux [ $\text{cm}^{-2}\text{s}^{-1}$ ]
$T_{irr,58}, T_{irr,54}$	...	Irradiation time of $^{58}\text{Ni}$ , $^{54}\text{Fe}$

which is based on the relation between the number of produced radionuclides  $N_x$  and the activity  $A$  ( $T_{1/2} = \ln 2 \cdot N_x/A$ ). The number of produced radionuclides  $N_x$  was calculated by the first part of equation 4.5. The specific activity at the irradiation end  $A(t_{irr_E})$  was determined by equation 10.2 (compare also to equation 4.8):

$$A(t_{irr_E}) = \frac{N}{\epsilon \cdot P_K \cdot \omega_{K_\alpha}} \cdot C \cdot e^{\lambda T_W}. \quad (10.2)$$

$N$	...	Net Peak Area, detected counts
$\epsilon$	...	Detector Efficiency
$P_K$	...	Probability for K-shell electron capture
$\omega_{K_\alpha}$	...	$K_\alpha$ fluorescence yield
$C$	...	$X_{ray}$ self absorption correction
$T_W$	...	Waiting time between the end of the irradiation and the begin of the activity measurement [s]
$\lambda$	...	Decay constant ( $= \ln(2)/t_{1/2}$ ) [1/s]

Both radionuclides,  $^{59}\text{Ni}$  and  $^{55}\text{Fe}$ , decay by electron capture emitting  $K_\alpha$  and  $K_\beta$  X-rays (6.93 and 7.65 keV for  $^{59}\text{Ni}$  and 5.90 and 6.49 keV for  $^{55}\text{Fe}$ , respectively), and were detected with a silicon detector.

For the determination of the half-life of  $^{59}\text{Ni}$ , Rühm *et al.* [1994] used the following values for the parameters in equation 10.1 and 10.2:

$$\begin{aligned}
 \sigma_{^{58}\text{Ni}(n,\gamma)} &= (4.6 \pm 0.3) \text{ barn} & \pm 6.5 \% & \text{ [Mughabghab } et al., 1981] \\
 \sigma_{^{54}\text{Fe}(n,\gamma)} &= (2.25 \pm 0.18) \text{ barn} & \pm 8.0 \% & \text{ [Mughabghab } et al., 1981] \\
 \epsilon_{\text{Ni}}/\epsilon_{\text{Fe}} &= (1.129 \pm 0.047) \text{ barn} & \pm 4.2 \% & \text{ for details see [Rühm } et al., 1994] \\
 P_{K,\text{Ni}} &= 0.885 & & \text{ for details see [Rühm } et al., 1994] \\
 P_{K,\text{Fe}} &= 0.870 & & \text{ for details see [Rühm } et al., 1994] \\
 \omega_{K_\alpha,\text{Ni}} &= 0.333 \pm 0.011 & \pm 3.3 \% & \text{ for details see [Browne } et al., 1986] \\
 \omega_{K_\alpha,\text{Fe}} &= 0.276 \pm 0.009 & \pm 3.3 \% & \text{ for details see [Browne } et al., 1986] \\
 T_{1/2,\text{Fe}} &= (2.73 \pm 0.03) \text{ years} & \pm 1.1 \% & \text{ for details see [Browne } et al., 1986] \\
 \rightarrow T_{1/2,\text{Ni}} &= (108000 \pm 13000) \text{ y} & \pm 12.0\% & \text{ [Rühm } et al., 1994]
 \end{aligned}$$

Up to date 2009, the following values were improved:

$$\begin{aligned}
 \sigma_{^{58}\text{Ni}(n,\gamma)} &= (4.13 \pm 0.05) \text{ barn} & \pm 1.21 \% & \text{ [Raman } et al., 2004] \\
 \sigma_{^{54}\text{Fe}(n,\gamma)} &= (2.328 \pm 0.060) \text{ barn} & \pm 2.58 \% & \text{ [this thesis]} \\
 P_{K,\text{Fe}} &= 0.8854 \pm 0.0016 & \pm 0.18 \% & \text{ for details see [Schötzig, 2000]} \\
 \omega_{K_\alpha,\text{Ni}} &= 0.388 \pm 0.004 & \pm 1.03 \% & \text{ for details see [Bambynek, 1984],} \\
 & & & \text{ [Schönfeld & Janßen, 1996]} \\
 \omega_{K_\alpha,\text{Fe}} &= 0.321 \pm 0.005 & \pm 1.56 \% & \text{ for details see [Bambynek, 1984],} \\
 & & & \text{ [Schönfeld & Janßen, 1996]} \\
 \omega_{K_\alpha,\text{Ni}} &= 0.388 \pm 0.004 & \pm 1.03 \% & \text{ for details see [Bambynek, 1984],} \\
 & & & \text{ [Schönfeld & Janßen, 1996]} \\
 T_{1/2,\text{Fe}} &= (2.744 \pm 0.009) \text{ y} & \pm 0.40 \% & \text{ [Junde, 2008]}
 \end{aligned}$$

## 10.3 Results

The recalculation of the half-life of  $^{59}\text{Ni}$  leads to a value of

$$\rightarrow T_{1/2,\text{Ni}} = 92700 \pm 5000 \text{ years} \quad (\pm 5.4 \%).$$

## 10.4 Discussion

The half-life values of  $^{59}\text{Ni}$ ,  $(92.7 \pm 5.0) \text{ ky}$  [renormalized in this thesis] and  $(76.0 \pm 5.0) \text{ ky}$  [Nishiizumi *et al.*, 1981] are still discrepant by about  $2 \sigma$ , but the uncertainty could be reduced to 5.4 %. This uncertainty is mainly dominated by the uncertainty of the used efficiency values of [Rühm *et al.*, 1994].







# A Appendix A

## A.1 Efficiency of the HPGe-diode

Throughout this thesis,  $\pm 2\%$  were assumed for the systematic uncertainty of the efficiency  $\epsilon_\gamma$  of the high purity germanium HPGe-diode at VERA. This value was needed, on the one hand, for the determination of the  $^{55}\text{Co}$ -activity, which was produced in iron samples via proton capture on  $^{54}\text{Fe}$  to produce a  $^{55}\text{Fe}$ -AMS standard material (see chapter 5 for details). On the other hand, the efficiency value was required for the determination of the  $^{198}\text{Au}$ -, and  $^{95}\text{Zr}$ -activity in samples, which served as fluence monitors during neutron irradiations on iron samples (see chapter 7 for details).

In this chapter, the efficiency values and its uncertainties are discussed for the HPGe-diode.

The efficiency of the high-purity germanium diode at VERA (shown in figure A.1) was studied in the nineties by Wagner by a set of primary and secondary calibration standards ( $^{241}\text{Am}$ ,  $^{109}\text{Cd}$ ,  $^{57}\text{Co}$ ,  $^{139}\text{Ce}$ ,  $^{51}\text{Cr}$ ,  $^{113}\text{Sn}$ ,  $^{85}\text{Sr}$ ,  $^{137}\text{Cs}$ ,  $^{54}\text{Mn}$ ,  $^{88}\text{Y}$ ,  $^{65}\text{Zn}$  and  $^{60}\text{Co}$ ).

The big advantage of primary calibration standards is their accuracy, which reaches a level of  $\pm 0.5\text{-}2\%$  by means of absolute measuring methods (e.g.  $4\pi$   $\beta$ - $\gamma$  coincidence method). In addition, single  $\gamma$ -ray emitters are favourable against multi-energy  $\gamma$ -ray emitters, because the latter ones are leading to following complications:

- The background of lower energy  $\gamma$ -rays is increased by the compton continuum of high energy  $\gamma$ -rays
- Small peaks can overlap with the photo-peak of interest
- Multienergy  $\gamma$ -ray emitter require a coincidence-summing correction for sample-detector distances smaller than 10 cm

The stability of the well-known efficiency of the detector was checked regularly with calibration sources. The last checks were carried out in the year 2006 and 2008, using a multi-elemental calibration source, QCY from Amersham (consisting of  $^{241}\text{Am}$ ,  $^{109}\text{Cd}$ ,  $^{57}\text{Co}$ ,  $^{139}\text{Ce}$ ,  $^{203}\text{Hg}$ ,  $^{113}\text{Sn}$ ,  $^{85}\text{Sr}$ ,  $^{137}\text{Cs}$ ,  $^{88}\text{Y}$  and  $^{60}\text{Co}$ ). In this regard, several efficiency values, originating from identical radionuclides of both calibration sources, were compared and are listed in table A.1.

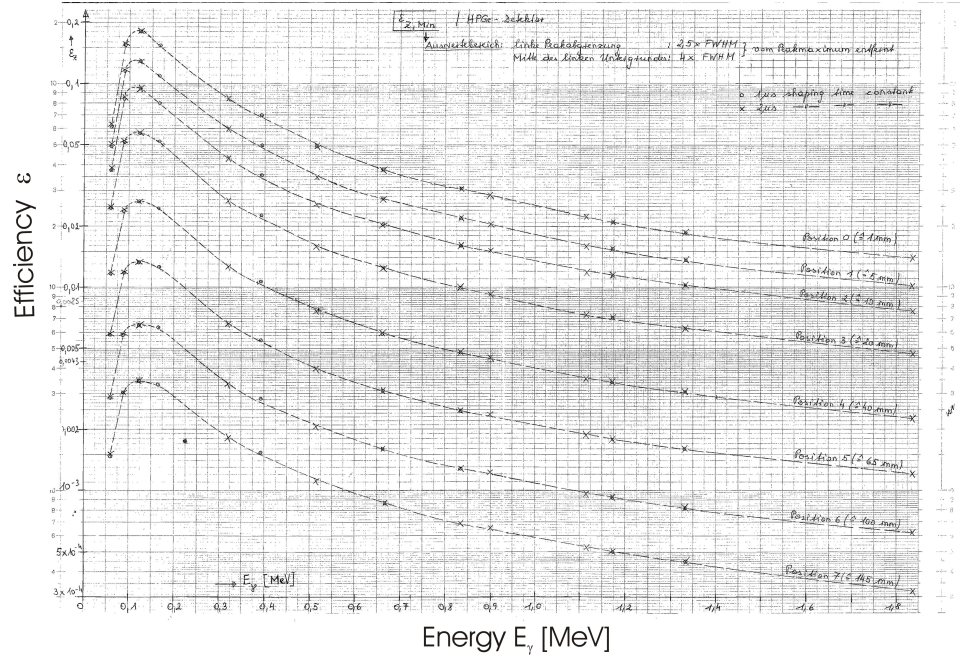


**Figure A.1:** Efficiency Curve of the HPGe-diode at VERA. The efficiency is the ratio between the measured and the emitted counts and depends on the energy of the  $\gamma$ -ray.

$E_\gamma$ [keV]	Isotope	$\epsilon_\gamma^{(1a)}$ [%]	$\pm$	$\epsilon_\gamma^{(1b)}$ [%]	$\pm$	$\epsilon_\gamma^{(2)}$ [%]	$\pm$
88.03	$^{109}\text{Cd}$	2.41	$\pm 0.05$	2.406	$\pm 0.018$	2.311	$\pm 0.072$
122.1	$^{57}\text{Co}$	2.65	$\pm 0.05$	2.644	$\pm 0.019$	2.640	$\pm 0.024$
165.9	$^{139}\text{Ce}$	2.45	$\pm 0.05$	2.449	$\pm 0.024$	2.373	$\pm 0.026$
391.7	$^{113}\text{Sn}$	1.05	$\pm 0.05$	1.061	$\pm 0.011$	1.026	$\pm 0.022$
514	$^{85}\text{Sr}$	0.78 (0.76)	$\pm 0.05$	0.7584	$\pm 0.0076$	0.7765	$\pm 0.0136$
661.6	$^{137}\text{Cs}$	0.60	$\pm 0.05$	0.5958	$\pm 0.0038$	0.6072	$\pm 0.0061$
898	$^{88}\text{Y}$	0.45	$\pm 0.05$	0.4479	$\pm 0.0094$	0.4363	$\pm 0.0045$
1173	$^{60}\text{Co}$	0.34	$\pm 0.05$	0.3413	$\pm 0.0078$	0.3421	$\pm 0.0028$
1333	$^{60}\text{Co}$	0.305	$\pm 0.05$	0.3043	$\pm 0.0073$	0.3060	$\pm 0.0025$
1836	$^{88}\text{Y}$	0.225	$\pm 0.05$	0.2274	$\pm 0.0056$	0.2197	$\pm 0.0022$

**Table A.1:** Comparison of efficiency values for several  $\gamma$ -rays, which are equal for both calibration sources. (1a) Efficiency values, read from the efficiency curve (in figure A.1). (1b) Measured efficiency-values (= data-points of the efficiency curve) by Wagner. (2) Efficiency values, obtained from the secondary standard, QCY, to check the validity of the efficiency curve.

It is known, that efficiency values of multi-energy radionuclides (e.g.  $^{88}\text{Y}$  and  $^{60}\text{Co}$  in table A.1) are smaller than efficiency values of single  $\gamma$ -ray emitters (e.g.  $^{137}\text{Cs}$ ), because several, cascading  $\gamma$ -rays coincide with each other and are, thus, detected at a higher energy. In this regard, to obtain the true efficiency value, a coincidence-summing correction was carried out for  $^{60}\text{Co}$ ,  $^{88}\text{Y}$  and  $^{55}\text{Co}$ , see section A.1.1.

### A.1.1 Coincidence summing correction

When a radionuclide emits at least two photons in sequence within the resolving time of the detector, a certain probability exists to detect those single photons as a sum pulse. Those events will be missing in the full-energy peak of the single photon and thus, give a lower count rate. The probability of summing increases with increasing total efficiency and with decreasing distance between source and detector. It does not depend on the count rate.

The geometry used for our activity measurements with a high purity germanium diode HPGe, which implies a source-detector distance of 4 cm and a total efficiency in the range of 2-4 %, thus, requires a coincidence summing correction for multi- $\gamma$ -ray emitter. In the next subsections the coincidence-summing correction factors for the measured radionuclides, which emit multi- $\gamma$ -rays, are given. Table A.2 gives a summary over the used values for the correction in the case of  $^{88}\text{Y}$  and  $^{60}\text{Co}$ , which are used in the calibration sources, and  $^{55}\text{Co}$ , which was measured in the course of the  $^{55}\text{Fe}$ -AMS standard production via proton capture.

isotope	$E_\gamma$ [keV]	$p_\gamma$ [%]	$\epsilon_{tot,\gamma}$ [%]	$\epsilon_\gamma$ [%]
$^{88}\text{Y}$	898	93.7	2.67	
$^{88}\text{Y}$	1836	99.2	2.09	
$^{60}\text{Co}$	1173.2	99.85	2.506	
$^{60}\text{Co}$	1332.5	99.983	2.349	
$^{55}\text{Co}$	477.2	20.2	3.042	0.86
$^{55}\text{Co}$	931.1	75.0	2.647	0.43
$^{55}\text{Co}$	1408	16.9		0.288
	92	1.16		2.5
	385			1.15
	411	1.07	3.12	0.98
	520	0.83	2.99	0.77
	803.7	1.87	2.75	
	1316			3.05

**Table A.2:** Values needed for the coincidence summing correction for  $^{88}\text{Y}$ ,  $^{60}\text{Co}$  and  $^{55}\text{Fe}$ . The energy of the  $\gamma$ -rays  $E_\gamma$  and their emission probabilities  $p_\gamma$  are taken from [Nudat 2.4, 2009]. The total efficiency of the germanium detector for the used geometry was retrieved from a total efficiency curve.

#### Correction factors for simple decay schemes

The photon  $E_{\gamma 1}$ , which is emitted with an emission probability  $p_1$ , is detected in the full-energy peak with a detection probability  $\epsilon_1$ . The total probability to detect the second photon (which is emitted in sequence) with the detector is  $\epsilon_{tot,2}$ . Thus, the probability to lose an event of the first full energy peak, is given by  $\epsilon_1 \cdot \epsilon_{tot,2}$ . The count rate of the first photon  $n_1$  is:

$$n_1 = Ap_1\epsilon_1 - Ap_1\epsilon_1\epsilon_{tot,2} = Ap_1\epsilon_1 \cdot (1 - \epsilon_{tot,2})$$

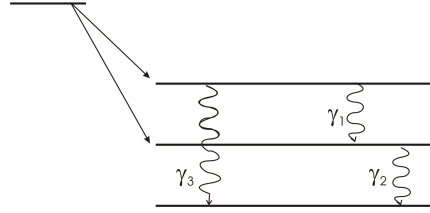


**Figure A.2:** Schematic view of a simple decay scheme. The higher energy level of the daughter nuclide can deexcite by the emission of  $\gamma_3$  or by the emission of  $\gamma_1$ , followed by  $\gamma_2$ .

and therefore has to be corrected by equation A.1:

$$C_1 = \frac{n_{\text{no coinc. sum.}}}{n_1} = \frac{1}{(1 - \epsilon_{\text{tot},1})} \quad (\text{A.1})$$

Equation A.1 was used to calculate the coincidence summing correction factor for the 898 keV -  $\gamma$ -line of  $^{88}\text{Y}$  and for the 1173.2 keV -  $\gamma$ -line of  $^{60}\text{Co}$ .

Similar considerations are done for the second photon  $E_{\gamma_2}$  of the  $\gamma$ -ray cascade. The second photon, , can only can be summed up with the first one, if it is preceded by the first one. Thus, the fraction of  $\gamma_2$  that are preceded by  $\gamma_1$  has to be added as an additional factor in this equation A.2, compared to the previous one A.1:

$$C_2 = \frac{1}{(1 - \frac{p_1}{p_2} \epsilon_{\text{tot},2})} \quad (\text{A.2})$$

Equation A.2 was applied for the 1836 keV  $\gamma$ -line of  $^{88}\text{Y}$  and for the 1332.5 keV  $\gamma$ -line of  $^{60}\text{Co}$ .

The angular correlation between both  $\gamma$ - rays was not taken into account.

### Correction factors for the complex decay schemes of $^{55}\text{Co}$

For the correction of coincidence summing one has to "study" the history before and after the  $\gamma$ - ray emission:

The two most **important summing - out effects** have been already discussed above, where the  $\gamma$ - ray of interest  $\gamma_i$  is summed up with

- (1)  $\gamma$ - rays, which are emitted in sequence afterwards (corrected by  $C_1$  from equation A.1 )
- (2)  $\gamma$ - rays, which preceded the emission of  $\gamma_i$  (corrected by  $C_2$  from equation A.2)

Two additional summing - out effects are discribed below in (3) and (4), where the  $\gamma$ - ray of interest  $\gamma_i$  is summed up with

- (3)  $X_k$ -ray, which is emitted in electron capture decays
- (4)  $X_k$ -ray, originating from internal conversion

The correction of (3) and (4) require total internal conversion coefficients, K-conversion coefficients, K-EC probability and K-shell fluorescence yields, but will

not be discussed here, because their contribution is less than 0.1 % in the case of  $^{55}\text{Co}$ .

**Summing - in - effects** occur, when the sum of two  $\gamma$ - rays is detected as sum pulse in the full energy peak in the  $\gamma$ - ray of interest and causes thus a higher count-rate.

$$n_3 = Ap_3\epsilon_3 + Ap_1\epsilon_1\epsilon_2 = Ap_1\epsilon_1 \cdot (1 - \epsilon_{tot,1})$$

$$C_3 = \frac{n_{\text{no coinc. sum.}}}{n_3} = \frac{1}{\left(1 + \frac{p_1}{p_3} \frac{\epsilon_1}{\epsilon_3} \epsilon_2\right)} \quad (\text{A.3})$$

The three most important  $\gamma$ -rays of the  $^{55}\text{Co}$ -decay are  $\gamma_{931}$ ,  $\gamma_{477}$  and  $\gamma_{1408}$  and the coincidence summing corrections are discussed below.

The 1408 keV level in the decay scheme of  $^{55}\text{Co}$  (see figure 3.5) can deexcite by three different options:

- to 44.2% an emission of  $\gamma_{1408}$
- to 52.8% an emission of  $\gamma_{477}$ , followed by  $\gamma_{931}$  (98.2%)
- to 52.8% an emission of  $\gamma_{477}$ , followed by  $\gamma_{520}$  and  $\gamma_{411}$  (2%)

For more details at the decay scheme see figure 3.5.

$$n_{477} = n_1 = Ap_1\epsilon_1 - \underbrace{Ap_1\epsilon_1 \cdot (0.98 \epsilon_{tot,931} + 0.02 \epsilon_{tot,520} + 0.02 \epsilon_{tot,411})}_{(1)} - \underbrace{Ap_1\epsilon_1 \cdot 0.528 \frac{p_{803}}{p_1} \epsilon_{tot,803}}_{(2)}$$

$$C_{477=1} = \frac{1}{1 - (0.98\epsilon_{tot,931} + 0.02 \epsilon_{tot,520} + 0.02 \epsilon_{tot,411}) - 0.528 \frac{p_{803}}{p_1} \epsilon_{tot,803}}$$

$$C_{931=2} = \frac{1}{1 - 0.98\left(\frac{p_{477}}{p_2} \epsilon_{tot,477} + \frac{p_{385}}{p_2} \epsilon_{tot,385} + \frac{p_{1213}}{p_2} \epsilon_{tot,1213} + \frac{p_{1370}}{p_2} \epsilon_{tot,1370}\right) + \frac{p_{520}\epsilon_{520}}{p_2\epsilon_2} \epsilon_{411}}$$

$$C_{1408=3} = \frac{1}{1 - 0.442 \frac{p_{803}}{p_3} \epsilon_{tot,803} + (0.98 \frac{p_{477}\epsilon_{477}}{p_3\epsilon_3} \epsilon_{931} + 0.929 \frac{p_{91}\epsilon_{91}}{p_3\epsilon_3} \epsilon_{1316})}$$

Table A.3 show the correction factors for coincidence summing of the three main  $\gamma$ - rays from the  $^{55}\text{Co}$ - decay, which were calculated for the used HPGe-geometry at VERA (source - detector distance = 40 mm).

isotope	$E_\gamma$ [keV]	$C_{coinc}$
$^{55}\text{Co}$	477.2	1.0293
$^{55}\text{Co}$	931.1	1.0095
$^{55}\text{Co}$	1408	0.9703

**Table A.3:** Coincidence correction factors for the 477, 931 and 1408 keV  $\gamma$ -ray.

### A.1.2 Results and Discussion

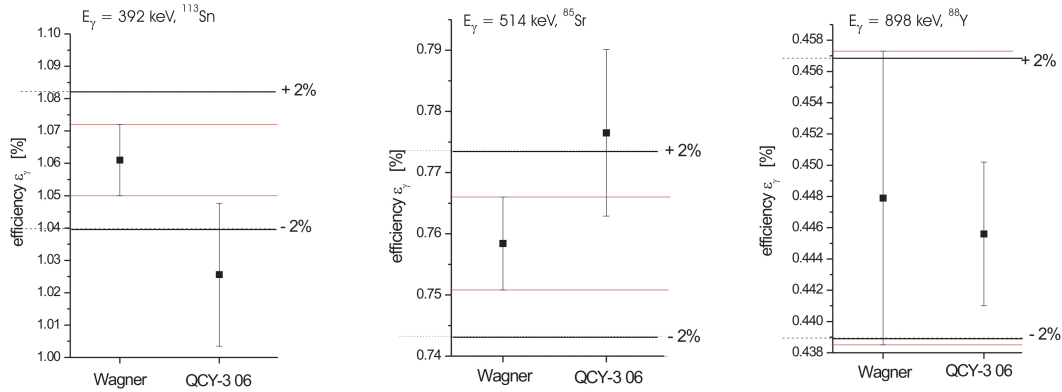
The Coincidence - summing effect influences multi- $\gamma$ -ray emitters like  $^{88}\text{Y}$ ,  $^{60}\text{Co}$  in the secondary calibration source, QCY, and  $^{55}\text{Co}$  in samples pg\_A, pg\_B and pg\_C (see table 5.1). Table A.4 shows the comparison between efficiency values, taken from (1a) the efficiency curve shown in figure A.1 and the recently measured, coincidence summing corrected efficiency values by means of a multi-elemental standard called QCY.

$E_\gamma$ [keV]	Isotope	$\epsilon_\gamma^{(1a)}$ [%]	$\pm$	$\epsilon_\gamma^{(1b)}$ [%]	$\pm$	$\epsilon_\gamma^{(2)}$ [%]	$\pm$
88.03	$^{109}\text{Cd}$	2.41	$\pm 0.05$	2.406	$\pm 0.018$	2.311	$\pm 0.072$
122.1	$^{57}\text{Co}$	2.65	$\pm 0.05$	2.644	$\pm 0.019$	2.640	$\pm 0.024$
165.9	$^{139}\text{Ce}$	2.45	$\pm 0.05$	2.449	$\pm 0.024$	2.373	$\pm 0.026$
391.7	$^{113}\text{Sn}$	1.05	$\pm 0.05$	1.061	$\pm 0.011$	1.026	$\pm 0.022$
514	$^{85}\text{Sr}$	0.78 (0.076)	$\pm 0.05$	0.7584	$\pm 0.0076$	0.7765	$\pm 0.0136$
661.6	$^{137}\text{Cs}$	0.60	$\pm 0.05$	0.5958	$\pm 0.0038$	0.6072	$\pm 0.0061$
898	$^{88}\text{Y}$	0.45	$\pm 0.05$	0.4479	$\pm 0.0094$	(*)0.4456	$\pm 0.0046$
1173	$^{60}\text{Co}$	0.34	$\pm 0.05$	0.3413	$\pm 0.0078$	(*)0.3505	$\pm 0.0029$
1333	$^{60}\text{Co}$	0.305	$\pm 0.05$	0.3043	$\pm 0.0073$	(*)0.3139	$\pm 0.0026$
1836	$^{88}\text{Y}$	0.225	$\pm 0.05$	0.2274	$\pm 0.0056$	(*)0.2254	$\pm 0.0023$

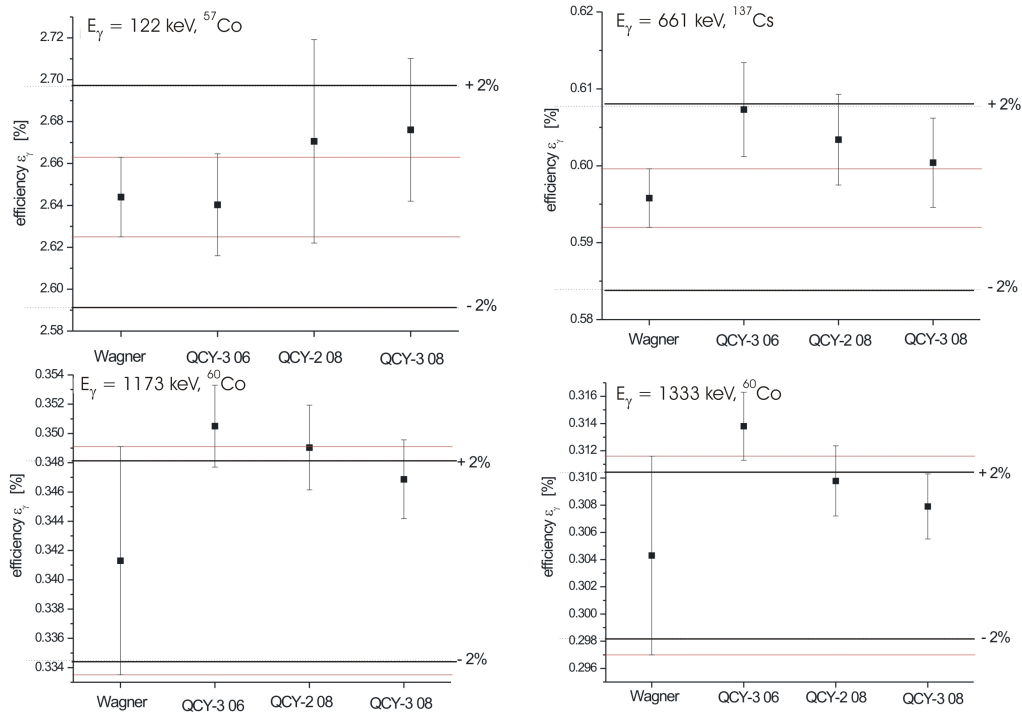
**Table A.4:** Comparison of efficiency values for several  $\gamma$ -rays, which are equal for both calibration sources, (1a) Efficiency values, read from the efficiency curve (in figure A.1). (1b) Measured efficiency-values (= data-points of the efficiency curve) by Wagner. (2) (\*) Coincidence-summing corrected) efficiency values, obtained from the secondary standard, QCY, to check the validity of the efficiency curve.

Figure A.3 and A.4 show the results from table A.4 graphically. Different calibration sources (on the horizontal axis) were used to determine the efficiency values (vertical axis) for various  $\gamma$ -rays.

## A.1 Efficiency of the HPGe-diode



**Figure A.3:** Efficiency values of three different  $\gamma$ -lines, measured by Wagner with the set of primary and secondary standards in the nineties and measured in the year 2006 with calibration source QCY-3 06. An uncertainty of 2 % covers the values very well.



**Figure A.4:** Efficiency values of four different  $\gamma$ -lines, measured by Wagner with the set of primary and secondary standards in the nineties and measured with the calibration sources QCY-3 06, QCY-2 08 and QCY-3 08. An uncertainty of 2 % covers the values very well.

It is necessary to extrapolate the efficiency-values, obtained by the secondary calibration sources QCY, for the whole energy scale to get the efficiency values e.g. for the  $\gamma$ -rays of  $^{55}\text{Co}$ . Therefore, an exponential fit over data-points was done and is shown in figure A.5. For the weight of the fit model, only the independent (not correlated) uncertainties of the efficiency values were taken:  $1\sqrt{\sigma_A^2 + \sigma_{stat}^2}$  with  $\sigma_A$  being the uncertainty of the activity and  $\sigma_{stat}$  being the statistical uncertainty of the count-rate.

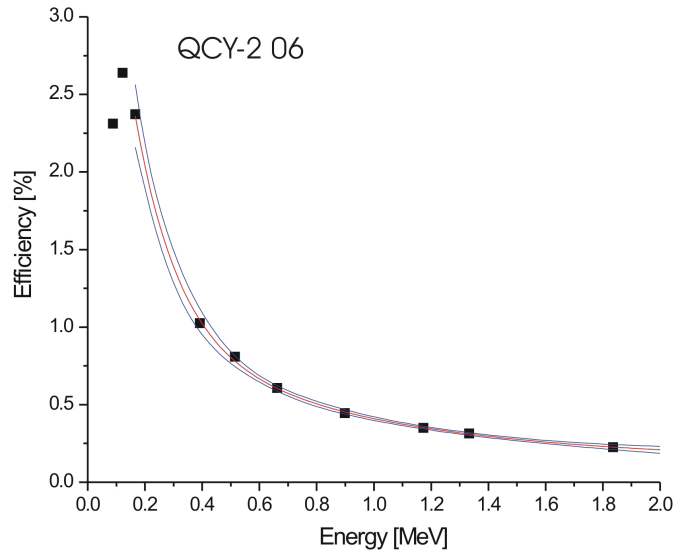


**Figure A.5:** An exponential fit of the efficiency values, measured with the secondary calibration sources QCY at the HPGe-diode at VERA. Coincidence-summing was taken into account. Only the independent uncertainties were taken as weight for the exponential fit.

The fit function was:

$$y = A_1 e^{-x/t_1} + A_2 e^{-x/t_2} + y_0, \quad (\text{A.4})$$

where the fit parameters were determined to:

$$\begin{aligned} A_1 & \dots (0.979 \pm 0.050) \\ t_1 & \dots (0.777 \pm 0.048) \\ A_2 & \dots (4.34 \pm 0.13) \\ t_2 & \dots (0.1502 \pm 0.0062) \\ y_0 & \dots (0.134 \pm 0.010) \end{aligned}$$

and the  $\chi^2/(\text{number of freedom})$  was 9.9.

Table A.5 shows the efficiency values for the main  $\gamma$ -lines of  $^{55}\text{Co}$ , which were obtained (1) with the efficiency curve shown in figure A.1 and (2) from the exponential fit shown in figure A.5. The values agree within 1-2% and thus, the efficiency values from the efficiency curve and that the efficiency has not changed significantly over a period of 15 years (see figure A.1) were proved.

$E_\gamma$ [keV]	Isotope	$\epsilon_\gamma^{(1)}$ [%]	$\pm$	$\epsilon_\gamma^{(2)}$ [%]
477	$^{55}\text{Co}$	0.85	$\pm 0.05$	0.864
931	$^{55}\text{Co}$	0.43	$\pm 0.05$	0.429
1408	$^{55}\text{Co}$	0.288	$\pm 0.05$	0.297

**Table A.5:** Efficiency values for the three, main  $\gamma$ -peaks of  $^{55}\text{Co}$ , obtained (1) with the efficiency curve shown in figure A.1 and (2) from the exponential fit shown in figure A.5.

### A.1.3 Conclusions

The conclusion of this efficiency check is, that the efficiency values obtained from the single  $\gamma$ -ray emitters of the QCY agree with the efficiency values obtained from the well-known efficiency curve from Wagner.

The coincidence summing corrections of the multi  $\gamma$ -ray emitters lie in the range of 2-3 %. In the case of  $^{88}\text{Y}$ , the efficiency values agree better to each other after the coincidence summing correction, in the case of  $^{60}\text{Co}$ , the altered efficiency values cause a deviation of up to  $\pm 3\%$ . This can be due to the uncertainty of the correction, which is based on the total efficiency curve and can be up to  $\pm 3\%$ . So far, this uncertainty of the total efficiency was not included to the calculations.

The exponential fit of the QCY-efficiency values is quite sensible to the conditions, one sets. The uncertainties e.g., which are used for the weight, should be independent, otherwise the fit parameters alter. The uncertainties of the parameters itselfs are overestimated, which is easily proved by the chi-square values of the fit ( $\approx 10$ ). During the peak analysis of the spectra, variations in the region of interests can cause an additional uncertainty of up to 1%, if it is performed differently for the calibration sources and the sample sources on the other hand.

$E_\gamma$ [keV]	Isotope	$\epsilon_\gamma^{(1)}$ [%]	$\pm$
477	$^{55}\text{Co}$	0.850	$\pm 0.017$
931	$^{55}\text{Co}$	0.4300	$\pm 0.0086$
1408	$^{55}\text{Co}$	0.2880	$\pm 0.0058$

**Table A.6:** Efficiency values for the  $\gamma$ -peaks of  $^{55}\text{Co}$ , which were used for calculations.

Concluding, it is the best to use the already existing efficiency curve, because the compared efficiency values lie within an uncertainty of 2-2.5 % (see figure A.3 and

A.4) and because that efficiency curve was well studied, including all possible corrections. Thus, the used efficiency values are taken from that efficiency curve and are listed in table A.6. The uncertainty of the efficiency is one of the dominating uncertainty in all our final values and was quantified to  $\pm 2\%$ .

# B Appendix B

## B.1 Statistics

### B.1.1 The arithmetic mean

The arithmetic mean  $\bar{x}$  of a series of measurements is the sum of the singular events  $x_i$  divided by the number of singular events  $n$ :

$$\bar{x} = \frac{1}{n} \sum x_i \quad (\text{B.1})$$

#### Uncertainties of the arithmetic mean

The fluctuation of the singular events  $x_i$  from the arithmetic mean  $\bar{x}$  is given by the standard deviation  $\sigma_{x_i}$ :

$$\sigma_{x_i} = \sqrt{\frac{(x_i - \bar{x})^2}{n - 1}}, \quad (\text{B.2})$$

where 68% of the singular events lie within the region of  $x_i \pm \sigma_{x_i}$ . Hence, the standard deviation represents the outer uncertainty of the values of the measurement series. However, in a statistical process like the decay, where the events are registered already statistically, the number of measured singular events won't influence the precision of the arithmetic mean. The statistical distribution is quasi given by nature. In order to incorporate the precision coming from the number of singular events, one determines the uncertainty of the mean  $\sigma_{\bar{x}}$  itself, which is the standard deviation divided by the root of the number of singular events:

$$\sigma_{\bar{x}} = \frac{1}{\sqrt{n}} \sqrt{\frac{(x_i - \bar{x})^2}{n - 1}}. \quad (\text{B.3})$$

When only the statistical uncertainties of the singular events are considered, one talks about the inner uncertainty of the mean  $s_{\bar{x}}^{stat}$ :

$$s_{\bar{x}}^{stat} = \frac{1}{n} \sqrt{\sum s_{x_i}^2}. \quad (\text{B.4})$$

### B.1.2 The weighted mean

If a series of independent measurements was performed, the mean is calculated by equation B.5:

$$\bar{x}^w = \frac{\sum \frac{x_i}{s_{x_i}^2}}{\sum \frac{1}{s_{x_i}^2}}, \quad (\text{B.5})$$

where  $1/s_{x_i}^2$  is the weight of a singular event.

### B.1.3 Uncertainties of the weighted mean

The outer uncertainty of the weighted mean is given by equation B.6 and the inner uncertainty of the weighted mean is given by equation B.7.

$$s_{\bar{x}}^w = \sqrt{\frac{\sum \frac{(x_i - \bar{x})^2}{s_{x_i}^2}}{n - 1 \sum \frac{1}{s_{x_i}^2}}} \quad (\text{B.6})$$

$$s_{\bar{x}}^{w,i} = \sqrt{\frac{1}{\sum \frac{1}{s_{x_i}^2}}} \quad (\text{B.7})$$

### B.1.4 Gaussian law of error propagation

Equation B.8 gives the Gaussian law of error propagation:

$$s_y = \sqrt{\sum \left( \frac{\partial y}{\partial x_i} \right)^2 s_{x_i}^2 + 2 \sum \sum \frac{\partial y}{\partial x_i} \frac{\partial y}{\partial x_j} \text{cov}(x_i, x_j)}, \quad (\text{B.8})$$

$y = y(x_i)$  ... parameter y in dependence of  $x_i$ , i going from 1 to n.  
 $s_y$  ... uncertainty of y  
 $s_{x_i}^2$  ... variance of variable  $x_i$   
 $\text{cov}(x_i, x_j)$  ... covariance between variable  $x_i$  and  $x_j$

## Bibliography

The number(s) at the end of a citation refer to the number(s) of the page(s), where the citation was used.

- AUBLE, R.L. 1983. Nuclear Data Sheets for  $A = 198$ . *Nuclear Data Sheets*, **40**, 301–383. 70, 71, 126
- BAMBYNEK, K. 1984. K fluorescence yield. *A. Meisel Ed. Leipzig Aug. 20-23*. 103
- BOUKHAROUBA, N., BRIENT, C.E., GRIMES, S.M., MISHRA, V., & PEDRONI, R.S. 1992. Low energy optical model studies of proton scattering on  $^{54}\text{Fe}$  and  $^{56}\text{Fe}$ . *Physical Review C*, **46**, 2375–2386. 27, 125
- BRANDL, T. 1998. *Aufbau eines Flugzeitspektrometers zur Messung von  $^{129}\text{I}$  am Vienna Environmental Research Accelerator*. Thesis, Univ. Wien, Institut für Radiumforschung und Kernphysik. 38
- BROOKSBANK, W.A., LEDDICOTTE, G.W., LYON, W.S., & REYNOLDS, S.A. 1955. Slow neutron activation cross sections of several elements. *Nuclear Sci. and Engineering Congress, Cleveland*, 203. 25, 26, 97, 125
- BROWNE, E., FIRESTONE, R.B., & SHIRLEY, V.S. 1986. Table of Radioactive Isotopes. *John Wiley and Sons, New York (1986)*. 103
- BURROWS, T.W. 1993. Nuclear Data Sheets for  $A = 95$ . *Nuclear Data Sheets*, **68**, 835–746. 71, 126
- CHADWICK, M.B., OBLOWINSKY, P., HERMAN, M., *et al.* 2006. ENDF/B-VII.0: Next Generation Evaluated Nuclear Data Library for Nuclear Science and Technology. *Nuclear Data Sheets*, **107**(12), 2931–3118. 23, 26, 131
- COPLEN, *et al.* 2002. Isotope-abundance variations of selected elements 2002 (IUPAC Technical Report). *Pure Appl. Chem.*, **74**, 1987 – 2017. 21, 22, 125
- DÖBELI, M., KOTTLER, C., STOCKER, M., WEINMANN, S., SYNAL, H.A., GRAJCAR, M., & SUTER, M. 2004. Gas ionization chambers with silicon nitride windows for the detection and identification of low energy ions. *Nuclear Instruments and Methods B*, **219–220**, 415–419. 35
- DEBERTIN, K., & HELMER, R.G. 1988. *Gamma- & X-Ray Spectrometry with semiconductor detectors*. North-Holland, Amsterdam. 5, 7, 9, 11, 12, 43

- FELDMAN, GARY J., & COUSINS, ROBERT D. 1998. Unified approach to the classical statistical analysis of small signals. *Physical Review D*, **57**, 3873–3889. 86
- FORSTNER, O., MICHLMAYR, L., AUER, M., GOLSER, R., KUTSCHERA, W., PRILLER, A., STEIER, P., & WALLNER, A. 2008. Applications of a compact ionization chamber in AMS at energies below 1 MeV/amu. *Proceedings of the 9th International Conference on the Application of Accelerators in Research and Technology, Florence, Italy, September 3-7, 2007. Nuclear Instruments and Methods B*, **266**, 2213–2216. 35
- HUBBEL, J.H., & SELTZER, S. M. 1996. Tables of X-Ray mass attenuation coefficients and mass energy-absorption coefficients from 1 keV to 20 MeV for elements  $Z = 1$  to 92 and 48 additional substances of dosimetric interest. *NIST, Reference Data*, **5632**. 10, 131
- JUNDE, HUO. 2008. Data Sheets for  $A = 55$ . *Nuclear Data Sheets*, **109**, 787–942. 22, 26, 27, 47, 54, 62, 103, 131
- KORSCHINEK, G., MÜLLER, D., FAESTERMANN, T., GILLITZER, A., NOLTE, E., & PAUL, M. 1990. Trace analysis of  $^{55}\text{Fe}$  in biosphere and technology by means of AMS. *Nuclear Instruments and Methods B*, **52**, 498–501. 2, 79
- KOSSERT, K., & CARLES, A. GRAU. 2006. The LSC efficiency for low- $Z$  electron-capture nuclides. *Applied Radiation and Isotopes*, **64**, 1446–1453. 63
- KUTSCHERA, W., AHMAD, I., GLAGOLA, B.G., PARDO, R.C., & REHM, K.E. 1993. Accelerator mass spectrometry of  $^{59}\text{Ni}$  in extraterrestrial matter. *Nuclear Instruments and Methods*, **73**, 403–412. 101
- MAGILL, J., PFENNIG, G., & GALY, J. 2006. Chart of the nuclides, 7<sup>th</sup> edition 2006. 21, 131
- MARTSCHINI, MARTIN. 2008.  $^{10}\text{Be} - ^{10}\text{B}$  isobar separation with a degrader foil: Implementation and testing of an optimized ion-optical setup for AMS of  $^{10}\text{Be}$ . Thesis, Univ. Wien, Faculty of Physics, Isotope Research. 35
- MICHLMAYR, LEONARD. 2007. *Isobar separation with post-stripping for the measurement of cosmogenic  $^{10}\text{Be}$  at VERA*. Thesis, Univ. Wien, Faculty of Physics, Isotope Research. 35
- M.J. BERGER, J.H. HUBBELL, S.M. SELTZER J. CHANG J.S. COURSEY R. SUKUMAR, & ZUCKER, D.S. 1990, 1998. *XCOM: Photon Cross Sections Database NIST Standard Reference Database 8 (XGAM)*. <http://www.physics.nist.gov/PhysRefData/Xcom/Text/XCOM.html>. 11, 131
- MUCHIN, K. N. 1974, 1. Auflage. *Unterhaltsame Kernphysik*. Verlag MIR Moskau VEB Fachbuchverlag Leipzig. 5

- MUGHABGHAB, S. 2006. Atlas of neutron resonances: resonance parameters and thermal cross sections  $Z=1-100$ . *Elsevier, Amsterdam*. 71, 126
- MUGHABGHAB, S.F, DIVADEENAM, M., & HOLDEN, N.E. 1981. Neutron Cross Sections from Neutron Resonance Parameters and Thermal Cross Sections. *Academic Press*. 26, 71, 100, 103, 125, 126
- NISHIZUMI, K., GENSHO, R., & HONDA, M. 1981. Half-life of  $^{59}\text{Ni}$ . *Radiochimica Acta*, **29**, 113–116. 2, 101, 102, 103
- NUDAT 2.4. 2009. Database Manager and Web Programming: Alejandro Sonzogni, NNDC, Brookhaven National Laboratory, sonzogni@bnl.gov Data Source: National Nuclear Data Center, Brookhaven National Laboratory, based on ENSDF and the Nuclear Wallet Cards, <http://www.nndc.bnl.gov/chart/>. 25, 28, 109, 125, 128
- POMERANCE, H. 1952. Thermal neutron cross sections. *Physical Review*, **88**, 412–413. 25, 26, 97, 100, 125
- PTB. 2009. [http://www.ptb.de/en/org/6/61/611/\\_index.htm](http://www.ptb.de/en/org/6/61/611/_index.htm). 63
- Q-VALUE CALCULATOR. 2009. Web programming: B. Pritychenko and A. Sonzogni, NNDC, Brookhaven National Laboratory Data Source: Atomic Mass Data Center, <http://www.nndc.bnl.gov/qcalc/>. 25, 28, 125
- RAMAN, S., OUYANG, XIAOPING, ISLAM, M. A., STARNER, J.W., JURNEY, E.T., LYNN, J.E., & MARTÍNEZ-PINEDO, G. 2004. Thermal-neutron capture by  $^{58}\text{Ni}$ ,  $^{59}\text{Ni}$  and  $^{60}\text{Ni}$ . *Physical Review C*, **70**. 103
- RÜHM, W., SCHNECK, B., KNIE, K., KORSCHINEK, G., ZERLE, L., NOLTE, E., WESELKA, D., & VONACH, H. 1994. A new half-life determination of  $^{59}\text{Ni}$ . *Planet. Space Sci.*, **42**, 227–230. 1, 2, 101, 102, 103
- ROSMAN, & TAYLOR. 1997. Isotopic compositions of the elements (IUPAC Technical Report). 21, 22, 125
- SCHÖNFELD, E., & JANSSEN, H. 1996. Evaluation of atomic shell data. *Nuclear Instruments and Methods A*, **369**, 527–533. 103
- SCHÖTZIG, U. 2000. Half-life and X-ray emission probabilities of  $^{55}\text{Fe}$ . *Applied Radiation and Isotopes*, **53**, 469–472. 103
- SEGRÉ, EMILIO. 1977. *Nuclei and Particles, second edition*. Addison-Wesley Publishing Company, Inc. 15, 16, 17
- SHAKUN, E.A., BATIY, V.G., RAKLVNENKO, YU.N., & RASTREPIN, O.A. 1986–87. Cross sections of  $(p,\gamma)$  reactions on isotopes  $^{54}\text{Fe}$ ,  $^{112}\text{Sn}$  and  $^{114}\text{Cd}$  at proton energies up to 9 MeV. *Yadernaya Fizika, Russia*, **45**, 614. 27, 125

- STEIER, P., PUCHEGGER, S., GOLSER, R., KUTSCHERA, W., PRILLER, A., ROM, W., WALLNER, A., & WILD, E. 2000. Developments towards a fully automated AMS system. *Proceedings of the IBA-14/ECCART-6 Conference, 26-30 July 1999, Dresden, Germany. Nuclear Instruments and Methods B*, **161-163**, 250-254. 83
- STEIER, P., GOLSER, R., LIECHTENSTEIN, V., KUTSCHERA, W., PRILLER, A., VOCKENHUBER, CH., & WALLNER, A. 2005. Opportunities and limits of AMS with 3-MV tandem accelerators. *Nuclear Instruments and Methods B*, **240**, 445-451. 38
- STEIER, P., DELLINGER, F., FORSTNER, O., GOLSER, R., KNIE, K., KUTSCHERA, W., PRILLER, A., QUINTO, F., SMCIK, M., TERRASI, F., VOCKENHUBER, C., WALLNER, A., WALLNER, G., & WILD, E.M. 2009. Analysis and application of heavy isotopes in the environment. *Nuclear Instruments and Methods B*. 38
- SZENTMIKLOSI, L., & BELGYA, T. 2007. *Standard Operating Procedure of the Budapest PGAA-NIPS facility*. Tech. rept. 75, 132
- TAGESEN, S., & WINKLER, G. 1993. Troubles, traps and tricks in fitting exponential decay data. *Nuclear Data Evaluation Methodology, Proceedings of the International Symposium, 12-16 October 1992, Brookhaven National Laboratory, Upton, NY, USA, World Scientific, Singapore*, 267-272. 59
- TUNIZ, CLAUDIO, BIRD, JOHN R., FINK, DAVID, & HERZOG, GREGORY F. 1998. *Accelerator Mass Spectrometry, Ultrasensitive Analysis for Global Science*. CRC Press LLC. 30
- VALENTA, A. 2001. *Actinides in nature - Investigating the usefulness of  $^{236}\text{U}$  as a neutron flux monitor*. Thesis, Univ. Wien, Institut für Radiumforschung und Kernphysik. 38
- VOCKENHUBER, CH., AHMAD, I., GOLSER, R., KUTSCHERA, W., LIECHTENSTEIN, V., PRILLER, A., STEIER, P., & S., WINKLER. 2003. Accelerator mass spectrometry of heavy long-lived radionuclides. *International Journal of Mass Spectrometry*, **223-224**, 713-732. 38
- VOCKENHUBER, CHRISTOF. 1999. *Entwicklung eines Foliendetektors zur Teilchenidentifizierung für AMS*. Thesis, Univ. Wien, Institut für Radiumforschung und Kernphysik. 38
- WALLNER, A., BICHLER, M., DILLMANN, I., GOLSER, R., KÄPPELER, F., KUTSCHERA, W., PAUL, M., PRILLER, A., STEIER, P., & VOCKENHUBER, C. 2007a. AMS measurements of  $^{41}\text{Ca}$  and  $^{55}\text{Fe}$  at VERA - two radionuclides of astrophysical interest. *Nuclear Instruments and Methods in Physics Research*

*Section B: Beam Interactions with Materials and Atoms, Accelerator Mass Spectrometry - Proceedings of the Tenth International Conference on Accelerator Mass Spectrometry*, **259**, 677–682. 79

- WALLNER, A., KNIE, K., FAESTERMANN, T., KORSCHINEK, G., KUTSCHERA, W., ROCHOW, W., RUGEL, G., & VONACH, H. 2007b. Study of the  $^{60}\text{Ni}(n,2n)^{59}\text{Ni}$  reaction from threshold to 20 MeV and the half-life of  $^{59}\text{Ni}$ . *International Conference on Nuclear Data for Science and Technology*. 83, 91, 101, 102
- WIESER. 2006. Atomic weights of the elements 2005 (IUPAC Technical Report). *Pure Appl. Chem.*, **Vol. 78, No. 11**, pp. 2051 – 2066. 21
- WINKLER, G. 1993. Data fitting and evaluation techniques for radioactive decay data. *Nuclear Data Evaluation Methodology, Proceedings of the International Symposium, 12-16 October 1992, Brookhaven National Laboratory, Upton, NY, USA, World Scientific, Singapore*, 257–266. 73, 97, 99
- WINKLER, G. 1998. On the Role of Covariances for Uncertainty Estimates in Radioactivity Measurements. *Applied Radiation and Isotopes*, **49**, 1153–1157. 73, 97, 99

*Bibliography*

---

# List of Tables

3.1	Stable isotopes of natural iron. The data for the isotopic composition is taken from [Rosman & Taylor, 1997] and the atomic mass data is taken from [Coplen <i>et al.</i> , 2002]. . . . .	22
3.2	Neutron induced reactions on the stable isotopes of iron. The data is taken from [Q-value Calculator, 2009] and the half-lives from [Nudat 2.4, 2009]. . . . .	25
3.3	The neutron capture cross section values of $^{54}\text{Fe}$ , published by [Brooks-bank <i>et al.</i> , 1955] and [Pomerance, 1952] for thermal energies. The value of [Pomerance, 1952] was measured relative to gold, whose previous thermal neutron capture cross section $\sigma_{^{197}\text{Au}(n,\gamma)}$ of 95 barn $\pm$ 8 % (for $v_n = 2200$ m/s) changed to $(98.65 \pm 0.90)$ barn (measured by [Mughabghab <i>et al.</i> , 1981]). The corrected value of the neutron cross-section is 2.25 barn. . . . .	26
3.4	Cross section values for $^{54}\text{Fe}(p,\gamma)$ , measured by [Shakun <i>et al.</i> , 1986–87] and [Boukharouba <i>et al.</i> , 1992] for MeV-protons. . . . .	27
3.5	Proton induced reactions on the stable isotopes of iron. The data is taken from [Q-value Calculator, 2009] and the half-lives from [Nudat 2.4, 2009]. . . . .	28
4.1	Coincidence correction factors for the 477, 931 and 1408 keV $\gamma$ -rays of the $^{55}\text{Co}$ decay. . . . .	44
4.2	Mass attenuation correction factors for a 477, 931 and 1408 keV $\gamma$ -ray through 200 $\mu\text{m}$ thick iron foil. . . . .	44
5.1	Specification of the sample material, used for the (p, $\gamma$ ) irradiations. . .	49
5.2	$^{54}\text{Fe}(p,\gamma)$ Irradiations at VERA. The uncertainty of the mass is given in brackets and corresponds to the last given number. . . . .	52
5.3	The amount of produced $^{55}\text{Fe}$ -atoms in sample pg_A after proton irradiation: Comparison of the two main $\gamma$ -rays at 931 keV and 477 keV. . . . .	55
5.4	The amount of produced $^{55}\text{Fe}$ -atoms in sample pg_B after proton irradiation: Comparison of the three main $\gamma$ -rays at 931 keV, 477 keV and 1408 keV, measured with the HPGe-diode at VERA. . . . .	55
5.5	The amount of produced $^{55}\text{Fe}$ -atoms in sample pg_C after the first proton irradiation: Comparison of the three main $\gamma$ -rays at 931 keV, 477 keV and 1408 keV, measured with the HPGe-diode at VERA. . . . .	56

5.6	The amount of produced $^{55}\text{Fe}$ -atoms in sample pg_C after the first proton irradiation: Comparison of the three main $\gamma$ -rays at 931 keV, 477 keV and 1408 keV, measured with the HPGe-diode at ATI (Vienna Atominstitut). . . . .	56
5.7	The amount of produced $^{55}\text{Fe}$ -atoms in sample pg_C after the second proton irradiation: Comparison of the three main $\gamma$ -rays at 931 keV, 477 keV and 1408 keV, measured with the HPGe-diode at VERA. . . . .	57
5.8	The amount of produced $^{55}\text{Fe}$ -atoms in sample pg_C after both proton irradiations: Comparison of the three main $\gamma$ -rays at 931 keV, 477 keV and 1408 keV, measured with the HPGe-diode at VERA. . . . .	57
5.9	Isotope ratios of three Fe samples, which were bombarded with protons to produce $^{55}\text{Fe}$ via $^{54}\text{Fe}(p,\gamma)^{55}\text{Co}$ . . . . .	59
5.10	Half-life of $^{55}\text{Co}$ . (1) The left values are calculated from the exponential fit. (2) The values on the right side are obtained from the linear fit. Three different time sections were used to study the influence of the number of used data points. . . . .	61
5.11	The half-life of $^{55}\text{Co}$ . . . . .	62
6.1	Masses of the Goodfellow Cambridge Ltd Fe-Foils. The uncertainty is $\pm 0.00050$ g. . . . .	64
6.2	Mass of the Master-solution $M$ , filled into bottle 1 (M1), bottle 2 (M2) and the residue (Mr), which was estimated to $(1 \pm 0.5)$ ml out of 150 ml. The mass of the residue is determined by $m_{Mr} = \frac{1}{150}(m_{M1} + m_{M2} + m_{Mr}) = \frac{1}{149}(m_{M1} + m_{M2})$ . . . . .	65
6.3	Mass of M1 solution, filled into bottle M (M1M), bottle A (M1A), and the remaining rest M1R of solution M1. As a check, the sum of the masses of the single solutions M1M, M1A and M1R were compared with the measured mass of solution M1 before. The difference is less than 1%. . . . .	65
6.4	Mass of solution, and the mass of the Fe-content inside the diluted solutions M1R, M1A, M1M, M2 and Mr. . . . .	66
6.5	Isotopic ratio of the produced $^{55}\text{Fe}$ -standards A0, A1 and A2. The reference date is 1 <sup>st</sup> October 2008 (00:00 CET). . . . .	66
7.1	Isotopic composition of the stable isotopes of Zr and Au, which were used as fluence monitors. . . . .	70
7.2	Parameters needed for the activity determination of the isotopes $^{198}\text{Au}$ and $^{95}\text{Zr}$ . The thermal neutron capture cross sections are taken from [Mughabghab, 2006] for $^{197}\text{Au}$ and [Mughabghab <i>et al.</i> , 1981] for $^{94}\text{Zr}$ . The half-lives are taken from [Auble, 1983] for $^{197}\text{Au}$ and [Burrows, 1993] for $^{94}\text{Zr}$ . The uncertainty of the detector efficiency $\epsilon_\gamma$ is 2%. . . . .	71

7.3	Comparison of the neutron fluence data, which were obtained from different fluence monitors (gold and zirconium foils) for each AI08 sample. Details about the irradiation data are given in table 7.7. Pos 4 and pos 5 denotes the positions of samples for the activity measurement.	72
7.4	Overview of the irradiated samples at the TRIGA Mark-II reactor of the Vienna Atominstitut. . . . .	73
7.5	Masses of the samples, which were used for the irradiations at the BRR. Au corresponds to the Au-powder mixed into the iron, whereas AuFront and AuBack correspond to the Au-foils, which were placed at the front and back side of the iron pellet. . . . .	76
7.6	Comparison of the results of the neutron fluence measurements for the irradiations at the BRR. . . . .	77
7.7	Overview of the irradiated samples at the TRIGA Mark-II reactor of the Vienna Atominstitut and at the Budapest Research Reactor (BRR). *AI06-samples were already available and were produced prior to this work. . . . .	77
8.1	Overview of the beam-times. In the left column, the date and the used detection setup are given for each beam-time. Column "reference" shows the sample material, which was used as reference material. The scaling factor $f_{std}$ was measured relativ to Faraday cup MFC04-3 ( $^{56}\text{Fe}^{3+}$ ) and its random and systematical uncertainties were derived in section 8.3.3. $b_{55/56}$ defines the background value and is the scaled, mean blank value according to the beam-time and sample material. . . . .	88
8.2	The calculated (results taken from table 6.5) and measured absolute isotopic ratios $^{55}\text{Fe}/^{56}\text{Fe}$ of the samples from the dilution series. "-" means that a sample was not measured in the corresponding beam-time. The random uncertainty includes the statistical uncertainty of the sample itself and the reproducibility of the single runs and cathodes. For uncertainties due to the scaling factor $f_{std}$ , see table 8.1. The reference date is 1.6.2009. . . . .	90
8.3	The absolute isotopic ratios $^{55}\text{Fe}/^{56}\text{Fe}$ of the samples from the dilution series. Data are measured ratios scaled to A0. The reference date is 1.6.2009, 12:00. . . . .	91
8.4	The calculated (results taken from table 5.9) and measured absolute isotopic ratio $^{55}\text{Fe}/^{56}\text{Fe}$ of sample pg_A and the absolute isotopic ratio $^{55}\text{Fe}/^{54}\text{Fe}$ of the remaining samples from the proton irradiation. The reference date is 1.6.2009. . . . .	93
8.5	Isotopic ratios $^{55}\text{Fe}/^{54}\text{Fe}$ of the pg_ samples. (*) $^{55}\text{Fe}/^{56}\text{Fe}$ of the pg_A sample. The reference date is 1.6.2009. . . . .	93
8.6	The absolute isotopic ratios $^{55}\text{Fe}/^{56}\text{Fe}$ of samples, which were irradiated with neutrons at the TRIGA Mark-II reactor at the Vienna Atominstitut in 2006. The reference date is the 1.6.2009. . . . .	94

8.7	The absolute isotopic ratios $^{55}\text{Fe}/^{56}\text{Fe}$ of samples, which were irradiated with neutrons at the TRIGA Mark-II reactor at the Vienna Atominstitut in March 2008. The reference date is the 1.6.2009. . . . .	95
8.8	The absolute isotopic ratios $^{55}\text{Fe}/^{56}\text{Fe}$ of samples, which were irradiated with neutrons at the Budapest Research Reactor in November 2008. The reference date is the 1.6.2009. . . . .	96
9.1	The determined isotopic ratios $^{55}\text{Fe}/^{56}\text{Fe}$ of samples, which were irradiated with neutrons at the TRIGA Mark-II reactor at the Vienna Atominstitut in March 2008. The reference date of the isotopic ratios is 1.6.2009. For the determination of the cross section of the corresponding neutron capture on $^{54}\text{Fe}$ , $^{55}\text{Fe}/^{56}\text{Fe}$ was corrected to the end time of the irradiations. . . . .	98
9.2	The determined neutron capture cross section $\sigma_{^{54}\text{Fe}(n,\gamma)}$ for thermal neutron energies. . . . .	98
9.3	The determined absolute isotopic ratio $^{55}\text{Fe}/^{56}\text{Fe}$ of sample BP_FeM_Au3, and $^{55}\text{Fe}/^{54}\text{Fe}$ of sample BP_54Fe_Au0 which were irradiated with cold neutrons at the Budapest Research Reactor in november 2008. The reference date of the isotopic ratios is 1.6.2009. (*) The second value of the neutron fluence was determined independently for sample BP_54Fe_Au0 at the BRR. The cross section $\sigma_{^{54}\text{Fe}(n,\gamma)}$ refers to thermal neutron energies. . . . .	99
9.4	The determined neutron capture cross section $\sigma_{^{54}\text{Fe}(n,\gamma)}$ at thermal neutron energies. . . . .	99
9.5	Comparison of the neutron capture cross section values $\sigma_{^{54}\text{Fe}(n,\gamma)}$ for thermal neutron energies. . . . .	100
A.1	Comparison of efficiency values for several $\gamma$ -rays, which are equal for both calibration sources. (1a) Efficiency values, read from the efficiency curve (in figure A.1). (1b) Measured efficiency-values (= data-points of the efficiency curve) by Wagner. (2) Efficiency values, obtained from the secondary standard, QCY, to check the validity of the efficiency curve. . . . .	108
A.2	Values needed for the coincidence summing correction for $^{88}\text{Y}$ , $^{60}\text{Co}$ and $^{55}\text{Fe}$ . The energy of the $\gamma$ -rays $E_\gamma$ and their emission probabilities $p_\gamma$ are taken from [Nudat 2.4, 2009]. The total efficiency of the germanium detector for the used geometry was retrieved from a total efficiency curve. . . . .	109
A.3	Coincidence correction factors for the 477, 931 and 1408 keV $\gamma$ -ray. . .	112

A.4 Comparison of efficiency values for several  $\gamma$ -rays, which are equal for both calibration sources, (1a) Efficiency values, read from the efficiency curve (in figure A.1). (1b) Measured efficiency-values (= data-points of the efficiency curve) by Wagner. (2) (\* Coincidence-summing corrected) efficiency values, obtained from the secondary standard, QCY, to check the validity of the efficiency curve. . . . . 112

A.5 Efficiency values for the three, main  $\gamma$ -peaks of  $^{55}\text{Co}$ , obtained (1) with the efficiency curve shown in figure A.1 and (2) from the exponential fit shown in figure A.5. . . . . 115

A.6 Efficiency values for the  $\gamma$ -peaks of  $^{55}\text{Co}$ , which were used for calculations. . . . . 115



## List of Figures

2.1	Mass attenuation coefficient in iron dependent on the photons energy (double logarithmical scale), taken from [Hubbel & Seltzer, 1996]. Compare the total attenuation for Ge in figure 2.2 . . . . .	10
2.2	Linear attenuation coefficients in Ge (Photon Cross Sections for photoelectric effect, Compton Scattering and pair production given in $cm^2/g$ ). Data taken from [M.J. Berger & Zucker, 1990]. . . . .	11
2.3	Typical spectrum of a monoenergetic <i>gamma</i> -ray source ( $^{137}Cs$ ), acquired by a high purity germanium detector (shielded with lead). . . .	13
2.4	The behaviour of the cross section at low energy versus the velocity $v$ or energy $E$ of the incident particle. The four upper plots are excitation functions for neutral incident particles in the case of $Q = 0$ , $Q > 0$ and $Q < 0$ . The plot at the bottom shows the excitation function for a charged incident particle in the case of $Q > 0$ . . . . .	19
3.1	Extract from the chart of nuclides [Magill <i>et al.</i> , 2006] showing the isotopes of iron. The number of protons is plotted against the number of neutrons. . . . .	21
3.2	Decay scheme of $^{55}Fe$ taken from [Junde, 2008] . . . . .	22
3.3	Some excitation functions of $^{54}Fe(n,*)$ -reactions, taken from [Chadwick <i>et al.</i> , 2006]. The cross sections for the individual neutron induced reactions are plotted against the incident neutron's energy. The scales are both logarithmic. . . . .	23
3.4	The excitation function of the $^{54}Fe(n,\gamma)$ -reaction, taken from [Chadwick <i>et al.</i> , 2006]. The scales are both logarithmic. . . . .	26
3.5	Decay scheme of $^{55}Co$ taken from [Junde, 2008] . . . . .	27
3.6	Schematic view of the Vienna Environmental Research Accelerator, based on a figure from Vockenhuber and Michlmayr. . . . .	31
3.7	A typical spectrum of $^{55}Fe$ , measured by the surface barrier detector .	35
3.8	A typical spectrum of $^{55}Fe$ , measured by the ionization chamber. . . .	36
3.9	A typical spectrum of $^{55}Fe$ , measured by the TOF spectrum . . . . .	38

4.1	Scheme of the experimental time procedure. During the irradiation time $T_{irr}$ the sample is activated and the number of produced radionuclides $N_x(t)$ increases and approaches a constant value given by the balance of production and decay. In the waiting time $T_W$ the produced radionuclides decay exponentially and are then measured during the time $T_{M_{real}}$ . . . . .	41
5.1	The left picture shows a natural iron powder in a mortar. The powder is then filled into the sample press and closed with the longer stamp in the middle picture. The right picture shows a typical iron pellet of 6 mm in diameter . . . . .	49
5.2	Position of the proton irradiation of the iron sample in section 04. . .	50
5.3	Sample holders. The left ladder with five different mounting positions was used for sample pg_A. The right ladder, which consists of the front aperture and the rear sample ladder (each one connected to a wire for a current measurement) was used for samples pg_B and pg_C. . . . .	51
5.4	Side view of the sample holder, which is connected to the flange. . . . .	51
5.5	Proton current in arbitrary units versus irradiation time $t_{irr}$ . The deposited charge on (a) the sample ladder and (b) the aperture is measured as the integral of the current. (1) The left figures correspond to the first irradiation and (2) the right ones to the second irradiation of sample pg_C. During the second irradiation, the current drops from around 300 a.u. to about 150 a.u. and increases after about 20 minutes to about 280 a.u. At the same time, the current measured at the aperture increases drastically. This indicates a shift of the proton beam from the sample to the aperture. . . . .	53
5.6	Spectrum of the irradiated sample pg_A, acquired within one hour measuring time with the HPGe. . . . .	54
5.7	True count-rate $n_{true}(t_M)$ plotted against the measuring time $t_M$ . (a) On the left side is the exponential fit of $n_{true}(t_{irr})$ and (b) the right side shows the linear fit of $\ln(n_{true}(t_{irr}))$ . The half-life of $^{55}\text{Co}$ is derived from the fitting parameters $t$ and $B$ , respectively. . . . .	60
5.8	Exponential decay of the true count-rate $n_{true}(t_M)$ with time after the first and the second proton irradiation. The half-life of $^{55}\text{Co}$ is derived from the parameters of the exponential fit. . . . .	62
6.1	Schematical view of the performed dilution steps. . . . .	65
7.1	Layout of the horizontal neutron beam facilities at the BRR, taken from the webpage <a href="http://www.kfki.hu/brr/indexen.htm">http://www.kfki.hu/brr/indexen.htm</a> . . . . .	74
7.2	Fe samples were irradiated at the position "sample chamber (NIPS)" (left side), schematical view taken from [Szentmiklosi & Belgya, 2007]. . . . .	75
7.3	Scheme of the irradiation assembly. . . . .	76

8.1	Schematical view of VERA, based on a figure from Vockenhuber and Michlmayr. The Faraday cups used for the current measurement of $^{54}\text{Fe}$ , $^{56}\text{Fe}$ and detectors used for measurements of $^{54}\text{Fe}$ are drawn into the scheme. . . . .	82
8.2	Schematical view of an exemplary evaluation of the isotopic ratio $^{55}\text{Fe}/\text{Fe}$ of sample AI08_FeA2, pressed into cathode Cat01 and Cat05 and measured during several runs. . . . .	87
8.3	Comparison of spectra, which were measured by the compact type ionization chamber (March 2009) for different sample cathodes. Samples, which were treated chemically, show in between the $^{55}\text{Fe}$ -bin and the $^{54}\text{Fe}$ -bin some counts, labeled by "chemistry". . . . .	91
8.4	Comparison of spectra, which were measured by the compact type ionization chamber (March 2009) for samples, which were made in the dilution series to produce a $^{55}\text{Fe}$ -AMS standard. Samples, which were treated chemically, show in between the $^{55}\text{Fe}$ -bin and the $^{54}\text{Fe}$ -bin some counts, labeled by "chemistry". . . . .	92
8.5	The $^{55}\text{Fe}/^{56}\text{Fe}$ - ratio of sample AI08_FeM, which was measured at different beam-times. . . . .	95
9.1	Results of the thermal neutron capture cross section $\sigma_{(n,\gamma)}$ for $^{55}\text{Fe}$ , obtained from samples which were irradiated at the TRIGA Mark-II reactor at the Vienna Atominstitut. The weighted mean is indicated by the black line and its uncertainty is indicated by the dashed lines. Correlations between the samples were taken into account. The results agree well with the cross section value from literature. . . . .	98
A.1	Efficiency Curve of the HPGe-diode at VERA. The efficiency is the ratio between the measured and the emitted counts and depends on the energy of the $\gamma$ -ray. . . . .	108
A.2	Schematic view of a simple decay scheme. The higher energy level of the daughter nuclide can deexcite by the emission of $\gamma_3$ or by the emission of $\gamma_1$ , followed by $\gamma_2$ . . . . .	110
A.3	Efficiency values of three different $\gamma$ -lines, measured by Wagner with the set of primary and secondary standards in the nineties and measured in the year 2006 with clabration source QCY-3 06. An unertainty of 2 % covers the values very well. . . . .	113
A.4	Efficiency values of four different $\gamma$ -lines, measured by Wagner with the set of primary and secondary standards in the nineties and measured with the calibration sources QCY-3 06, QCY-2 08 and QCY-3 08. An uncertainty of 2 % covers the values very well. . . . .	113
A.5	An exponential fit of the efficiency values, measured with the secondary calibration sources QCY at the HPGe-diode at VERA. Coincidence-summing was taken into account. Only the independant uncertainties were taken as weight for the exponential fit. . . . .	114

*List of Figures*

---

# Acknowledgments

Finally, arrived at page number 135, I really would like to thank many people.

First of all, I thank my supervisor Toni Wallner and the students around him for the great collaboration:

Thank you Claudia Lederer for all the beam-times, we withstood together;) I won't forget our chemistry treatments and sample preparations in the middle of Friday nights. Neither the overwhelming dimension of our produced Excel-sheets! It was real fun to work with you:)

Peter Kuess, I thank you very much for your help in the challenging time before the Budapest irradiations and the funny time in Budapest during the neutron irradiations!

Toni, thank you a lot for always taking time, whenever I needed to discuss several topics about my thesis and for your calm when explaining!!

My office at VERA was the best, I shared it with Lea Reichhart and Franz Weninger- thank you for sharing the "working" hours together, especially in bad times, when frustration threatened the concentration; in interesting times, when discussions guided us from one topic to the next one; in funny times, when ;)))))) Ah and Franz, thank you for watering my sun flower, when it was still alive.

Special thanks to Wolfgang Hieß from the workshop, without whom we would not have made the sample press. It really required a precise work.

Thanks also to Gabi Obstmayer, Ewald Friedl and Johann Lukas for the help with the current measuring sample ladder.

Of course, the sample press could not have been constructed, if Herwig Peterlik didn't borrow us his sample press: thank you!

Thank you, Peter Steier, Alfred Priller and Oliver Forstner for your advice when needed!! You were always a great help!

Thank you, Gerhard Winkler! It was very interesting and important to me to discuss uncertainties, correlations, evaluations, efficiency values, once more correlations, fittings, etc. You always had answers or suggestions to the plenty of questions I had. Thanks for taking time for those discussions.

Thanks to Tamasz Belgya and Laszlo Szentmiklósi for the time in Budapest at the Budapest Research Reactor.

Thanks to Max Bichler for the neutron irradiations at the Atominstitut.

Especially, I would like to thank Robin Golser and Toni Wallner, who gave me the possibility to write my thesis at the VERA laboratory (Isotope Research) and the financial support (to attend and participate at various conferences).

In the last lines I really would like to thank ALL my friends and my whole family, who all encouraged me throughout my thesis, especially in the last year, when I was very busy with my music studies parallel to the thesis. With their help I could enjoy it:) Thank you, my little brother Sebastian, for our daily late night-dinners, interesting discussions and your massages.

I thank my parents for offering me the possibility to study what I want to study!!!

## Curriculum vitae



**Name:** Kathrin Buczak  
**Date of birth:** November 13<sup>th</sup>, 1984  
**Place of birth:** Vienna, Austria  
**Nationality:** Austria  
**e-mail:** kbuczak@yahoo.de

---

**Education:**

1991 - 2003: Preparatory Course for piano at the University of Music and Performing Arts Vienna

1991 - 1995: Elementary School Wehlistraße, 1020 Vienna

1995 - 2003: Graduation with honors from the Gymnasium GRG1 Stubenbastei 6-8, 1010 Vienna

**Academic Studies:**

Since 2003: Student of Physics at the University of Vienna

Since 2007: Student of music (piano) at the Konservatorium Wien, University

**Semester abroad:**

October 2006 - February 2007: Erasmus - Semester in physics at the UAB (Universitat Autònoma de Barcelona, Spain)

**Laboratories during studies:**

Advanced biophysical laboratory work

Laboratory Modern Microscope Methods

Laboratory Nuclear and Isotope Physics

Isotope detection and application

**Scholarship:**

Academic Excellence Scholarship "Leistungsstipendien der Universität Wien", twice

**Diploma thesis:**

since March 2008 at VERA, Isotope Research, Faculty of Physics, University of Vienna: "Preparation of a  $^{55}\text{Fe}$ -AMS standard and the precise measurement of the neutron capture cross-section of  $^{54}\text{Fe}(n,\gamma)$ "

---

**Work Experience:**

Since 2002 giving private lessons in physics, maths and languages

Summer 2002, 2003: Office work at Optimum Bau GmbH

October 2004 - June 2005: Temporary work at the Wiener Konzerthaus

July 2006: Internship at Stefan-Meyer-Institut Vienna (SMI), including two weeks at the Paul Scherrer Institut in Switzerland (PSI) (studies of pionic deuterium)

July 2007: Internship at the Scattering & Spectroscopy Group, University of Vienna

July 21 to September 10, 2009: International Summer Student Programme 2009 at DESY (Edge effects of single crystal diamond detectors)

**Languages:** German, Polish, English and Spanish (fluent)  
French (colloquial), Italian (basics) and Latin

**Computer Languages:** Basics in C++

**Skills:** driving licence type B

**Hobbies:** Music, playing the piano, reading, dancing, snowboarden, swimming, travelling